STUDY OF THE FAR FIELD OF A PULSED SPRAY FROM AN AUTOMOTIVE FUEL INJECTOR

By

Farid Roshanghalb

A DISSERTATION

Submitted to
Michigan State University
in partial fulfillment of the requirements
for the degree of

Mechanical Engineering-Doctor of Philosophy

2015

ABSTRACT

STUDY OF THE FAR FIELD OF A PULSED SPRAY FROM AN AUTOMOTIVE FUEL INJECTOR

By

Farid Roshanghalb

Pulsed liquid sprays from automotive fuel injectors are inherently complicated and the formation and development of sprays involve multiple physical processes which take place both simultaneously and sequentially. The pulsed spray characteristics far from the injector orifice are affected by complicated mechanisms of primary and secondary break-up at and close to the injector tip. This complexity usually requires researchers to make assumptions about break-up mechanisms. In addition, several droplet collision models have been proposed for sprays, but when used in conjunction with break-up mechanism models, the accuracy and limitation of collision models have been difficult to judge. This study is intended to explore, examine and compare different collision models in a pulsed fuel spray. Since trustworthy laser diffraction measurements of droplet size distribution can be performed far from the injector orifice, these data can be used as accurate initial conditions for simulating downstream spray development. Since the pulsed sprays from automotive fuel injectors are relatively dense ones, this study eliminates the complexity of simulating two-phase flow equations for break-up and instead solves the simpler fluid mechanics problem of the Lagrangian trajectory of spray droplets, together with a droplet collision model. It was found that for the single-hole sprays of this study, when the droplet size distribution is known at some plane downstream of the break-up region, the development of the spray can be modeled accurately by using a simple Lagrangian model which calculates the droplet collision impact parameter analytically at each collision.

To my parents, Farahnaz and Gholamreza, and my lovely wife, Dr. Soroor Soltani.

ACKNOWLEDGMENTS

I would like to thank all the people who contributed somehow to this work. First and foremost I thank my advisor Professor Giles Brereton who helped me throughout my research. He is not just my thesis advisor, but a good friend who have led me through my graduate study period. I would like to specially thank my beautiful wife, Dr. Soroor Soltani, who is always supportive. She helped me in coding the simulation. I would like to thank my committee members Professors Farhad Jeberi, Harold Schock and Dennis Miller for their interest in my work. I would also like to thank Mr. Ed Timm who helped me a lot in setting up the experiments.

TABLE OF CONTENTS

LIST OF TABLES

LIST OF FIGURES

Chapter 1

Introduction

This thesis begins with introducing some background information on liquid fuel sprays, on why they are important and on what is and is not known about them.

1.1 Liquid Sprays

Liquid sprays are two-phase flows in which the liquid ligaments or droplets are the discrete phase and the surrounding vapor and/or gas is the continuous phase, and are often contrasted with bubbly flow in which the discrete and continuous phases take opposite forms. Because liquid densities are generally higher than gas densities, bubble motions experience lower kinematic inertia and higher drag forces than droplet motion. The process of forming a spray is called atomization and the device used to generate a liquid spray is called a spray nozzle, fuel injector or atomizer. Sprays are usually characterized by their particle size distribution and number density, and measurements of these quantities are central to defining product performance over a range of applications, from the delivery of drugs to the human respiratory system to the application of coatings and agrochemicals. Sprays present unique challenges in terms of their measurement environment and the speed of measurement required. Sprays are mainly used in industry to distribute materials over some specified area, or to create a large liquid surface area. Some of the industries in which sprays are used widely include:

i) The food industry: sprays are used to wash agricultural fruits and vegetables, and to dry food products such as instant coffee and powder soups.

ii) Paper making: sprays are used to clean paper rolls.

iii) Fire suppression and mining: water and solutions are sprayed from hoses and sprinklers for fire control, and water sprays are used to reduce dust levels in mining operations.

iv) Agriculture: pesticides are sprayed over target surfaces to provide uniform distributions of chemicals.

v) Fuel sprays: fuel injectors for gasoline and diesel engines and atomizers for gas turbines are used to provide liquid- and vapor-phase fuel distributions for subsequent combustion.

1.2 The Importance of Spray Research

Liquid sprays are inherently complicated and the formation and development of sprays involves multiple physical processes which take place both simultaneously and sequentially. There have been a large number of studies of liquid sprays that have led to improve understanding of spray break-up, geometrical spray shape, and understanding of microscopic behavior. However, these studies have led only to partial descriptions of spray formation and development, and several other aspects of sprays remain incompletely understood, including the processes of primary and secondary break-up. Some well-understood aspects of spray modeling require significant computational resources and so both new and simpler models are desirable to provide a better predictive capability for liquid sprays.

The objectives of this dissertation are to characterize, explain, and provide predictive models for the size distribution of droplets in the far field of pulsed spray from automotive fuel injectors.

In Chapter 2, a review of literature on sprays is given. In Chapter 3, the theoretical background to sprays is introduced and the difficulties in predicting their behavior are explained. In Chapter 4, the experimental apparatus and the visualization and measurement techniques of the present study are described. Experimentally measured effects of fuel temperature and injection pressure on spray geometrical shape and droplet size distribution along the spray axis are presented in Chapter 5. In Chapter 6, the numerical simulation procedure and numerical results are introduced. The conclusion and proposed future works are summarized in Chapter 7.

Chapter 2

Background and Objectives

In this chapter, a brief survey is given of previous studies of liquid jets, sprays, instability and primary jet break-up, secondary break-up, and droplet collision and evaporation. The terminology used to describe sprays is also introduced and explained.

2.1 Liquid Jet Instability and Break-Up

Liquid jets have been studied for more than a century. Savart's experiment [5] was one of the earliest studies of liquid jets, in which the observed effects of surface tension on jet instability led him to propose capillary instability as a possible mechanism of jet break-up. Rayleigh developed a first-order perturbation calculation for the break-up of a liquid round jet that did not depend on ambient effects [6]. He showed that the unstable disturbances that caused jet break-up must be axisymmetric and that the disturbance wavelengths must be longer than the circumference of the liquid jet.

Donnelly later conducted experimental studies of liquid jet break-up and showed that Rayleigh's droplet model did not explain the observation of large main droplets interspersed with smaller satellite droplets [7]. Furthermore, the size of these droplets was found to vary with the wave number of the disturbances. Lafranc presented a third-order perturbation analysis of the capillary instability of liquid jets in which it was shown that the higher order terms accounted quite accurately for the

presence of satellite droplets [8]. Ranz proposed that the sizes of droplets in a liquid jet spray were related to the wavelength of the most unstable waves [**?**]. The fidelity of his atomization model was questioned because aerodynamically induced wave growth requires a finite time to develop, in which case an unbroken length should be observed near the nozzle exit. However these unstable waves may have been much smaller than the jet diameter and therefore difficult to observe experimentally [9].

2.2 Spray Research

Liquid sprays have been studied for many years because of their practical importance and the difficulty in predicting their behavior from first principles. While some sprays are continuous and steady, at least after some initial start-up transient, others consist of multiple short pulses may never reach a steady state. The sprays considered in this thesis are those that arise from a single-pulse injection, such as in an automobile engine. In these sprays, liquid is typically injected for several milliseconds into a surrounding gas that may move at some low relative velocity, so that the tip of the spray has to displace only a light gas.

Before describing research into spray characteristics, some terminology used to describe large-scale spray features will be introduced. The macroscopic characteristics of a diesel spray are usually described by their shape according to three main parameters: spray penetration distance; spray angle; and spray break-up length. These parameters are often used to compare the results of different spray prediction models with measured characteristics to assess the utility of such models for describing spray development. They are also used to model combustion in burners and in engine cylinders, and to predict whether or not sprayed droplets will collide with walls.

The spray tip penetration is defined as the time-dependent distance covered by the spray in the

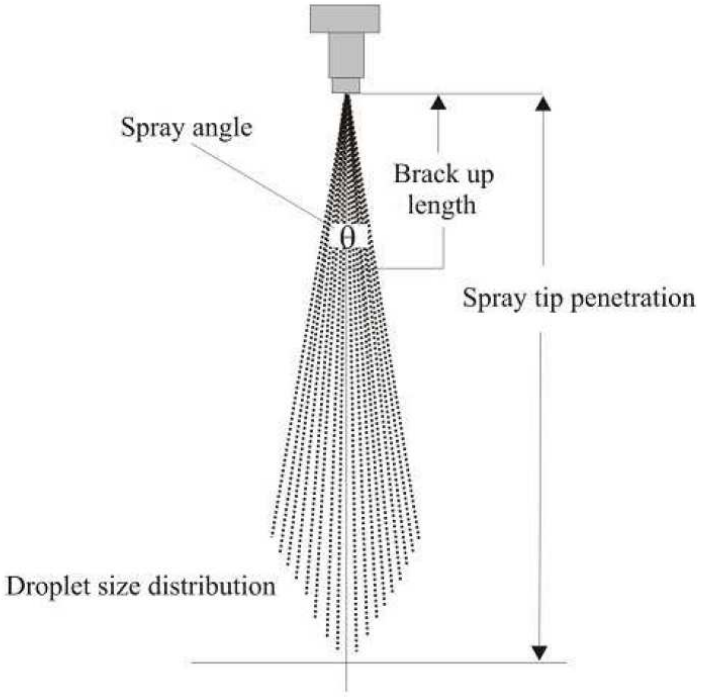

Figure 2.1 Macroscopic characteristics of a single-jet Diesel spray [1]

surrounding gas phase. The tip penetration length is determined by the effects of the momentum of the injected fluid and the resistive force exerted by the gas phase. Several models were developed to predict the propagation of the spray tip as a function of time, for different injection conditions and were compared with experimental data [10]. Spray penetration lengths and spray cone angles were measured experimentally using photographic techniques. Such techniques were used by Miller and Beardsley [11] who studied the effect of the ambient gas density on the penetration length of an engine spray.

Several attempts have been made to find correlations that can predict the fuel-spray tip penetration especially for Diesel fuel sprays. Dent (1971) proposed from experimental data a correlation applicable to pulsed Diesel sprays, described by the following equation [12]:

$$S(t) = 3.07 \left(\frac{\Delta P}{\rho g}\right)^{1/4} \left(\frac{294}{T_g}\right)^{1/4} \sqrt{d_0 t}, \tag{2.1}$$

where t is the time after the start of injection, ΔP is the pressure difference at the nozzle hole, d_0 is the nozzle hole diameter, and T_g and ρ_g are the ambient gas temperature and density, respectively. This correlation predicts that spray tip penetration increases in proportion to the square root of time and is independent of the injected fluid characteristics. According to Correas (1988), the tip penetration of a Diesel fuel spray is proportional to the square root of time and the mean velocity at the beginning of the injection. His proposed correlation is [13]:

$$S(t) = C_1 U_0^{0.5} \sqrt{d_{eq} t}, d_{eq} = d_0 \sqrt{\frac{\rho_l}{\rho_g}}, \tag{2.2}$$

where d_{eq} is an equivalent diameter, ρ_l is the liquid density and C_1 is an experimental constant. Jaward et al. proposed as an alternative correlation [14]:

$$S(t) = C_2 \Delta P^{0.25} \sqrt{t \rho_l^{0.25}} \rho_g^{-0.14}, \tag{2.3}$$

where C_2 is an experimentally determined constant. An empirical equation was proposed by Jimenez et al. which states that the tip penetration is proportional to time raised to the power of 0.9 [15]:

$$S(t) = 0.6^{-3} U_0 t^{0.9} \left(\frac{\rho_g}{\rho_l} \right)^{-0.163}, \tag{2.4}$$

where U_0 is the mean liquid velocity at the beginning of the injection.

An important parameter of fuel sprays is the angle of the edge of the spray as it emerges from the orifice of the injector. While different ways to measure the cone angle have been proposed, a common definition is that it is the angle that is formed by two straight lines in contact with the spray's outline at a distance equivalent to 60 times the diameter at exit from the injector [1]. When a specific amount of fuel is injected into a chamber using injectors of different designs, the effect

of changing the cone angle has a reciprocal effect on the penetration length of the spray. That is to say, a larger cone angle reduces the penetration length and can cause interference between sprays in a multi-orifice nozzle, which can promote merging of droplets through collision. On the other hand, a larger penetration length results when there is a smaller cone angle, which can cause the spray to collide with the combustion-chamber wall, which is undesirable.

There have been several attempts to propose formulas to determine the cone angle. One of the most widely used, which can be used for gas phases with densities lower than 15 kg/m^3, is [1]:

$$tan\left(\frac{\theta}{2}\right) = 0.13\left(1 + \frac{\rho g}{\rho_l}\right), \tag{2.5}$$

where θ is the cone angle, ρ_g and ρ_l are the gas and liquid phase density, respectively. In the above equation, the aspect ratio of the injector is not included, although Reitz and Braco considered it in their investigations [16]. According to Hiroyasu et al. the cone angle can be determined as [17]:

$$\theta = 0.05\left(\frac{d^2\rho_a(\rho_l - \rho_a)}{\mu_a^2}\right)^{1/4}, \tag{2.6}$$

where d is the orifice diameter, μ_a is the gas phase viscosity, ρ_a and ρ_l are the gas and liquid phase density, respectively.

Reitz et al. conducted experiments using nozzles with wide range of diameters, and over a wide range of liquid- and gas-phase pressures [9]. Using a high-speed camera, they were able to calculate spray angles under different operating conditions. They showed that the spray angle increased with increasing injection velocity. Williams proposed a statistical formalism for describing the behavior of sprays which included the effects of droplet growth, the formation of new droplets, collisions and aerodynamic forces [18]. This study was a significant step towards modeling the

spray's break-up statistically and accounting for collisions between droplets. Williams used the Liouville theorem to describe the single-particle probability density. Reitz et al. [19] implemented three coupled models to simulate Diesel-fuel sprays. They used flow cavitation and evaporation models for the Eulerian liquid phase along with an atomization model for high-pressure Diesel sprays. Luret et al. used a direct numerical simulation to improve the Eulerium Lagrangian Spray Atomization (ELSA) model [20], which was originally proposed by Vallet et al. [21].

Arcoumanis et al. [22] developed a cavitation-induced atomization model, which used the total area at the exit of the injection hole occupied by cavitation bubbles to calculate the radius of an equivalent bubble having the same area as the entire cavitation-bubble population. Huh and Gosman [23] published a phenomenological spray atomization model based on the assumption that cavitation and turbulence inside the nozzle hole are attributed to turbulent fluctuations in the exit flow, as the dominant source of perturbations at the free surface of the liquid jet. Baumgarten et al. developed a model for cavitation and turbulence induced primary break-up which was able to impose the influence of the cavitation nozzle flow on their spray break-up. Their model described the transition from the cavitating flow inside the injection hole to the dense spray near the nozzle [24].

Wan and Peters [25], Sazhin et al. [26] and Naber and Siebers [27] modeled spray penetration by solving the cross sectional averaged equations of the lquid-phase flow, describing the mass and momentum balance in the spray. Sjoberg [18] attempted to incorporate conditions at the tip region of the spray by assuming that droplets were collected in a region near the spray tip; the shape of the near-tip region was approximated by a ball of growing radius. Roisman et al. [28] studied a high speed fuel spray penetration at distances much longer than the break-up length in a pressure chamber. In their proposed spray propagation model, inertia of the liquid-air mixture and the formation of the vortex-ring-like structures near the leading edge of the spray were considered.

Their propagation prediction agreed well with experimental data reported by Kamimoto et al. [28].

Panchagnula and Sojka [29] carried out a theoretical study of droplet SMD (Sauter Mean Diameter) and reported that SMD increased with increasing axial distance for an effervescent atomizer spray. They attributed this SMD increase to both coalescence of large- and medium-size droplets and evaporation of small droplets. A contrasting conclusion was reached by Ghaemi et al. [30], who showed that the increase of droplets SMD with increasing downstream axial distance from an atomizer was primarily the result of evaporation of small droplets and to a much lesser extent the result of coalescence. Kastengren et al. studied the effect of ambient gas density on the structure of diesel sprays near nozzles using x-ray radiography. Their observations showed that the spray width became much larger as the ambient density increased [31]. Klein-Douwel et al. used the shadowgraph technique to determine macroscopic characterizations of a Diesel fuel injection spray. Their work revealed that not all fuel sprays behave identically, even when external conditions are kept the esame [32]; this observation suggested a stochastic nature in spray behavior. Taskiran and Ergeneman performed an experiment to find the temporal and spatial evolution of Diesel sprays. They investigated the spray penetration and cone angle and found that the cone angle was time dependent in their pulsed sprays [33].

2.3 Evaporation in Droplets and Sprays

Droplet evaporation has been modeled with varying degrees of complexity, according to the accuracy desired. Some droplet models have been developed based on the assumption that the droplet surface temperature is uniform and does not change with time. This simplification reduces the dimensionality of the problem by eliminating the need to solve an energy equation for droplet temperature [34] and can be desirable in simplified analytical studies of droplet evaporation and

thermal ignition of fuel vapor/air mixture [35–39]. One of the most commonly used assumptions in modeling droplet evaporation is that the droplet retains its spherical form, even when moving [40–42]. Generally, the fuel droplet evaporation process includes two main phases: the transport of fuel molecules from the surface of the droplet into gas through evaporation and surface recession; and diffusion of fuel vapor from the droplet surface of the droplets into the ambient gas. Empirical correlations have been proposed for the evaporation of droplets [43, 44]. Sazhin et al. proposed numerical modeling of droplet heating and evaporation by convection and radiation from the surrounding gas. Their work was based on an analytical solution of the heat conduction equation inside the droplet, with the assumption of a constant convective heat transfer coefficient [45]. Woo et al. developed an analytical mass transfer expression to describe the evaporation of pure droplets in the convective regime [46]. Brereton [47] developed a spherical model with temperature-dependent properties for evaporation of multicomponent liquid droplets by simplifying the partial differential equations of droplet heat transfer and mass diffusion by approximating them as ordinary differential equations. Torres et al. [48] used the Peng-Robinson equation of state to extend their coupled PDE model of the continuity, thermal energy and species diffusion equations to high pressures and implemented their multicomponent fuel model into KIVA-3V.

2.4 Micro-Characterizations of Sprays

Droplets produced by atomizers are not usually of uniform diameter and so can more usefully be described by a distribution. One way of describing a spray is by specifying the mean diameter of the droplets at certain locations. There are multiple definitions of mean droplet diameter and each one may be useful for interpreting particular spray phenomena. A general relationship for

calculating the mean diameter is:

$$d_{ab} = \left(\frac{\sum_{i=0}^{N} N_i d_i^a}{\sum_{i=0}^{N} N_i d_i^b} \right)^{1/a-b}, \tag{2.7}$$

where i represents the different classes of droplets which have the same diameter d_i, and N is the total number of droplets, and a and b are integers. Table 2.1 shows the different mean diameter definitions and their applications.

Table 2.1 Mean diameters and applications

a	b	Name	Symbol	Application
1	0	Arithmetic Diameter (AMD)	d_{10}	Comparison
2	0	Surface Area	d_{20}^2	Surface area controlling
3	0	Volume	d_{30}^2	Volume controlling
2	1	Surface Area Length	d_{21}	Absorption
3	1	Volume Length	d_{31}	Evaporation
3	2	Sauter Mean Diameter (SMD)	d_{32}	Vaporization
4	3	De Brouckere	d_{43}	Combustion equilibrium

The most commonly used mean diameter is the SMD, which represents the diameter of an imaginary droplet that has the same ratio of the total liquid volume in a spray to the total droplet surface area in a spray. It can be interpreted as a value that shows the atomization quality. The smaller the SMD, the finer the droplets and the better the atomization of the spray. The aerodynamic forces on a droplet and the time it takes to vaporize depend on its size, with smaller droplets having more rapid acceleration or deceleration and shorter vaporization times than larger ones. Fig. 2.2 shows a log-normal droplet distribution which is generated randomly for a total number of 1000 droplets. Mean diameters of this distribution are presented in Table 2.2.

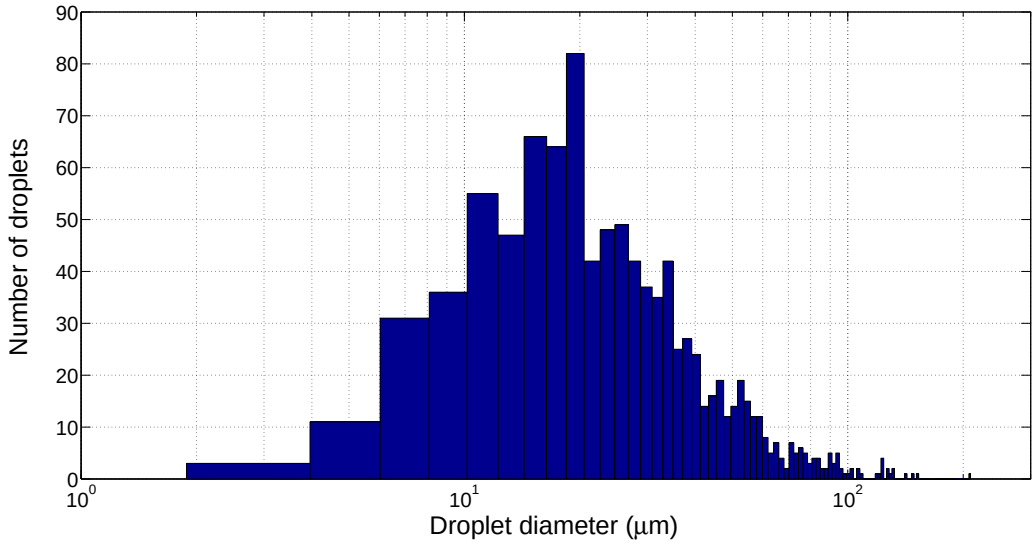

Figure 2.2 A randomly generated log-normal droplets distribution

In 1981, O'Rourke proposed a collision model based on a statistical approach [49]. This model

Table 2.2 Mean diameters in the spray of Fig. 2.2

Mean Diameter Name	Mean Value (μm)
Arithmetic Diameter (AMD)	32.0
Surface Area	39.8
Volume	48.6
Surface Area Length	49.6
Volume Length	59.9
Sauter Mean Diameter (SMD)	72.3
De Brouckere	96.9

did not require knowledge of the exact locations of any two colliding droplets as the probability of collision was computed statistically based on the local distribution of the droplets present. The model included only coalescence and grazing separation of droplets and so could not mimic other processes observed in binary collisions. Ashgris and Poo (1990) observed that droplet separation produced satellite droplets from the interacting region between two colliding droplets. Ashgriz and Poo extended the O'Rourke model and divided the separation process into the two classes of stretching and reflexive separation to account for the creation of satellite droplets [50]. Other researchers such as Qian and Law (1997), Estrade et al. (1999) and Brenn at al. (2001) also showed that satellite droplets are formed in these collision processes and that the average size of droplets decreases after collision [51–53].

2.5 Objectives of this Study

From the literature review, it appears that much empirical information is available about macroscopic features of sprays, such as their penetration lengths and spreading angles. Phenomena such as droplet evaporation also appear to be well understood for isolated spherical droplets. Less is known about microscopic features of sprays such as droplet size and velocity distributions, and few measurements of these quantities have been reported. While mechanisms of instability that promote the break-up of liquid jets into droplets have been identified, and models for the collision of two isolated droplets have been developed, it is not clear how well these models can be adapted to predict details of real sprays with many interacting, evaporating droplets. Nor is it clear how an unstable liquid jet develops into a spray with a particular spreading angle and droplet size distribution.

The objectives of this study are to make new experimental measurements in an impulsively

started fuel spray to address some of these unresolved issues and to test the abilities of proposed models to explain the behavior of real jets. In particular, it is planned to:

i) make new measurements of the effects of fuel delivery pressure on macroscopic spray characteristics;

ii) make new measurements of the dependence of droplet size distribution on distance from the spray nozzle;

iii) make new measurements of the effects of fuel temperature on spray characteristics and droplet size distribution;

iv) evaluate the adequacy of droplet evaporation models in explaining temperature-dependent effects on droplet size distribution

v) evaluate the utility of droplet collision models for explaining the dependence of droplet size distribution on downstream distance.

In addressing these objectives, the utility of single-droplet evaporation models and two-droplet collision models for describing entire sprays can be assessed. In the following chapters, the theoretical background and experimental setup are described and the droplet size distribution measurement techniques are explained in detail. Experimental measurements of fuel sprays are then reported and compared with numerical calculations of the development of n-heptane sprays.

Chapter 3

Theoretical Background

In this chapter, the theoretical background is presented for the basic physical processes that take place within liquid sprays. The processes include break-up, droplet transport, droplet collision and droplet evaporation.

3.1 Droplet Evaporation

Droplet evaporation is a two-phase flow phenomenon that can, in principle, be solved by using the three-dimensional continuity, Navier-Stokes, thermal energy and species conservation equations to describe both the liquid transport within each droplet and the flow of gas surrounding each droplet. These two equation systems can then be coupled by control-volume applications of the same principles to a thin region at the boundary of each droplet. However this approach is impractical as it would need enormous computational resources and is not currently used in spray studies. Instead, models have been introduced to make evaporation calculations more practical, though the simplifications they introduce limit their validity to particular classes of evaporation problems. Several of these models are described below, and introduced in order of increasing generality and complexity.

A droplet is a small, often spherical, volume of liquid bounded almost completely by a free surface. Both the size and the shape are influenced by the droplet's surface tension, which acts to minimize the droplet surface area, tending to produce a spherical shape for a given volume of

liquid. The process of droplet evaporation comprises two main phases [34]:

i) transport of fuel molecules from the surface of the droplet to gas in the immediate vicinity of droplets, through evaporation with surface recession; and

ii) diffusion and advection of fuel vapor from the surface of the droplet into the ambient gas.

In the case of droplets of mixtures of liquids, a third phase is present: the diffusion of liquid within the droplet as the surface concentrations of evaporating species change. The first phase is usually described by equilibrium thermodynamic relations relating the momentary concentrations in the liquid and vapor phase, such as the gas phase being saturated for pure droplets, or Raoult's law for droplets of liquid mixtures. The second phase is concerned with convective heat and mass transfer, usually with the assumption that the droplet retains its spherical shape, even when in motion [40, 41, 54] on account of the dominance of surface tension over inertia. It is also usually assumed that the temperature is uniform over the droplet surface though it can vary with time. It has been shown from three-dimensional internal flow calculations that isotherms often coincide with streamlines [55] in both stationary and fast-moving droplets, which justifies this assumption.

3.1.1 The d^2 Law

A simple model for describing the rate of evaporation of a droplet is the d^2 'law'. This model relationship can be thought of as describing a spherical droplet of a pure liquid in a stationary gas environment of constant temperature in time and space, equal to the liquid's wet-bulb temperature. Under these assumptions, it can be shown that the rate of decrease of the droplet's surface area is proportional to time [56], as

$$d^2 = d_0^2 - \lambda t, \tag{3.1}$$

where d is the droplet diameter at time t, d_0 is the initial droplet diameter and λ is an experimentally determined evaporation constant. This model is incomplete as it does not predict a value of λ and, even when a value of λ is provided from empirical sources, it is too simplistic to predict the size of droplets accurately under forced convection or in the final stages of evaporation, when surface tension becomes important. Fig. 3.1 shows experimental measurements of the non-dimensional droplet ratio value with time for pure methanol for near quiescent conditions at an ambient pressure of 1 atmosphere and a temperature of 300 K, together with a fit of the d^2 model.

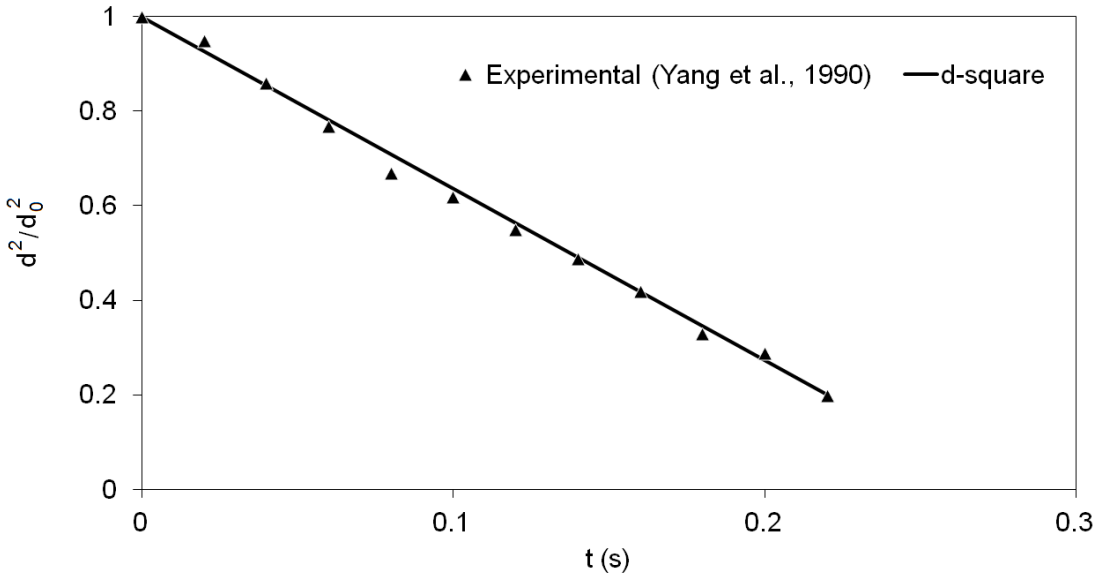

Figure 3.1 Temporal history of droplet diameter for evaporation of a methanol droplet [2]

3.1.2 The Spalding Mass-Number Model

Another way of modeling droplet evaporation is to define a mass transfer coefficient (h_m) such that

$$\dot{m}'' = h_m(\rho_{v_s} - \rho_{v_\infty}), \tag{3.2}$$

where $\dot{m}''$ is the mass flux of vapor at the droplet surface and ρ_{v_s} and ρ_{v_∞} are densities of vapor adjacent to and far from the droplet. For stationary droplets in a quiescent atmosphere, evaporation is controlled by the rate of diffusion of vapor and h_m is:

$$h_m = \frac{2D_g}{d_d}, \tag{3.3}$$

where D_g is the binary diffusion coefficient of fuel vapor in gas and d_d is the droplet diameter. For the general case of evaporation controlled by both diffusion and convection, a dimensionless mass transfer coefficient can be specified by a Sherwood number, defined as [57]:

$$Sh = \frac{d_d h_m}{D_g}, \tag{3.4}$$

$Sh = 2$ when droplet evaporation is driven only by molecular diffusion. For the more general case of evaporation driven by both convection and diffusion, correlations for Sh are usually developed from experimental or simulation data. One such correlation for Sh for moving evaporating droplets is [58]:

$$Sh = \left[2 + 0.87 Re_f^{1/2} Sc_f^{1/3}\right] \left(1 + B_M\right)^{-0.7}, \tag{3.5}$$

where

$$Re_f = \frac{U_d d_d}{\nu_f}, \tag{3.6}$$

$$Sc_f = \frac{\nu_f}{D_g}, \tag{3.7}$$

$$B_M = \frac{\rho_{v_s} - \rho_{v_\infty}}{\rho_{g_s}} = \frac{Y_{\nu_s} - Y_{\nu_\infty}}{1 - Y_{\nu_s}} \tag{3.8}$$

where Re_f is the Reynolds number at the film surrounding each droplet ($20 \leq Re_f \leq 2000$), Sc_f is the Schmidt number in the film region, B_M is the Spalding mass number and Y_{v_s} is the mass fraction at the droplet surface. It can be shown from [59] that:

$$Y_{\nu s} = \frac{1}{[1 + \frac{M_\infty}{M_f}(1 - \frac{P_\infty}{P_{\nu f}})]}, \tag{3.9}$$

where M_∞, M_f, P_∞ and P_{v_f} are the ambient gas and liquid molecular weights, and the ambient and liquid vapor pressure at the droplet surface respectively. The mass evaporation rate flux for a single droplet is

$$\dot{m}'' = \frac{d}{dt}\left(\frac{\frac{\pi}{6}\rho_d d_d^3}{\pi d_d^2}\right) = \frac{1}{6}\rho_d \frac{d}{dt}(d_d). \tag{3.10}$$

From Eqs. 3.2, 3.4 and 3.5, the rate of the droplet diameter decrease can be determined as:

$$d_d \frac{d}{dt}(d_d) = 6\rho_d \left[2 + 0.87 Re_f^{1/2} Sc_f^{1/3}\right] \left(1 + B_M\right)^{-0.7} \; Dg \; \left(\rho_{v_s} - \rho_{v_\infty}\right). \tag{3.11}$$

This ordinary differential equation can be integrated to yield $d_d(t)$ using standard numerical methods.

3.1.3 Coupled ODE Models

Simple models for heating and evaporating of non-isothermal droplets have also been developed. Some models are based on approximations of the temperature and concentration profiles inside droplets as their steady-state forms, which results in ODEs for droplet diameter, and average temperature and species concentration. For a spherically symmetric droplet of a pure liquid, the un-

steady one dimensional heat conduction equation inside the droplet can be written as:

$$\rho_l c_l \frac{\partial T}{\partial t} = \frac{k_l}{r^2}\frac{\partial}{\partial r}(r^2\frac{\partial T}{\partial r}), \tag{3.12}$$

where ρ_l, c_l and k_l are the liquid droplet density, heat capacity and thermal conductivity respectively (assumed to be constant). r is the distance from the center of droplet, t is time and T is the droplet temperature. If the droplet is heated by convection from the surrounding gas, and has a constant surface temperature T_s equal to the saturation temperature T_{sat}, the boundary condition at the droplet surface can be written as:

$$h\left(T_g - T_{sat}\right) = \rho_l L\dot{R} + k_l\left(\frac{\partial T}{\partial r}\right)_{r=R}, \tag{3.13}$$

where h is the convection heat transfer coefficient, L is the specific heat of evaporation and T_g is the ambient gas temperature. If a quasi-steady (parabolic) form of the temperature profile inside the droplet is assumed [60]:

$$T = T_c + (T_{sat} - T_c)\left(\frac{r}{R}\right)^2, \tag{3.14}$$

where T_c is the temperature at the center of droplet and R is the droplet radius. Integrating both sides of Eq. 3.12 with respect to r yields

$$\rho_l c_l \int_{r=0}^{R} \frac{\partial T}{\partial t} r^2 dr = k_l R^2 \left(\frac{\partial T}{\partial r}\right)_{r=R}. \tag{3.15}$$

Taking the derivative of Eq. 3.14 with respect to t and r respectively yields

$$\dot{T} = \dot{T}_c - \dot{T}_c\left(\frac{r}{R}\right)^2 + (T_{sat} - T_c)\frac{-2r^2\dot{R}}{R^3}, \tag{3.16}$$

$$\frac{\partial T}{\partial r} = \frac{2r}{R^2}\left(T_{sat} - T_c\right). \tag{3.17}$$

After substituting Eqs. 3.16 and 3.17 into Eq. 3.15 and simplifying:

$$\dot{R} = \frac{k_l}{R\rho_l L}\left[\frac{hR}{k_l}\left(T_g - T_{sat}\right) - 2\left(T_{sat} - T_c\right)\right]. \tag{3.18}$$

Given an initial value of the droplet diameter, Eq. 3.18 can be integrated numerically to obtain the droplet diameter at any time.

3.1.4 Coupled PDE Droplet Evaporation Models

The most sophisticated and expensive approaches to calculating droplet evaporation typically involve spherically symmetric treatments of multicomponent droplets in a gaseous environment. In this case the bulk continuity equation is:

$$\frac{\partial \rho}{\partial t} + \nabla.\left(\rho v\right) = 0, \tag{3.19}$$

$$\frac{\partial \rho_l}{\partial t} + \frac{1}{r^2}\frac{\partial}{\partial r}\left(r^2 \rho_l v_l\right) = 0, \tag{3.20}$$

where ρ and v are the gas phase density and velocity, respectively. Subscript l represents the properties of the droplet, while r is the droplet radius. The continuity equation for species i, assuming Fickian diffusion, can be written as

$$\frac{\partial(\rho y_i)}{\partial t} + \nabla.\left(\rho y_i v\right) = \nabla.\left(\rho D_i \nabla y_i\right) \tag{3.21}$$

$$\frac{\partial(\rho_l y_{l,i})}{\partial t} + \frac{1}{r^2}\frac{\partial}{\partial r}\left(r^2 \rho_l v_l y_{l,i}\right) = \frac{1}{r^2}\frac{\partial}{\partial r}\left(r^2 \rho_l D_l \frac{\partial y_{l,i}}{\partial r}\right) \tag{3.22}$$

The thermal energy equation is written as

$$\frac{\partial(\rho I)}{\partial t} + \nabla.\left(\rho I v\right) = \nabla.\left(\lambda \nabla T + \rho \sum h_i D_i \nabla y_i\right) - p\nabla.v \tag{3.23}$$

$$\frac{\partial(\rho_l T_l)}{\partial t} + \frac{1}{r^2}\frac{\partial}{\partial r}\left(r^2 T_l \rho_l v_l\right) = \frac{1}{c_p r^2}\frac{\partial}{\partial r}\left(r^2 \lambda_l \frac{\partial T_l}{\partial r}\right) + \frac{\rho_l D_l}{c_p r^2}\sum\nolimits_{i_{fuel}}\left[\frac{\partial}{\partial r}\left(r^2 h_{l,i}\frac{\partial y_{l,i}}{\partial r}\right) - h_{l,i}\frac{\partial}{\partial r}\left(r^2\frac{\partial y_{l,i}}{\partial r}\right)\right] \tag{3.24}$$

By integrating Eq. 3.21 over an infinitesimally thin control volume at the droplet surface, the interface condition for mass fraction of species i can be derived as:

$$\left[\rho_{ls}\left(v_{ls} - v_s\right)\left(y_{gs,i} - y_{l,i}\right) + \rho_{ls} D_{l,i}\nabla y_{ls,i} - \rho_{gs} D_{g,i}\nabla y_{gs,i}\right].\hat{n} = 0 \tag{3.25}$$

$$\rho_{ls}\left(v_{ls} - \dot{r}_s\right)\left(y_{gs,i} - y_{l,i}\right) + \rho_{ls} D_l\left(\frac{\partial y_i}{\partial r}\right)_{ls} - \rho_{gs} D_{g,i} Sh_{g,i}\left(\frac{y_{g\infty,i} - y_{gs,i}}{2r_s}\right) = 0 \tag{3.26}$$

Since the total mass fraction is equal to 1, the following constraint can be applied:

$$\sum_{i_{fuel}} y_{l,i} = 1 \tag{3.27}$$

together with [48]:

$$\sum_{i_{fuel}} D_{l,i}\nabla y_{l,i} = 0 \tag{3.28}$$

A summation over all species i of Eq. 3.25 yields:

$$\left[\rho_{ls}\left(v_{ls} - v_s\right)\left(y_{gs,F} - 1\right) - \rho_{gs}\sum_{i_{fuel}} D_{g,i}\nabla y_{gs,i}\right].\hat{n} = 0 \tag{3.29}$$

By manipulating Eqs. 3.23 and 3.25, the energy conservation at the interface can be expressed as:

$$\left\{ \sum_i L_{is} \rho_{ls} \left[- \left(v_{ls} - v_s \right) y_{ls,i} + D_l \nabla y_{ls,i} \right] + \lambda_{gs} \nabla T_{gs} - \lambda_{ls} \nabla T_{ls} \right\} .\hat{n} = 0 \tag{3.30}$$

For a spherically symmetric droplet, Eq. 3.29 is an equation for the surface regression rate:

$$\dot{r}_s - v_{ls} = \frac{\rho_{gs} \sum_{i_{fuel}} D_{g,i} Sh_{g,i} \left(y_{g\infty,i} - y_{gs,i} \right)}{2 \rho_{ls} r_s \left(y_{gs,F} \right)} \tag{3.31}$$

An interface condition on temperature can be derived from Eq. 3.30 as follows [48]:

$$\left\{ \sum_i L_{is} \rho_{ls} \left[\left(\dot{r}_s - v_{ls} \right) y_{ls,i} + D_l \left(\frac{\partial y_i}{\partial r} \right)_{ls} \right] - \lambda_l \left(\frac{\partial T}{\partial r} \right)_{ls} + \lambda_g N u_g \frac{T_{g\infty,i} - T_s}{2 r_s} \right\} = 0 \tag{3.32}$$

This system of equations can then be solved, together with a temperature-dependent library of liquid properties, using a PDE solver for the governing equations inside the droplet, and a root-finding procedure such as Broyden's method for matching the PDE and control-volume-obtained surface conditions to obtaine detailed solutions of the rate of recession of the droplet surface and the changes in temperature and species profiles within the droplet as a function of time.

3.2 Spray Dynamics

3.2.1 Break-Up

In the atomization of a round liquid jet, a diverging spray forms at the nozzle exit. It is also the location of break-up of the liquid jet. The injected liquid stream becomes unstable to small disturbances over a wide range of conditions. While the precise mechanisms of break-up are still a

topic of research, liquid jet break-up is usually divided into different regimes that reflect differences in the shape of jets as the operating conditions are changed. Four main break-up regimes have been identified for a round liquid jet injected into a stagnant gas: the Rayleigh regime; the first wind-induced regime; the second-wind induced regime and the atomization regime [61]. Rayleigh break-up takes place at low liquid-stream velocity when small-amplitude disturbances on the liquid surface promote amplification interactions between the liquid and gas phases and initiate break-up of the liquid stream into droplets. In this regime, the droplet diameters are larger than the jet diameter and the break-up occurs several nozzle diameters downstream of the nozzle. The first wind- induced regime is similar to the Rayleigh regime except the droplet diameters are of the order of the jet diameter. For high speed liquid jets, it is believed that the growth of unstable short-wavelength surface waves results in break-up of the second wind-induced and atomization regimes. In the second wind-induced regime, droplet diameters are smaller than the jet diameter and even smaller in the atomization regime. In the atomization regime, break-up starts at the nozzle exit. In order to make a quantitative classification of the break-up regimes, the Ohnesorge number is introduced as the ratio of the inertia and surface tension forces:

$$Oh = \frac{We_l}{Re_l}, \tag{3.33}$$

where the Weber and Reynolds numbers are defined as

$$We_l = \frac{U^2 d\rho_l}{\sigma}, \tag{3.34}$$

$$Re_l = \frac{Ud\rho_l}{\mu_l}, \tag{3.35}$$

where ρ_l is the liquid density, σ is the liquid surface tension, μ_l is the liquid dynamic viscosity, U is the liquid jet velocity and d is the nozzle diameter. The so-called Ohnesorge diagram represents the different break-up regimes, which are shown together with the zone of Diesel injection applications in the following figure.

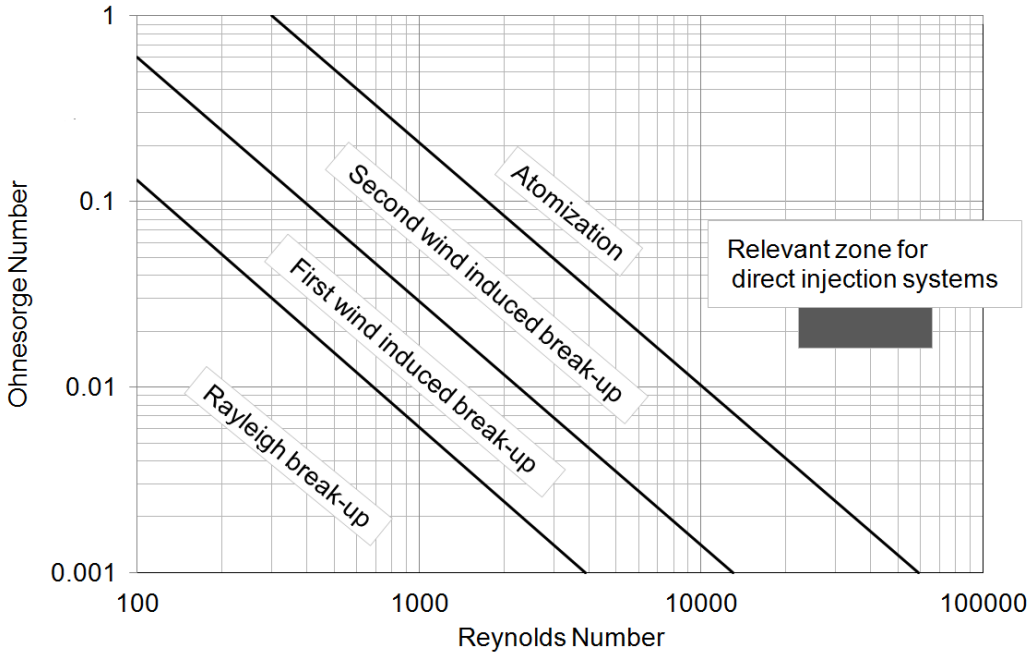

Figure 3.2 Ohnesorge diagram

In Diesel sprays, the primary break-up is the first disintegration of the coherent liquid into large droplets near the hole of the injector, and the secondary break-up takes place farther downstream. Fig. 3.3 is a schematic of the primary and secondary break-up in a typical Diesel spray. The physics of primary and secondary break-up are believed to be very complicated, and stochastic break-up models have been developed to generate a range of droplet sizes at high Weber numbers [62, 63].

3.2.2 Collision Models

In regions of sprays where droplet distribution is sparse, droplet size distribution is affected mainly by evaporation. However, at high Weber numbers and where the droplet distribution within the

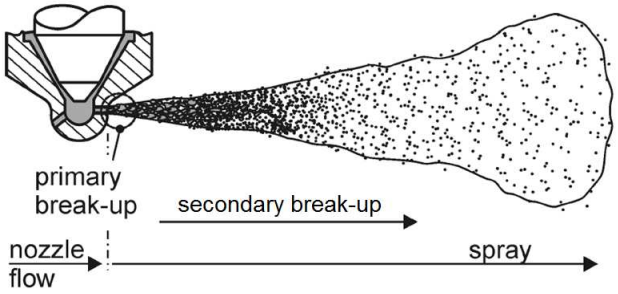

Figure 3.3 Diesel injection: primary and secondary break-up

spray is dense, collision processes can play an important role in the formation of the droplet size distribution. Although droplet break-up can be induced by interactions between spray and gas motion, droplet collision is the mutual impact of two droplets, caused by their differences in velocity and direction within a spray. As two droplets impinge, the region of gas separating them can be trapped as they collide, raising the gas pressure. When the relative velocity of droplets is not large enough to overcome the pressure forces between the droplets, they do not impinge but bounce apart. If the relative velocity is higher, droplets can collide and temporarily or permanently coalescence. At relatively low Weber numbers, the coalescence is permanent and the characteristics of the new bigger droplet can be obtained from the initial sizes and velocities of the droplets. At higher Weber numbers, temporary coalescence occurs and the excess kinetic energy of the droplets leads to their separation. Droplets that coalesce temporarily tend to undergo reflexive or stretching separation at low and high impact parameters respectively [50, 51].

One of the earliest work in droplet collision has been done by Rayleigh [64] who observed that small rain droplets bounce upon collision.

Several experimental studies have been performed on the different mechanisms of binary droplet collision. Ashgriz and Poo observed that both the reflexive and stretching separations produce satellite droplets from the interacting parts between two colliding droplets, and result in a size reduction in droplets [50]. The after-collision characteristics usually are described by the following

non-dimensional parameters [65]:

$$We = \frac{\rho d_1 U_{rel}^2}{\sigma}, \tag{3.36}$$

$$\Delta = \frac{d_1}{d_2}, \tag{3.37}$$

$$b = \frac{2B}{d_1 + d_2}, \tag{3.38}$$

where We is the Weber number based on droplet diameter, Δ is the droplet size ratio, b is the impact parameter, ρ and σ are the density and surface tension of the liquid phase, and the subscripts 1 and 2 represent smaller and larger droplets respectively. B is the distance from the center of one droplet to the relative velocity vector (U_{rel}) placed on the center of the other droplet, as shown in Fig. 3.4. For a head-on collision, the value of b is zero; *i.e.* the interaction height of the collision region is equal to the summation of the radii of the two droplets (see Eq. 3.38).

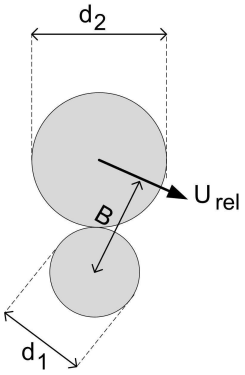

Figure 3.4 Parameters used to describe droplet collisions

3.3 Coalescence Criteria Calculation

In an attempt to predict the reasonable criteria for coalescence, it is assumed that the interaction of two spherical droplets of diameters d_1 , d_2 produces a spherical droplet of diameter d_0 rotating with an angular momentum Ω about its center of gravity.

$$d_0 = (d_1^3 + d_2^3)^{\frac{1}{3}}, \tag{3.39}$$

The criterion adopted is that separation occurs if the rotational energy exceeds the surface energy required to reform the two droplets from the coalesced droplets of diameter d_0. The moment of inertia I of a sphere rotating about its axis through its center can be written as

$$I = \int_{r=0}^{r=r_0} r^2 dm = \frac{8\pi}{15}\rho {r_0}^5 = \frac{\pi}{60}\rho {d_0}^5, \tag{3.40}$$

The rotational kinetic energy can be expressed by [66]

$$RE = \frac{\Omega^2}{2I} = \frac{10\pi\rho {U_{rel}}^2 B^2 d_1^6 d_2^6}{3d_0^{11}}, \tag{3.41}$$

where, RE is the rotational kinetic energy. The surface energy required to form two droplets of diameters d_1 and d_2 from a larger droplet of diameter d_0 and surface tension σ is given by [66]

$$SE = \pi d_1^2 \sigma \left[1 + \left(\frac{d_2}{d_1}\right)^2 + \left\{1 + \left(\frac{d_2}{d_1}\right)^3\right\}^{\frac{2}{3}}\right], \tag{3.42}$$

where, SE is the surface energy. Following the criterion of $RE = SE$,

$$b = \frac{4.8\sigma}{U_{rel}^2 d_1 \rho}\, f(\frac{d_2}{d_1}), \tag{3.43}$$

where, the dimensionless function $f(\frac{d_2}{d_1})$ is given by the equation

$$f\left(\frac{d_2}{d_1}\right) = \frac{\left[1+\left(\frac{d_2}{d_1}\right)^2+\left\{1+\left(\frac{d_2}{d_1}\right)^3\right\}^{\frac{2}{3}}\right]\left[1+\left(\frac{d_2}{d_1}\right)^3\right]^{\frac{11}{3}}}{\left(\frac{d_2}{d_1}\right)^6\left(1+\frac{d_2}{d_1}\right)^2} \tag{3.44}$$

3.4 The O'Rourke Collision Model

The O'Rourke model has been widely utilized in numerical studies of sprays and uses a statistical approach to predict the outcomes of collision events. This model only considers collisions of droplets that are in the same computational cell. Thus the collision frequency of larger droplets against all smaller ones is [67]:

$$\upsilon_{21} = \frac{N_1}{V_{cell}}\frac{\pi}{4}(d_1+d_2)^2 U_{rel}, \tag{3.45}$$

where V_{cell} is the cell volume. O'Rourke assumed a Poisson distribution of droplet sizes and showed that the probability of no collision was [49]:

$$P_0 = e^{(-\upsilon_{21}\Delta t)}. \tag{3.46}$$

In this model, three collision outcomes are considered: stretching separation with no generated satellite droplets; bounce; and permanent coalescence. A random number ξ is sampled from a uniform distribution between 0 and 1. If it is greater than the probability of no collision, collision takes place between the two droplets; otherwise no collision occurs because the two droplets bounce. The critical impact parameter that delineates permanent coalescence from stretching separation is shown in Fig. 3.5 [68]. The value of the critical impact parameter (CIP) is estimated as

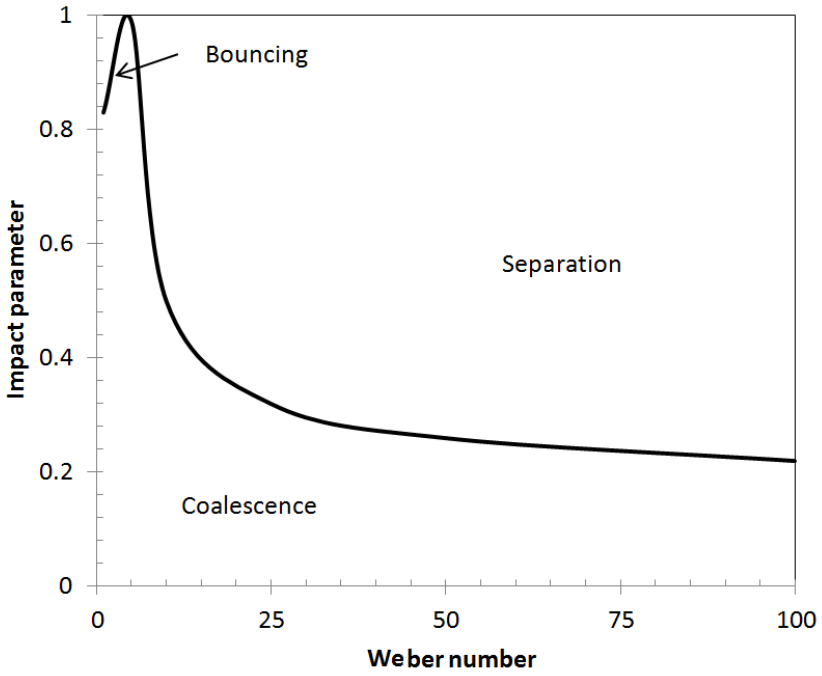

Figure 3.5 Effect of droplet diameter on coalescence–stretching separation in a binary collision of the same size droplets

the square root of ε_{coal}, where ε_{coal} is the coalescence efficiency and is defined as:

$$\varepsilon_{coal} = min\left\{1,\ \frac{2.4}{We_s}\left(\frac{1}{\Delta^3} - \frac{2.4}{\Delta^2} + \frac{2.7}{\Delta}\right)\right\}, \tag{3.47}$$

$$We_s = \frac{\rho U_{rel}^2 (d_1 + d_2)}{2\sigma}, \tag{3.48}$$

where We_s is the Weber number based on the amplitude of the relative velocity and the diameter of each droplet. If a random number between 0 and 1 is greater than the CIP, stretching separation with no generated satellite droplets takes place. Otherwise it is considered to be a permanent coalescence. The conservation of mass and momentum equations require the post-collision properties of the permanent coalescence regime to be:

$$d_{new} = \left(d_1^3 + d_2^3\right)^{\frac{1}{3}}, \tag{3.49}$$

$$U_{new} = \frac{d_1^3 U_1 + d_2^3 U_2}{d_{new}^3}, \tag{3.50}$$

where the subscript new denotes the value after collision. In a stretching separation that generates no satellite droplets, both droplets are assumed to retain their size. The velocities of the droplets after collision can be obtained from the energy and momentum conservation equations as:

$$U_{new,\,i} = \frac{d_i^3 U_i + d_j^3 U_j + d_j^3 \left(U_i - U_j\right) \left(\frac{b - \sqrt{\varepsilon_{coal}}}{1 - \sqrt{\varepsilon_{coal}}}\right)}{d_i^3 + d_j^3},\ i, j \in \{1, 2\},\ i \neq j. \tag{3.51}$$

In the bouncing process, bounced droplets preserve their original diameters, while their velocities are obtained from the momentum conservation equation:

$$U_{new,\,i} = \frac{d_i^3 U_i + d_j^3 U_j + d_j^3 \left(U_i - U_j\right)}{d_i^3 + d_j^3},\ i, j \in \{1, 2\},\ i \neq j. \tag{3.52}$$

3.5 Modeling the Generation of Satellite Droplets

Although the O'Rourke model only permits permanent coalescence between two droplets, many researchers have shown that satellite droplets are formed after collision [50–52] and that stretching and reflexive separation may take place. Models that include these effects are described briefly below.

3.5.1 Stretching Separation with Generated Satellite Droplets

Visualization data reported by Ashgriz and Poo [50] and Qian and Law [51] suggested that, during the stretching separation process, a portion of the interaction volume forms satellite droplets while the rest remains in the original colliding droplets. Therefore when two droplets experience stretch-

ing separation, the interacting portion between them creates a ligament which ultimately forms satellite droplets, whereas the non-interacting portion creates two droplets called 'head droplets.' According to Ashgriz and Poo [50], when two droplets collide at a high impact parameter, only a fraction of them come into direct contact, as shown in Fig. 3.4. This fraction can be calculated as:

$$\begin{cases} \theta_1 = \Omega_1 C_{VS} \\ \theta_2 = \Omega_2 C_{VS} \end{cases} \tag{3.53}$$

$$\Omega_1 = \begin{cases} 1 - \frac{1}{4\Delta^3}(2\Delta - \tau)^2 (\Delta + \tau) & for\ h > \frac{d_1}{2} \\ \frac{\tau^2}{4\Delta^3}(3\Delta - \tau) & for\ h < \frac{d_1}{2} \end{cases} \tag{3.54}$$

$$\Omega_2 = \begin{cases} 1 - \frac{1}{4}(2 - \tau)^2 (1 + \tau) & for\ h > \frac{d_2}{2} \\ \frac{\tau^2}{4}(3 - \tau) & for\ h < \frac{d_2}{2} \end{cases}, \tag{3.55}$$

where h, V, Δ and b are the interaction height, droplet volume, size ratio of droplets and impact parameter, respectively and

$$\tau = (1 - b)(1 + \Delta), \tag{3.56}$$

$$h = \frac{(d_1 + d_2)(1 - b)}{2}. \tag{3.57}$$

Mannannur and Reitz [69] proposed a separation volume coefficient to determine the temporal creation of a ligament that is composed of the interacting volumes of the two droplets. The separating volume is smaller than the interaction volume. To account for these phenomena, the present model defines the separation volume coefficient by assuming that the separating volume is proportional to the ratio of the energy required for separation to the total energy of the two droplets. The separation volume coefficient of stretching collision is defined as:

$$C_{VS} = \frac{E_{st} - E_{ten} - E_{dis}}{E_{st} + E_{ten} + E_{dis}}, \tag{3.58}$$

where E_{st} is the total kinetic energy, E_{ten} is the surface tension energy in the interacting area, and E_{dis} is the viscous dissipation, often assumed to be 30% of the total kinetic energy [69].

$$E_{st} = \frac{1}{2}\rho U_{rel}^2 \left(\frac{\pi}{6} d_1^3\right) \left[\frac{\Delta^3}{\left(1+\Delta^3\right)^2}\right] \left[1 + \Delta^3 - \left(1 - b^2\right)\left(\Omega_1 + \Delta^3 \Omega_2\right)\right], \tag{3.59}$$

$$E_{ten} = \sigma \sqrt{d_1 \tau \left(\Omega_1 + \Delta^3 \Omega_2\right) 2\pi \left(\frac{\pi}{6} d_1^3\right)}. \tag{3.60}$$

According to Munnannure and Reitz [69], the first shape of the interacting area after the collision is a cylindrical ligament. Fig. 3.6 shows the process of stretching separation and ligament and satellite-droplet formation. The mass conservation equation for the stretching separation with a ligament is written as:

$$\frac{\pi}{6} d_1^2 + \frac{\pi}{6} d_2^2 = \left(1 - \Omega_1\right) \frac{\pi}{6} d_1^2 + \left(1 - \Omega_2\right) \frac{\pi}{6} d_2^2 + \pi r^2 L. \tag{3.61}$$

The diameter of the two 'head droplets' after the separation can be written as:

$$d_{1af} = \left[\left(1 - \Omega_1\right) d_1^3\right]^{\frac{1}{3}}, \tag{3.62}$$

$$d_{2af} = \left[\left(1 - \Omega_2\right) d_2^3\right]^{\frac{1}{3}}, \tag{3.63}$$

where subscript af indicates the status of droplet properties after collision. The velocities of the

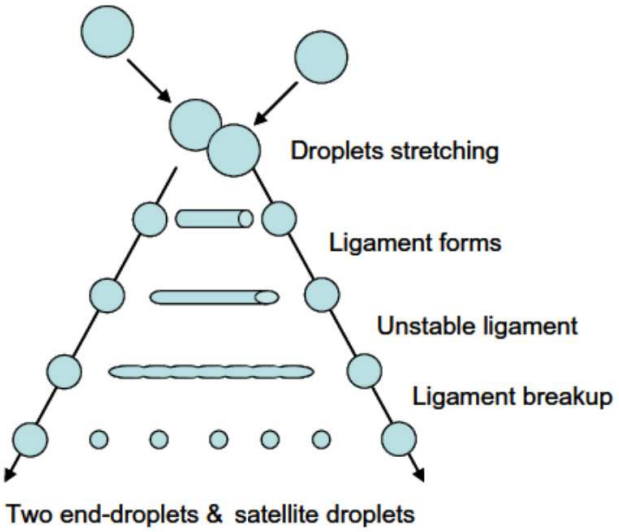

Figure 3.6 The stretching separation process

'head droplets' can be calculated from Eq. 3.11. Assuming the separation process takes place rapidly enough, no heat or work transfer takes place and so the conservation of energy equation can be expressed as:

$$\frac{1}{2}\rho\frac{\pi}{6}\left(d_1^3U_1^2+d_2^3U_2^2\right)+\pi\sigma\left(d_1^2+d_2^2\right)=\frac{1}{2}\rho\frac{\pi}{6}\left(\left(1-\Omega_1\right)d_1^3U_1^2+\left(1-\Omega_2\right)d_2^3U_2^2\right)+$$
$$\rho\frac{1}{2}\pi r^2\delta U_r+\pi\sigma d_{1af}\left(\frac{d_{1af}}{2}+\sqrt{\frac{d_{1f}^2}{4}-r^2}\right)+$$
$$\pi\sigma d_{2af}\left(\frac{d_{2af}}{2}+\sqrt{\frac{d_{2f}^2}{4}-r^2}\right)+\sigma 2\pi r\delta+\varphi, \tag{3.64}$$

where φ is the viscous dissipation, r is the cylindrical ligament radius, δ is the ligament length, and U_r is the average velocity of the fluid inside the ligament. In this model, it is assumed that the droplet velocities (before and after collision) and the volume of the ligament are independent of time. Also the radius of the ligament is assumed to be much smaller than the diameters of droplets

after collision. Making these assumptions and differentiating Eq. 3.64 with respect to time,

$$\left(U_r^2\right)^{\cdot} - \frac{4\sigma\dot{r}}{\rho r^2} + \frac{2\dot{\varphi}}{\rho\pi r^2\delta} = 0, \tag{3.65}$$

where $\dot{}$ denotes a derivative with respect to time. The initial shape of the mass that connects the bulbous end-drops is assumed to be a uniform cylinder of length equal to its radius, so

$$\pi r^2\delta = \pi r_0^2 r_0, \tag{3.66}$$

where r_0 is the initial radius of the ligament

$$r_0 = \left[\frac{1}{6}\left(\Omega_1 d_1^3 + \Omega_2 d_2^3\right)\right]^{1/3}. \tag{3.67}$$

The average fluid velocity in the stretching ligament is assumed to be proportional to the rate of stretching so

$$U_r = C\dot{\delta}, \tag{3.68}$$

where C is a constant assumed to be unity [70]. The viscous dissipation rate for a pure extensional flow can be given by [69]:

$$\dot{\varphi} = \frac{\pi r^2\mu\dot{\delta}^2}{2\delta}. \tag{3.69}$$

Substituting from Eq. 3.65 and 3.68, we find that

$$\ddot{r} = \frac{3\dot{r}^2}{r} + \frac{r^4}{2\rho r_0^6}\left(\sigma - \mu\dot{r}\right), \tag{3.70}$$

Mannunnar and Reitz showed that, as an alternative to solving the non-linear differential Eq. 3.30,

an approximation solution can be found by obtaining the non-dimensional radius R of the following equation [69]:

$$\frac{3}{4\sqrt{2}}k_1 k_2 We_0^{0.5} R^{3.5} + R^2 - 1 = 0, \tag{3.71}$$

where k_1 and k_2 are constants for the specific conditions. The diameter of the generated satellite droplets is given by:

$$d_{sat} = 3.78 r_0 R. \tag{3.72}$$

The number of satellite droplets generated is:

$$N_{sat} = \frac{3}{4}\left(\frac{r_0}{r_{sat}}\right)^3 \tag{3.73}$$

The velocity of the satellite droplets can also be found from the conservation of momentum.

3.5.2 Reflexive Separation and Generation of Satellite Droplets

Tennison et al. considered reflexive separation as an additional outcome when the Weber number defined in Eq. 3.36 is greater than a critical Weber number of

$$We_{crit} = \frac{3\left[7\left(1+\Delta^3\right)^{\frac{2}{3}} - 4\left(1+\Delta^2\right)\right]\Delta\left(1+\Delta^3\right)^2}{\Delta^6\eta_1 + \eta_2}, \tag{3.74}$$

where

$$\eta_1 = 2(1-\beta)^2\sqrt{1-\beta^2} - 1, \tag{3.75}$$

$$\eta_2 = 2(\Delta-\beta)^2\sqrt{\Delta^2-\beta^2} - \Delta^3, \tag{3.76}$$

$$\beta = \frac{1}{2}b\left(1+\Delta\right). \tag{3.77}$$

Fig. 3.7 shows the droplet formation process of reflexive separation. As can be seen from this figure, all satellite droplets generated from the separation are assumed to have the same size, so no head-droplet is formed in this process.

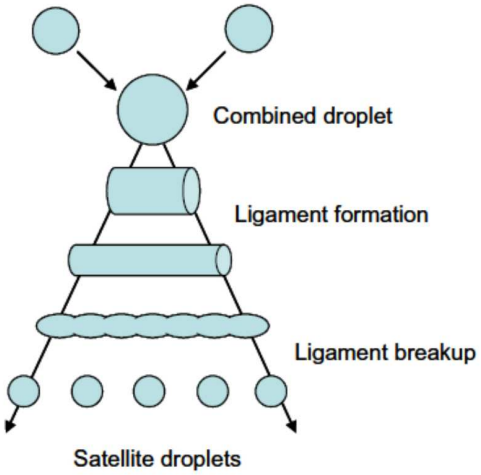

Figure 3.7 The process of reflexive separation

The velocity of the satellite droplets in reflexive separation can be obtained from Eq. 3.51.

$$U_{new,\,i} = \frac{d_i^3 U_i + d_j^3 U_j + d_j^3 \left(U_i - U_j\right) \sqrt{1 - \frac{We_{crit}}{We_s}}}{d_i^3 + d_j^3},\ i, j \in \{1, 2\},\ i \neq j. \tag{3.78}$$

The diameter of the satellite droplets can be calculated from Eq. (3.31) and (3.32) with the initial ligament radius of:

$$r_0 = \left[\frac{1}{8}\left(d_1^3 + d_2^3\right)\right]^{\frac{1}{3}}. \tag{3.79}$$

3.6 Single Droplet Trajectories

Predictions of the trajectory of a discrete-phase droplet can be obtained by integrating the force balance on the droplet, written in a Lagrangian reference frame. The inherent three-dimensional

character of the droplets is accounted for through an aerodynamic drag force. As a particle moves through the fluid, it experiences a force equivalent to the composite drag force of the droplets moving relative to the ambient fluid. Inter-droplet effects on the aerodynamic drag are neglected. The force balance equates the droplet inertia with the forces acting on the droplet and, in the z direction, can be written as

$$\frac{dU_p}{dt} = F_D\left(U - U_p\right) + \frac{g\left(\rho_p - \rho\right)}{\rho_p} + F_z, \tag{3.80}$$

where F_D ($U - U_p$) is the drag force per unit droplet mass and

$$F_D = \frac{18\mu}{\rho_p d_p^2}\frac{C_D Re}{24}, \tag{3.81}$$

where U is the environmental gas phase velocity, U_p is the droplet velocity, μ is the gas phase viscosity, ρ_g is the gas density, ρ_p is the droplet density, and d_p is the droplet diameter. Re is the Reynolds number, which is defined as

$$Re = \frac{\rho d_p \left|U_p - U\right|}{\mu}. \tag{3.82}$$

The drag coefficient, C_D can be found from

$$C_D = a_1 + \frac{a_2}{Re} + \frac{a_3}{Re^2}\,, \tag{3.83}$$

where a_1, a_2 and a_3 are constants that apply for smooth spherical particles over several ranges of Re given by Morsi and Alexander [3]. Figure 3.8 shows the drag coefficient diagram for these ranges of Reynolds numbers.

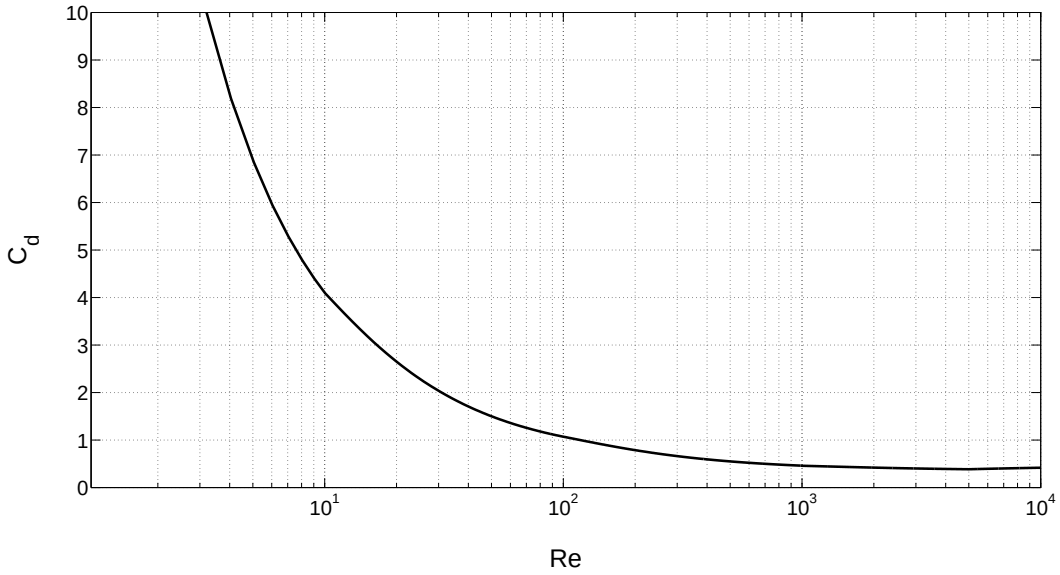

Figure 3.8 Drag of a spherical droplet over a range of Reynolds numbers [3].

These models for the behavior of droplets undergoing collisions will be examined in later sections of this dissertation. They will be used to determine how well experimental measurements of droplet size distributions in sprays can be explained by droplet collision theories. The evaporation models will be used to assess whether evaporation is a significant contributor to changes in droplet size measured along the axis of a spray.

Chapter 4

Experimental Methods

In this chapter, the experimental apparatus used to spray fuel in a controlled manner, and to measure the macroscopic features of the spray and the droplet size distribution is described. The apparatus consists of five main parts: the fuel delivery system; the injector control system; the fuel heating system; the macroscopic visualization system; and the droplet size measurement system. Fig. 4.1 shows a schematic of the experimental setup. A fuel injector is supplied with fuel from a pressurized tank through a fuel line. A computer control system is used to set injection parameters such as time duration and time delay after a timing pulse, to allow a specified volume of fuel to be injected/sprayed. A capability was also provided to heat the fuel in the line upstream of the injector, to explore effects of fuel temperature on spray behavior. A high speed CCD camera was used to record the spray propagation into quiescent surroundings which, after image processing, could be used to make macroscopic characterizations of the spray. A Spraytec diffraction-based laser droplet sizing system was used to determine microscopic spray characteristics such as droplet size distribution. Each of these components is described in detail in the following sections.

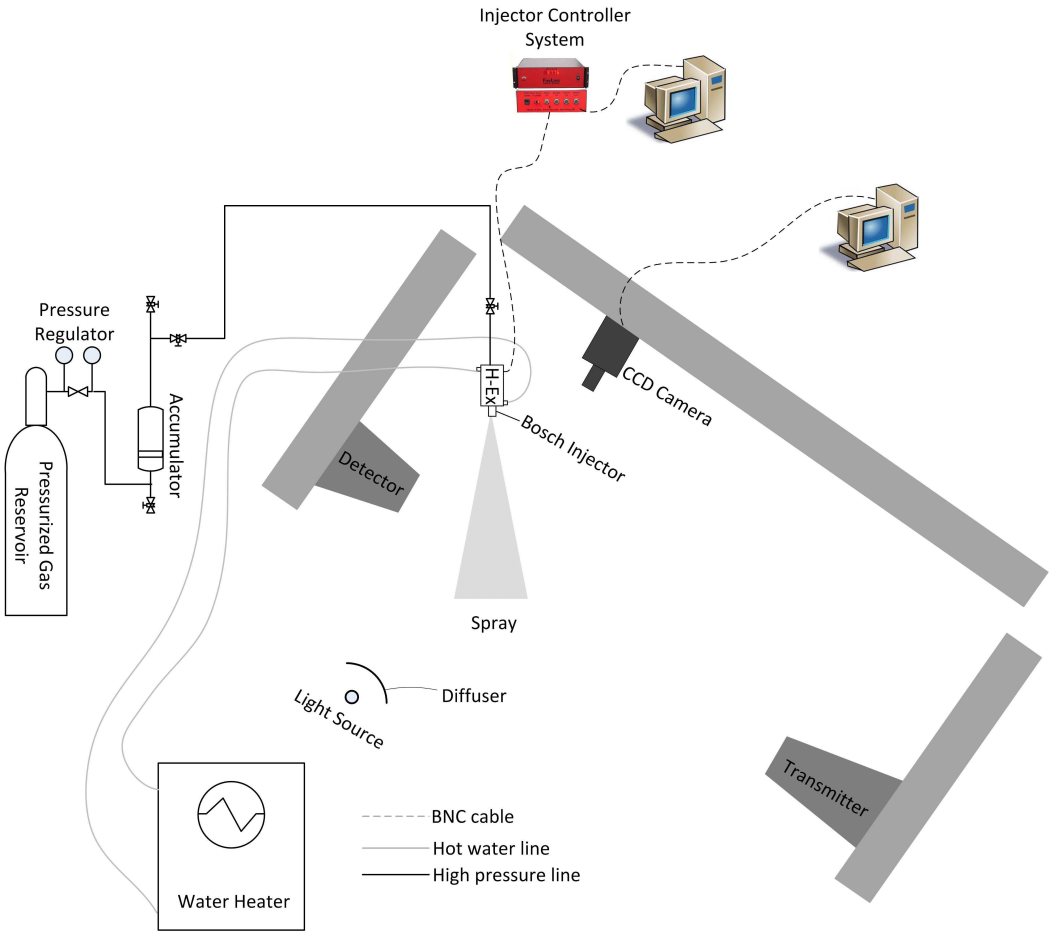

Figure 4.1 Schematic of the present experimental setup

4.1 Fuel Delivery System

In these series of experiments n-heptane was used as the fuel. The fuel delivery system is shown in Fig. 4.1. To supply fuel to the injector, a cylinder of nitrogen is used to pressurize the fuel tank at a pressure controlled by the cylinder regulator. A second pressure gage is installed on the fuel tank, which comprises two chambers. One contains liquid fuel and its outflow is connected to the injector supply line. The other is a compressed gas accumulator—a cylinder with two chambers that are separated by a floating piston—connected to the nitrogen reservoir. As the volume of the compressed gas changes, the pressure of the gas (and the pressure on the fluid) changes. An injector (in these series of experiments, a commercial Bosch Model PA66) is connected by a fuel line to the accumulator, so that its pressure provides a flow of fuel when the needle of the injector is energized. This injector is a type of commercial injectors used in common rail fuel injection system which usually operates at pressures between 100 and $300\ MPa$. The original injector was a 7-hole type with a $0.3\ mm$ each hole diameter. In order to study the pure single plunge spray development, 6 holes were blocked out by using a commercial super glue. Fuel is then sprayed from the injector. In order to refill the accumulator with fuel and change the injector, three high-pressure valves are positioned as shown in Fig. 4.1. With this system, the injector can operate over a range of pressures limited only by that of the nitrogen in the cylinder.

In Fig. 4.2, a typical heavy-duty fuel injector with electromagnetic fuel injection control is shown. This kind of fuel injector consists of three main parts: a solenoid spring; a control chamber; and a nozzle chamber. In the closed position, both the control and nozzle chambers are pressurized. Because the area above the control plunger is larger than the area of the nozzle chamber, there is a net closing force and so no fuel leaves the nozzle. When the solenoid is energized, the resulting magnetic force raises the ball valve and, because the z-throttle area is smaller than the A-throttle

area, the pressure in the control chamber drops. However, the nozzle chamber is still pressurized and so there is a net opening force that raises the control plunger. The needle tip is then raised and fuel is injected. When the solenoid is no longer energized, the solenoid spring pushes the ball valve to its original seat and terminates injection.

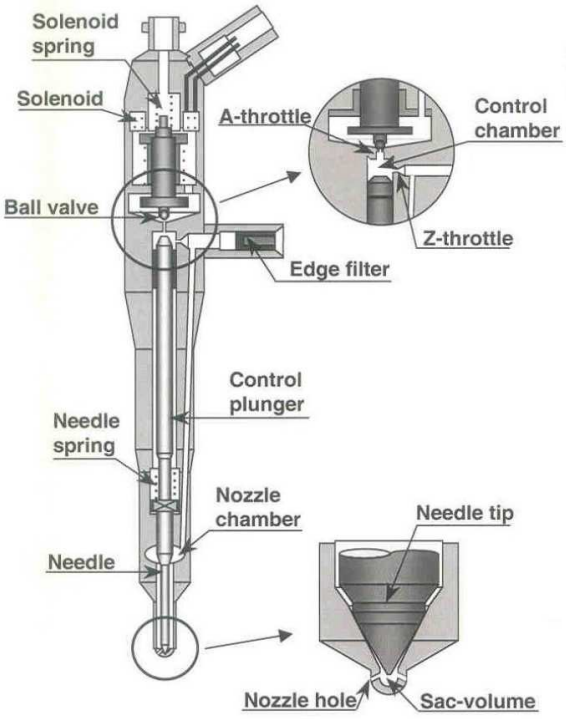

Figure 4.2 Schematic of a common rail fuel injector

4.2 Fuel Heating System

To investigate spray behavior at fuel temperatures above ambient, a heating system is used. As fuels are flammable, a high capacity water heater is used to raise the fuel temperature using a cross-flow heat exchanger. The circulating water passes through insulated lines and transfers heat to the injector. Table 4.1 shows the water heater specifications.

Table 4.1 Water heater specification

Item	Water Heater
Type	Residential
Tank (Gal)	10
Voltage	120
Phase	1
Total watts	2000
Number of elements	1
Height/Top of the heater (in)	23
Jacket diameter (in)	$15 - 3/4$
Water connection	$3/4 in NPT$
Temperature range	$90 to 220 F$
Weight (lb)	47.05
Model	1PZ78

4.3 Injection Controller System

A FireLynx engine controller system is used to customize the injection period and delay in these experiments. The FireLynx is a programmable engine controller designed to operate in environments from -40°C to +75°C with built-in over-voltage, over-current and over-temperature protection. This system also permits independent external waveform control of multiple injectors, with a temporal resolution of 0.01 ms. The output voltage to the injector can be scaled from the input supply voltage or the built-in 5 V power supply and the period of injection can take any value above 0.1 ms, however the injection pulse width was 2.4 ms in all experiments.

4.4 Macroscopic and Microscopic Visualization Systems

The optical techniques used in spray visualization can be divided into two sub-categories: direct imaging and non-imaging techniques. Direct imaging in direct injection spray diagnostics has focused on observation of the spray structure and geometry, such as spray cone angle, cluster break-up, and penetration length. Non-imaging optical techniques measure spatial and temporal

droplet size distribution and velocities.

4.4.1 Macroscopic Visualization System

Direct imaging is used for evaluating the macroscopic characteristics of a spray and consists of taking photographs with a charge-coupled device (CCD) camera to capture images of the spray or spray droplets. Illumination is carried out with a flashlight or pulsed laser, which creates a high intensity light source of short duration. The primary requirement in determining the spray geometric parameters is that the entire spray be imaged. A uniform light source, a diffuser, and a Photron CCD camera were configured to generate backlit images of the entire spray (Fig. 4.3). This camera can be used with different rates to record the spray development. For 10,000 and 300,000 frame per second rates, the resolution is 896X848 and 256X64 pixels, respectively. The corresponding physical resolution in images is approximately 51 μm/pixel. These footprints have 16 Bit gray color. To freeze the motion of the droplets in the spray, a triggered flash lamp with sub-microsecond duration was used.

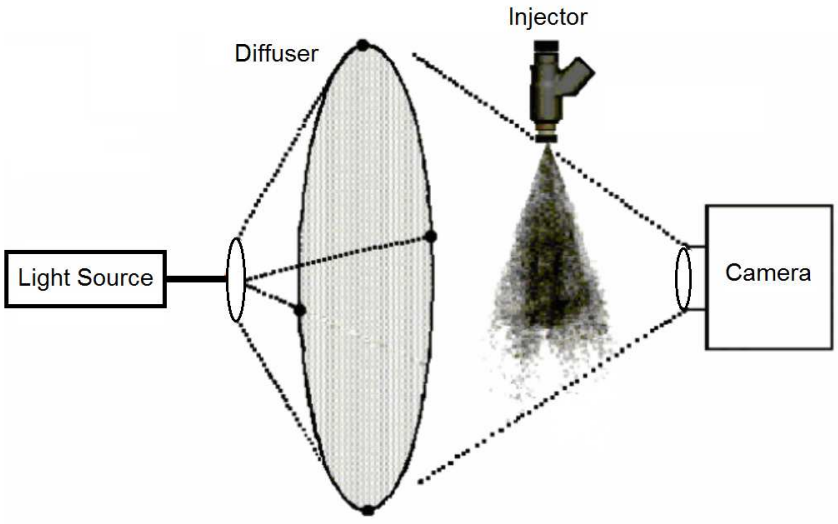

Figure 4.3 Schematic of the macroscopic visualization system

A continuous light source and a CCD camera with a very short exposure time were used to record spray images. The light and/or camera triggers were activated with time-delayed signals from an injector driver circuit. Additional electronic controls were used to synchronize and phase the injection, the light source and the camera shutter. As shown in Fig. 4.4, backlit illumination was used for uniform imaging of the spray and was effective for resolving the spray edges. To evaluate the principal spray parameters such as the spray angle and axial spray penetration distance, the edges of the spray were determined. To define the spray boundary, image processing techniques were used to distinguish between droplets at the spray boundary and optical noise.

Figure 4.4 Backlit image of a direct Diesel injection spray

4.4.2 Laplacian-Gaussian Edge Detection

Edge detection algorithms are commonly used for evaluating of the Diesel spray macroscopic characteristics properties. These algorithms find edges that form a closed contour and completely bound an object. The intensity of an image changes at the edges of a specific shape is shown in Fig. 4.5.

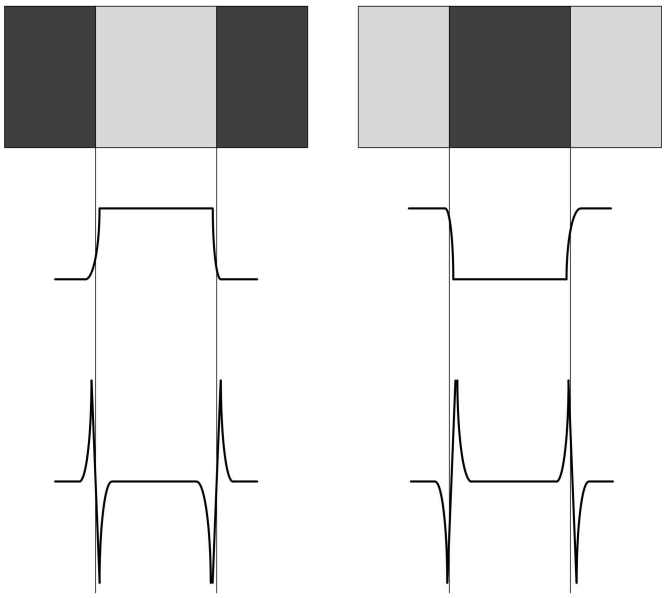

Figure 4.5 Intensity and spatial intensity derivative functions near the edges

If the intensity profile of an image changes continuously, it indicates the presence of an edge. The Laplacian is a 2-D isotropic measure of the second spatial derivative of an image and in 2-D images can be defined as:

$$\nabla^2 f(x,y) = \frac{\partial^2 f}{\partial x^2} + \frac{\partial^2 f}{\partial y^2}. \tag{4.1}$$

The Laplacian of an image highlights regions of rapid intensity change and therefore can be used for edge detection. However, as a second-order derivative, the Laplacian is very sensitive to noise and so is applied to images that have first been smoothed. This pre-processing step reduces the high frequency noise components prior to the differentiation step. One possible preprocessing tool is

the Gaussian smoothing. The Gaussian distribution function in two variables $g(x, y)$ is illustrated in Fig. 4.6 and is defined as

$$g\left(x,y\right)=\frac{1}{2\pi\sigma^{2}}e^{\frac{-(x^{2}+y^{2})}{2\sigma^{2}}}, \tag{4.2}$$

where s is the standard deviation representing the width of the Gaussian distribution. The shape of the distribution and hence the amount of smoothing can be controlled by varying s.

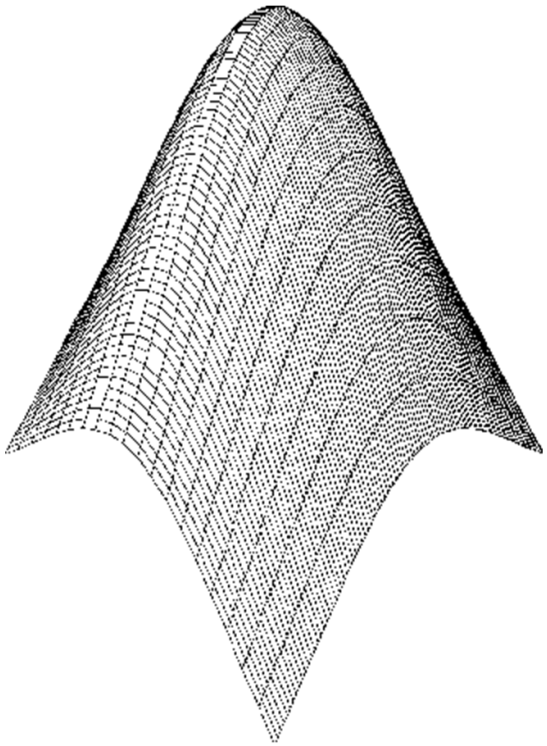

Figure 4.6 The Gaussian distribution in two variables

In order to smooth an image with the intensity function of $f(x, y)$, it is convolved with $g(x, y)$ to produce a smoothed image with the intensity function of $s(x, y)$.

$$s\left(x,y\right)=f\left(x,y\right)*g(x,y). \tag{4.3}$$

After smoothing the image with a Gaussian operator, the Laplacian of the smoothed image is taken,

which is equivalent to convolving the original image $f(x, y)$ with a Laplacian of a Gaussian (LOG) operator. Fig. 4.7 shows the LOG operator.

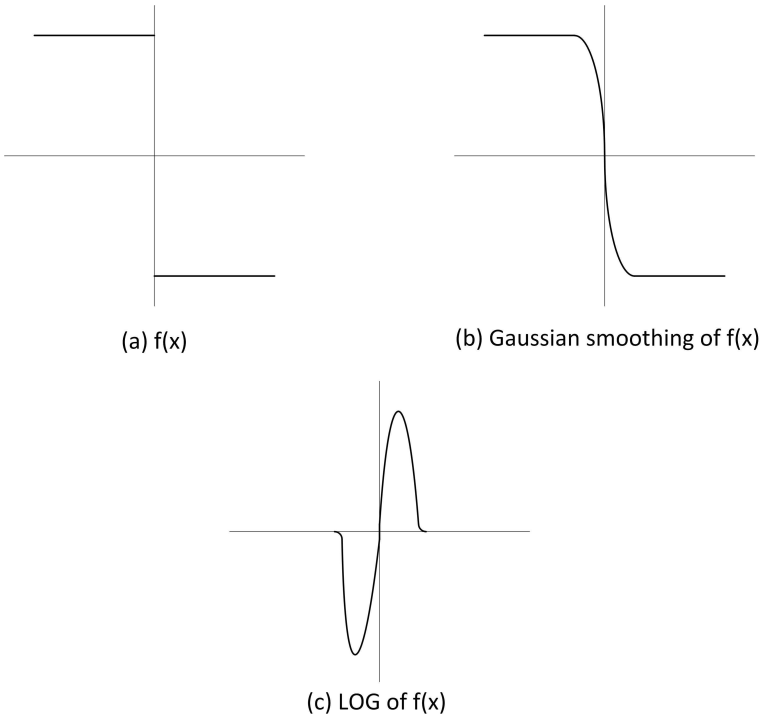

Figure 4.7 The LOG operator

The zero crossing is the location in a Laplacian of an image where the value of the Laplacian passes through zero. Such points often occur at the edges in images where the intensity of the image changes rapidly. Fig. 4.5 shows that in the approach to a change in intensity, the Laplacian response is positive on the darker side, and negative on the lighter side. Thus there is a sharp edge between two regions of uniform but different intensities and the Laplacian response is: zero at a long distance from the edge; positive just to one side of the edge; negative just to the other side of the edge; and zero at some point in between, on the edge itself. Once the image has been converted by the Laplacian of a Gaussian filter, the algorithm detects the zero crossings. Fig. 4.9 shows a Diesel spray shape before and after the image processing.

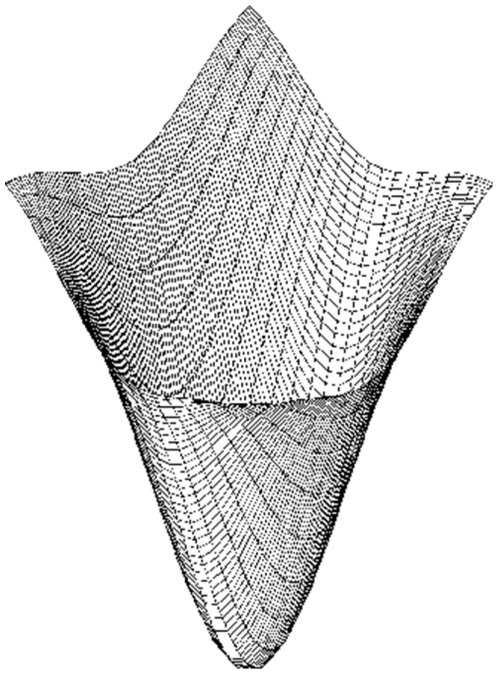

Figure 4.8 Steps of a LOG operator

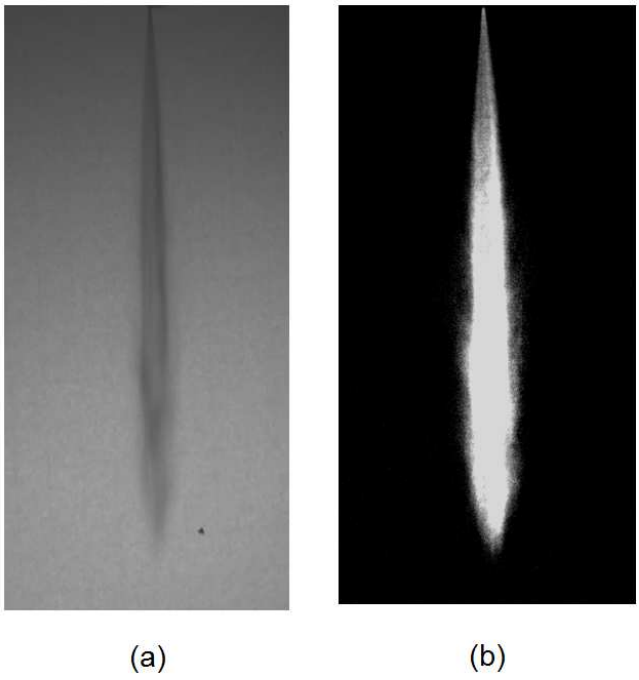

Figure 4.9 (a) n-heptane spray with rough edges before the image processing. (b) The same spray after implementing edge detection image processing

4.4.3 Microscopic Measurement Systems

Specialized laboratory instruments have been developed for measurement of droplets in automotive fuel sprays as laser diffraction instruments and phase-Doppler instruments. These laser-based instruments may be used to measure and record the sizes of droplets within fuel sprays. However, they do not necessarily give identical results in the same spray. Phase-Doppler systems measure the size distribution of a spray in a very small probe volume which is created at the intersection of two or more focused laser beams. Laser diffraction measures droplet size distributions by measuring the angular variation in intensity of light scattered as a laser beam passes through a dispersed droplet sample. Large droplets scatter light at small angles relative to the laser beam and small droplets scatter light at large angles, as illustrated in Fig. 4.10. The angular scattering intensity data is then analyzed to calculate the size of the particles responsible for creating the scattering pattern, using theories of light scattering. The droplet size is reported as a volume equivalent sphere diameter. Thus in laser diffraction methods, the size distribution result is obtained from the region of the spray within the laser beam cross section as opposed to the probe volume in phase-Doppler anemometry. The need to move the probe volume through numerous positions in the spray makes phase-Doppler measurements significantly more time consuming than laser diffraction ones. In both methods, the droplet sizing parameters obtained from the size distribution curves are the Sauter Mean Diameter (SMD) and the droplet diameters corresponding to the 50% or 90% cumulative volume point on the droplet size distribution curve: $Dv50$ and $Dv90$ respectively.

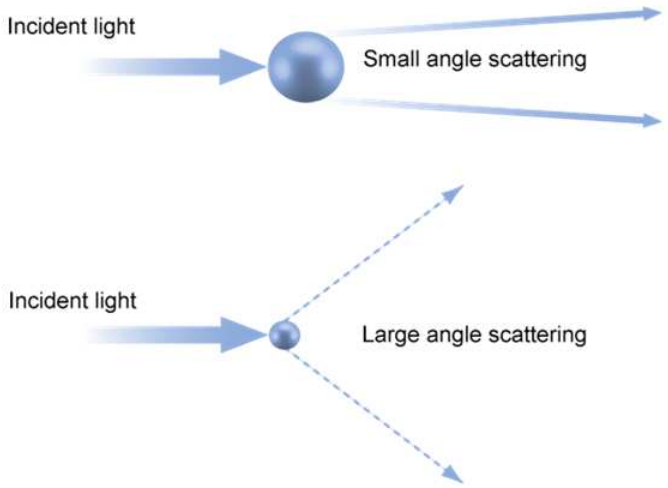

Figure 4.10 Scattering of light from small and large particles

4.4.4 Malvern Spraytec

The Malvern Spraytec was designed as a laser diffraction system to measure droplet size distributions from light scattered by the spray droplets in a cylindrical beam of laser light, as illustrated in Fig. 4.11. The light scatter from droplets is collected by the Spraytec after first taking a background measurement. The scattered light is then used to infer a spatially integrated droplet size distribution. The diffracted light from the droplets within the working distance and size range of the receiving optics is collected in an annular array of photo detectors and its intensity measured. The recorded scattering pattern is then analyzed using a Mie scattering model to yield a size distribution. The angular range over which scattering measurements are made has been optimized within the Spraytec to ensure poly-disperse size distributions are fully resolved. Particle size calculations are then carried out using a multiple scattering algorithm. This ensures accurate particle size distributions can be measured at up 98% obscuration, beyond the range of operation of traditional laser diffraction systems. To properly calculate the droplet size distribution, the software has the user input the optical properties of the material being measured. Laser diffraction systems yield

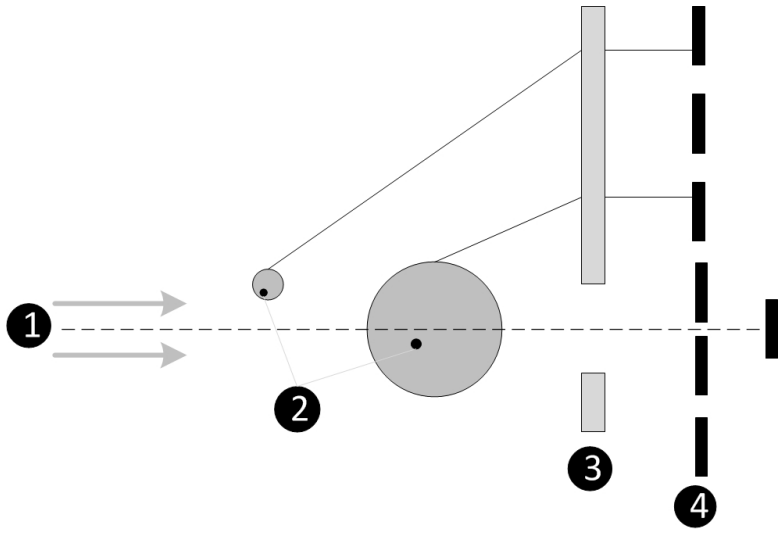

Figure 4.11 The Spraytec spray measurement

a size distribution measurement from scattering data coincident in time, as a single measurement from the entire scattering volume. No measurement of droplet velocity distribution was made. The main components of a Spraytec system are shown in Fig. 4.12.

Figure 4.12 Key components of a Spraytec system

4.4.5 Optical Support Bench (X-bar)

The optical support bench or X-bar supports the transmitter and receiver modules. The X-bar allows the transmitter and receiver can be moved to different positions, with the detector optics remaining aligned to the transmitter laser path.

4.4.6 Transmitter

The transmitter contains the laser source which produces a collimated beam of 14 mm diameter with a wavelength of 632.8 nm. The laser beam from the transmitter passes through the measurement zone within the spray, then through a lens and protective windows to the detector array in the receiver. The resultant scattered light is detected by the detectors in the receiver. When no spray is present in the measurement zone, the transmission level is 100$\%$. However, some light is blocked when droplets are present in the beam.

4.4.7 Receiver

The receiver holds the lens assembly and photodiode detector elements. A 300 mm lens focuses scattered light onto the detectors and by using Mie scattering theory, the size distribution of scattering droplets is determined. The receiver has 36 detectors that sense the scattered-light intensity of droplets as small as 0.5 μm. Mie scattering theory is applicable to homogeneous and spherical droplets of arbitrary size illuminated by plane waves [71]. According to Mie theory, the intensity of the scattered light which reaches an observer is a function of the incident light intensity and scattering function. Mie theory requires knowledge of the optical properties such as the refractive index of the droplet-gas interface. A typical Mie scattering pattern is shown in Fig. 4.13. Each bar in the histogram represents the scattered light captured by one of the detectors and so relates

directly to the size of the particles.

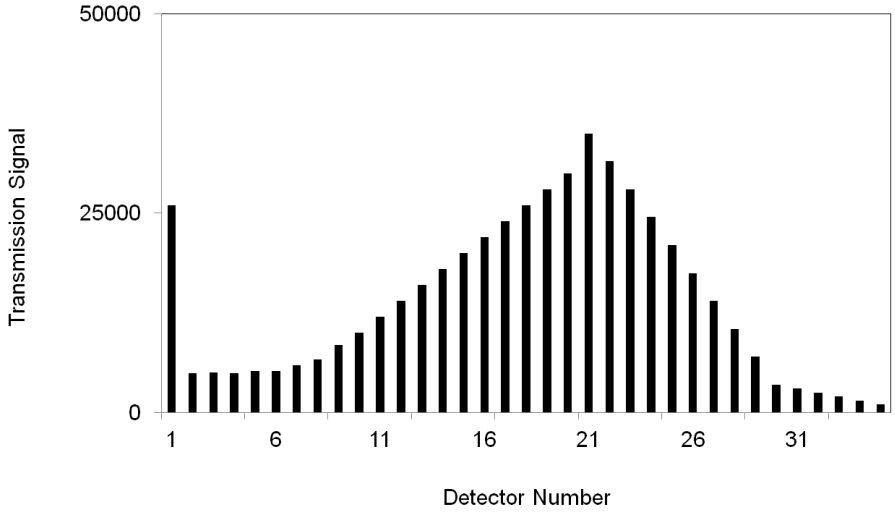

Figure 4.13 A snapshot of a scattering pattern of the detector array

4.5 Experimental Plan

The overall experimental plan is to make measurements of impulsively started fuel sprays under a range of controlled conditions that will provide new data for the design of fueling systems and target data for assessing the validity of droplet evaporation and droplet collision models in predicting the microstructure of sprays. Since diffraction-based measurements of droplet size distribution can only be made reliably well downstream of the nozzle, it is planed to make these measurements at a series of such locations along the spray axis. The size distribution data at the location closest to the nozzle can then be used as an initial condition for testing the ability of collision and evaporation models to predict the droplet size distribution at multiple locations further downstream. Since droplet evaporation is known to be sensitive to the temperature difference between the liquid and the surrounding gas, it is also planned to measure these data over a range of fuel temperatures, and so provide target data for testing the temperature sensitivity of evaporation models. The plan is

to make these measurements using n-heptane as the fuel because it is a pure substance with well known properties and is representative of gasoline.

The overall experimental plan is therefore:

i) Measure the shape and spray angle of n-heptane sprays under ambient conditions as a function of time and penetration distance, to describe their macroscopic structure;

ii) Carry out the measurements of *i*) for fuel temperatures at a controlled range of values above ambient to determine the effect of fuel temperature on macroscopic spray structure;

iii) Measure the droplet size distribution at the closest location to the nozzle at which reliable diffraction-based measurements can be made, as indicated by the light transmission efficiency, for use as an initial condition for testing evaporation and collision models and for characterizing the micro-structure of the spray;

iv) Measure the droplet size distribution at a series of downstream locations, and at on- and off-axis locations, to characterize the microstructure of the spray and provide target data for collision and evaporation models in sprays; and

v) Repeat the measurements of *iii*) and *iv*) at different fuel temperatures, to determine the effect of fuel temperature on spray microstructure and to provide target data for spray model testing.

Chapter 5

Experimental Results

In this chapter, experimental results are presented of the spray geometry and the size distribution of droplets in the far field of the spray. The liquid was chosen as n-Heptane, which is representative of gasoline, and an impulsively started spray was generated using a low pressure Bosch 7-hole injector with all but one hole blocked. This configuration was chosen as sprays from single orifices provide better target data for computational modeling than those from multiple orifices, as the complexity of merging sprays is avoided. The injector hole diameter was $0.3\ mm$. While injector actuation is almost perfectly repeatable from event to event, the nature of break-up is believed to depend on instability in the presence of small disturbances and so the subsequent evolution of sprays is stochastic in nature. For this reason, multiple measurements are made of each injection event so that both instantaneous and average data can be recorded. The reported droplet size distributions are time averaged during the spray event and include an average size distribution along the whole spray from the front edge to the tail.

5.1 Measurement Error and Malvern Instrument Calibration

To better understanding of the experiment results, it is important to calculate the order of magnitude of error in the experiments. In this study, spray tip penetration and angle are obtained by implementing image processing; explained in previous chapter; on the raw images. In order to

calculate the fuel spray tip penetration, the location of the injector tip and spray front edge are necessary, the maximum error of reading these locations can be 2 pixels as Fig. 5.1 shows. Since the maximum length of each pixel in the study is $50\ \mu m$, the maximum error in finding spray tip penetration is $0.1\ mm$. In the similar way, it is obvious that the maximum error of reading pixels for calculating spray angle is two pixels at 60 diameters downstream of the injector tip [1]. By using Eq. 5.1, it can be shown that the maximum error in reading the spray angle is almost $0.3\ ^{\circ}$.

$$\theta \approx \tan\theta = \frac{2 * 50}{60 * 300} rad \approx 0.3^{\circ} \tag{5.1}$$

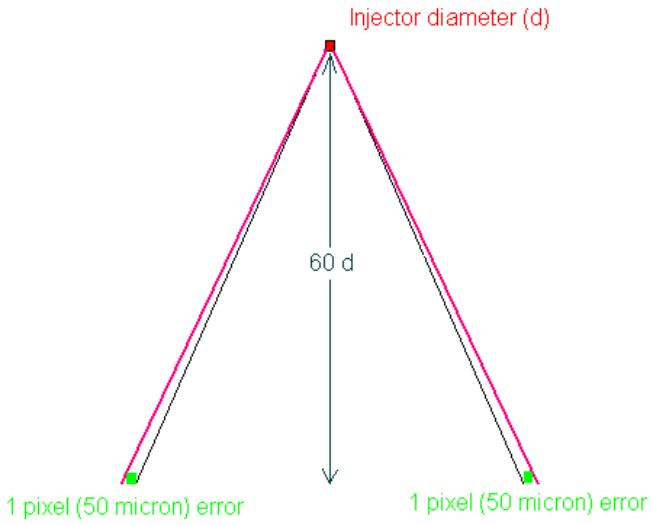

Figure 5.1 Error in measuring fuel spray angle and penetration

In this study, the Malvern Spraytec instrument was used for laser-diffraction measurement. For ventilation purpose, a vacuum system collects fuel after spraying. In order to show that this vacuum system has negligible effect on fuel spray development in the experiments, two different approaches were taken to investigate the influence of the vacuum system on measurement results. In the first approach, the ambient air velocity was measured at the entrance of the drain system. Since this velocity was too low to be measured by conventional pitot tube device, the air velocity

was measured at the horizontal section of the vacuum drain system as it is shown in Fig. 5.2, then by using incompressible flow assumption, the air flow velocity was calculated at the drain entrance as it is shown below:

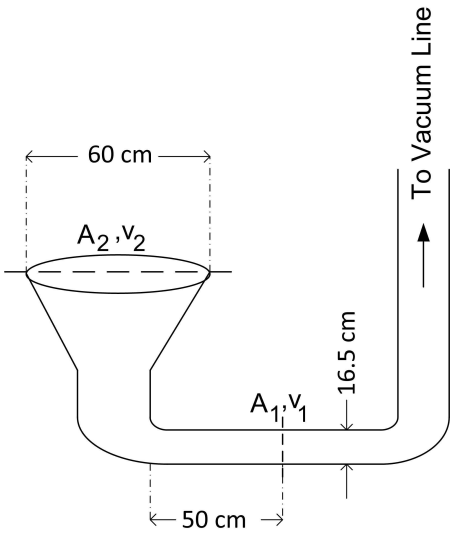

Figure 5.2 Flow velocity measurement in vacuum system

$$Q = A_1 v_1 = A_2 v_2 \;\rightarrow\; v_2 = \left(\frac{D_1}{D_2}\right)^2 v_1 = \left(\frac{16.5}{60}\right)^2 \times 3 = 0.23\,\frac{m}{s} \tag{5.2}$$

The calculated air flow velocity at the vacuum entrance is negligible compared to the fuel spray velocity which is order of 50 m/s. In the second approach, the droplet size distribution at a fixed injection pressure and temperature was measured for two cases: having the vacuum system on and off. Fig. 5.3 shows that the droplet size distribution is almost identical for both cases which indicates that the vacuum system has almost no effect on the experimental results.

In order to assess the accuracy and limitations of the Malvern instrument, it is necessary to simulate the dense spray environment with a two-phase medium of known particle number density and distribution. This was accomplished using a dispersion of Solid Soda Lime microspheres in distilled water in a stirred glass test cell. In order to make sure that using a glass container

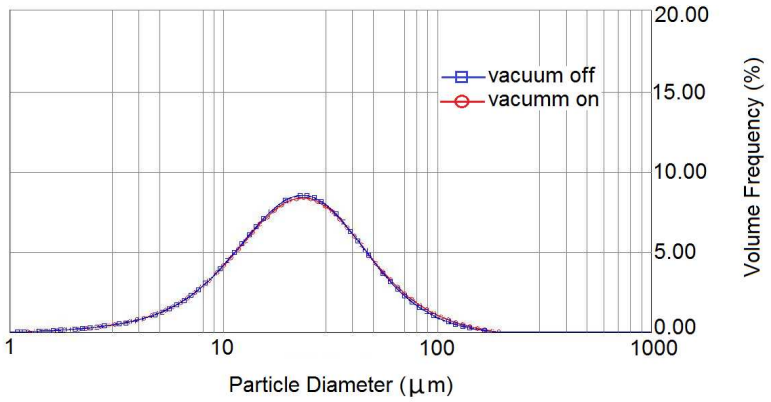

Figure 5.3 Effect of the vacuum system operation on measurement results (injection pressure and temperature are 5 MPa, 25 $^{\circ}$ C, respectively

does not affect the Malvern device measurement result, it is built from fine microscopic slides and it is placed such that the Malvern laser beam is perpendicular to the sides of the container. A test measurement of particle size distribution was also conducted to investigate the effect of this container on the performance of the Malvern device. In this test fuel spray, the size distribution for n-Heptane was measured with and without the container, as shown in Fig. 5.4. Fig. 5.4 shows the results of this test which demonstrates that the glass container has almost no effect on the Malvern device performance. The pulsed spray ran for 50 pulses and each pulse had the duration of 2 ms with the frequency of 40 Hz (Fig. 5.5). Based on the pulsed spray Weber number range in this experiment, no droplet splashing interfered with the Malvern measurement [72].

In order to calibrate the Malvern instrument, 1 gr of Solid Soda Lime glass made by Cospheric Inc. (which has microspheres in the range of 37-40 μm) was agitated in 200 ml distillate water in the glass container. Agitation was performed to prevent the particles from coagulating. The Malvern instrument indicated that 95.4 percent of particles were in the range of 34-40 μm, as shown in Fig. 5.6, which is the same as the certification for particles by Cospheric Inc.

It is also noteworthy that the Air Force Research Laboratory released a technical bulletin on calibrating the Malvern SprayTech device [4]. The goal of their study was to assess the capability and

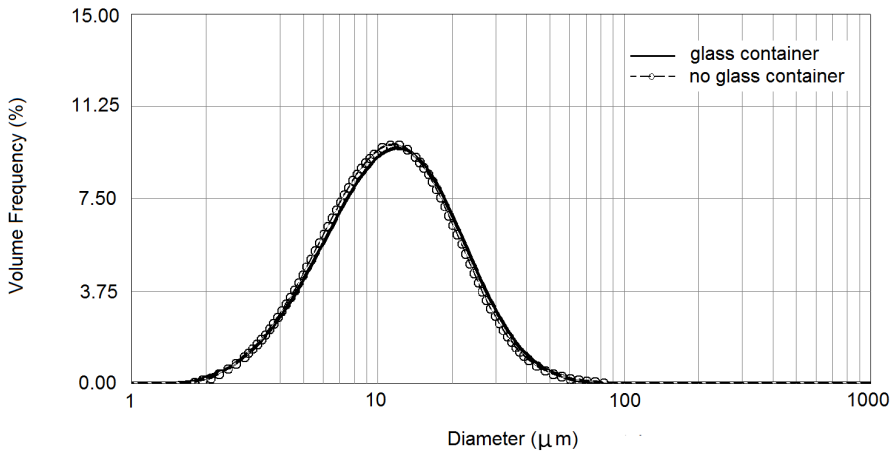

Figure 5.4 Effect of using a glass container in measuring droplet size distribution

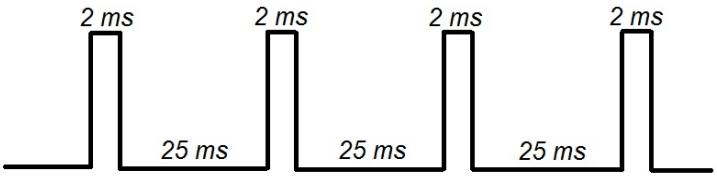

Figure 5.5 The pulsed spray duration which was used by the injector in all experiments

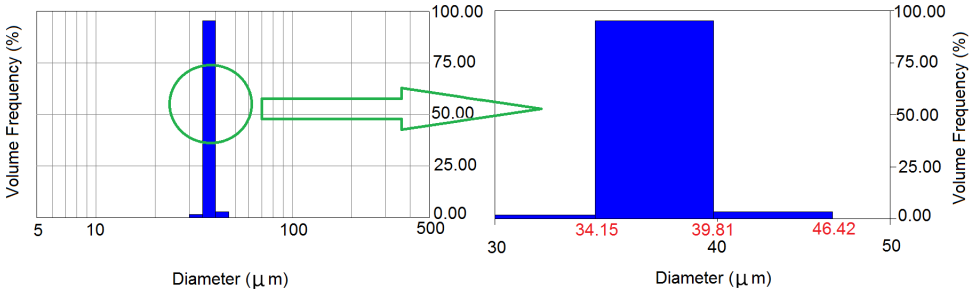

Figure 5.6 Calibration results of Malvern Spraytec with 37-40 μm microspheres

limitations of the laser diffraction technique in dense sprays. This involved a relatively broad range of sizes from tens of microns to nearly a millimeter in diameter. In order to assess the accuracy and limitations of the instrument, it was necessary to simulate the dense spray environment with a two-phase medium of known particle number density and distribution. This was accomplished using a dispersion of solid, spherical polystyrene microspheres and distilled water in a magnetically stirred glass test cell. Separate experiments were conducted with each instrument using both monodis-

persed microspheres at concentrations ranging from $1\ \%$ to 90% transmission and sizes ranging from 30 to $650\ \mu m$. Experiments were also conducted with polydispersed mixtures of beads over the same range of concentrations and sizes. The polydispersed mixtures consisted of six different bead sizes in relative concentrations that approximated log-normal size distributions typical of large-scale rocket injectors. Their results from the polydispersed experiments were presented as a percent error in the volume-weighted volume mean diameter from the actual size. Volume mean diameter was chosen as a representative indicator of accuracy distribution because the instrument uses a process of inverting the light scattering data to obtain a particle volume distribution and is thus geared toward providing maximum accuracy in a volume mean diameter. Fig. 5.7 contains plots of measurement error which they obtained, expressed as a percentage of volume mean diameter as a function of transmission for each of the polydispersed bead mixtures. The Malvern Spraytec instrument shows very high accuracy over the range of transmissions studied in this thesis. The instrument was accurate to within +/-10$\%$ in the transmission range of 2$\%$ to 90$\%$. The instrument produces reasonably good results even at a transmission of 1$\%$. However the minimum error occurred at above 60$\%$ transmission for all the distributions which is always the case in the experiment of this dissertation.

5.2 Droplet Size Distribution within a Pulsed n-Heptane Spray

During a single injection from a pulsed fuel injector, the lab data showed a variation of the droplet size distribution along the spray. The leading edge of the spray has larger droplets than the trailing edge as shown in Fig. 5.8, where the droplet size distribution is plotted at the spray leading edge, middle section, and trailing edge. These distributions were constructed from 50 ensembles of data, with each of the three distributions determined from 0.3 ms of data, with the entire passage of the

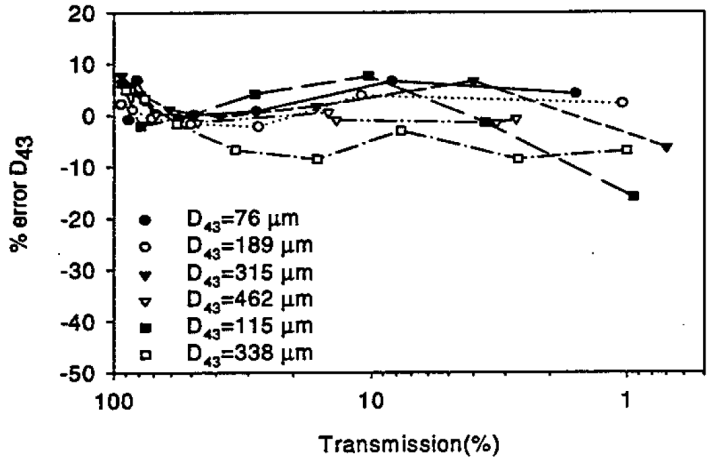

Figure 5.7 Percent error in measured volume mean diameter verses transmission for SprayTech [4]

spray through the measuring volume taking 2 ms. The corresponding values of D_{43} and $Dv50$ in these parts of the spray, measured at 50 mm from the injector nozzle, were 27.73 μm, 23.1 μm, 19.93 μm and 23.16 μm, 18.43 μm, 15.35 μm, respectively. For a single spray injection, the minimum spray droplet mean diameter occurs near the spray tail. In this study, all subsequent droplet size distributions plotted are averaged over the entire length of the spray and representative of the size distribution in the center of the spray.

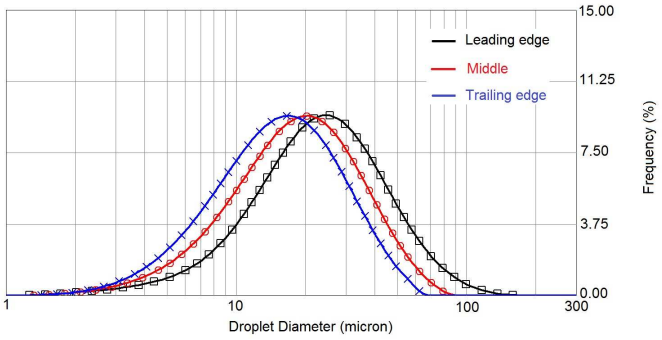

Figure 5.8 Droplet size distribution variation along a n-Heptane single spray injection

5.3 The Geometry of a Low Pressure n-Heptane Spray at Ambient Fuel Temperature

Experiments have been carried out using the methodology described in the previous chapter for n-Heptane pulsed injection into an ambient atmosphere conditions at 20°C, 1 bar at fuel supply pressures between 5 and 10 MPa. A typical image of the resulting spray, 0.3 ms after injection, is shown in Fig. 5.9. It can be seen that the spray for a single hole injector is a symmetric cone shape with a spray angle of approximately 15°. The spray appears to be less dense at its edges and front, possibly because the proximity to the ambient air enhances evaporation. In Fig. 5.10,

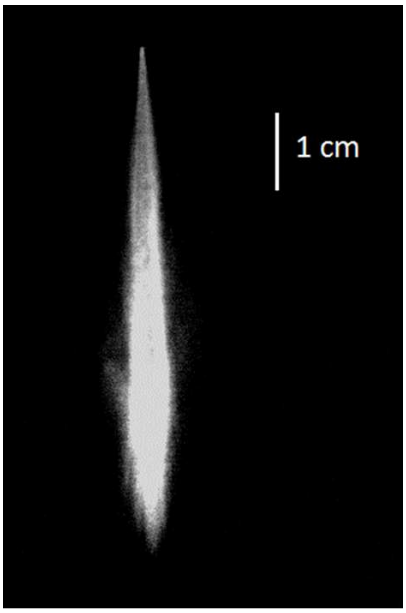

Figure 5.9 n-Heptane spray overall shape

the development of an n-heptane spray injected at an upstream pressure of 10 MPa is shown. The development of the break-up core can be seen in this sequence of images. The front edge of the spray gets sharper as it moves and it can be seen that the break-up starts almost from the center of the spray. The spray is less dense at its sides and the droplets are finer in this area than the center. Because of the stochastic nature of sprays, several experiments were performed

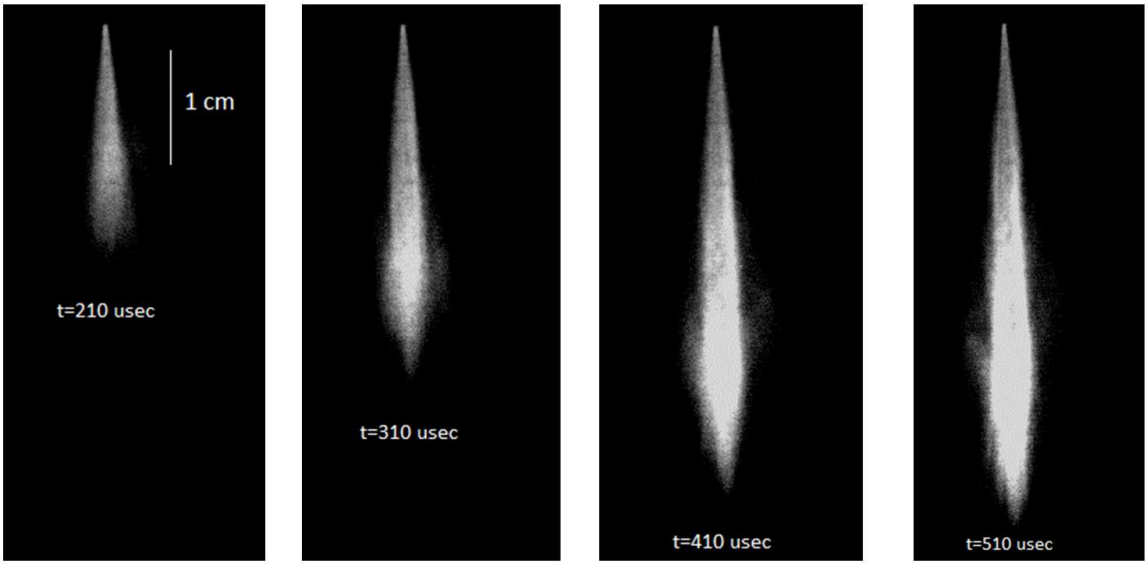

Figure 5.10 Development of n-heptane spray at 10 MPa, 25$^{\circ}C$

to determine how the spray cone angle and penetration would change under different injection conditions. For this purpose, the variance is defined as the average of the squares of the differences between the individual experimental values and their averaged value. Standard deviation is defined as the square root of the variance and is used to express how measurements for a group are spread out from the average. Fig. 5.11 shows the behavior of the cone angle value at an injection time of 2 ms at two different injection pressures, for 50 independent experiments at the same conditions. As the injection pressure doubled from 5 MPa to 10 MPa, the spray angle decreased by about 3 degrees. The vertical lines show the numbers between the minimum and maximum measured values during the experiments. Because of the stochastic nature of the secondary breakup [73], the spray edges vary with time. From Fig. 5.11, it can be inferred that the spray angle varied during the injection [1] and this is thought to be due to the unsteady nature of the spray formation. The measurement error of cone angle in the experimental series is less than 0.3 degrees, so the variations seen in Fig. 5.11 and Fig. 5.13 are not noise.

Fig. 5.12 shows the averaged value of the spray tip penetration of 50 observations at the same

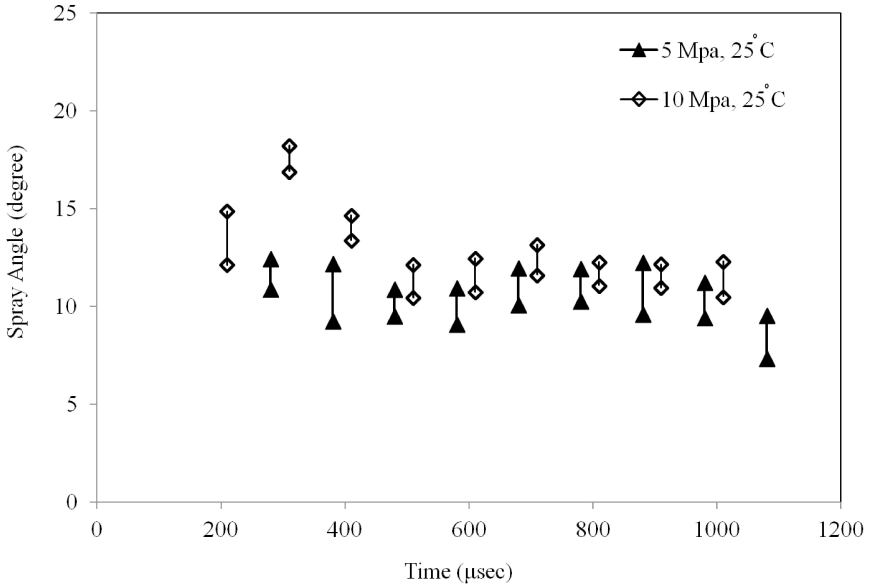

Figure 5.11 Dependence of spray angle on time and injection pressure at a fuel temperature of 25°C in a 25°C ambient.

conditions, for two different injection pressures. As the injection pressure increased, the spray liquid-jet Reynolds and Weber numbers increased, and the tip of the spray developed faster.

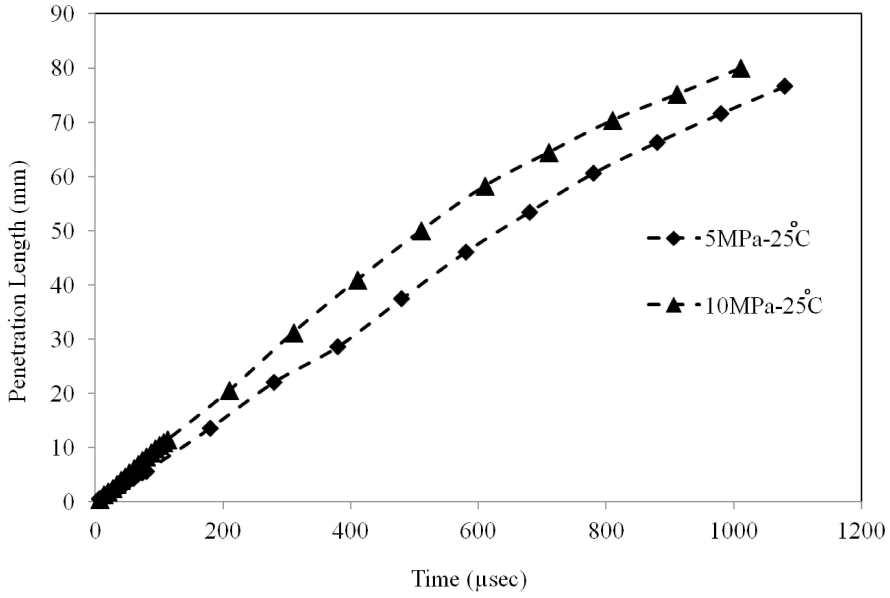

Figure 5.12 Effect of injection pressure on the spray tip penetration at a fuel temperature of 25°C in a 25°C ambient.

5.4 The Effect of Fuel Temperature on the Geometry of a Low Pressure n-Heptane Spray

Fig. 5.13 shows the behavior of the cone angle at an injection time of 2 ms for different n-heptane temperatures, for 50 independent experiments performed at the same conditions. At the higher fuel temperature (by $50^{\circ}C$), the spray angle decreased by several degrees. The vertical lines show the values between the minimum and maximum measured values during the experiments. From this figure, it was inferred that the spray angle varied during the injection and was again due to the unsteady nature of the pulsed spray. Fig. 5.14 shows the averaged values of the spray tip penetration

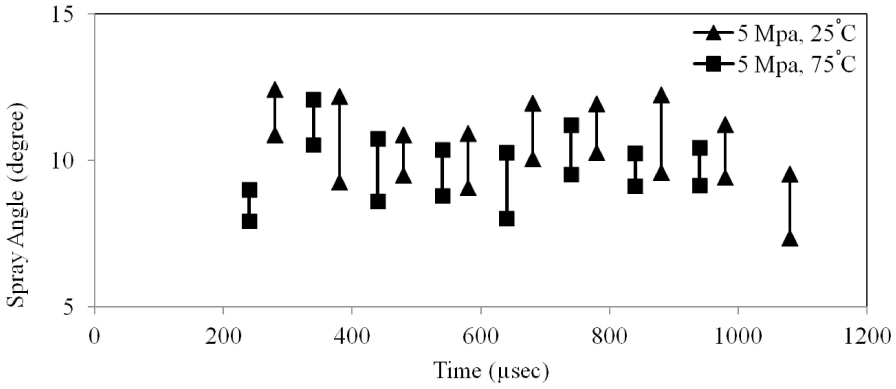

Figure 5.13 Dependence of spray angle on time and on fuel temperature

of 50 observations, at the same conditions, but for two fuel temperatures that differed by 50°C. At the higher fuel temperature, evaporation was thought to be a more important phenomenon and so the increased rate of droplet evaporation made the front of the spray develop more slowly.

5.5 The Microscopic Characteristics of an n-Heptane Spray

In this section, data obtained from laser diffraction measurements of droplet diameters in a pulsed spray, using the techniques described in the previous chapter, are presented. The sizes of droplets

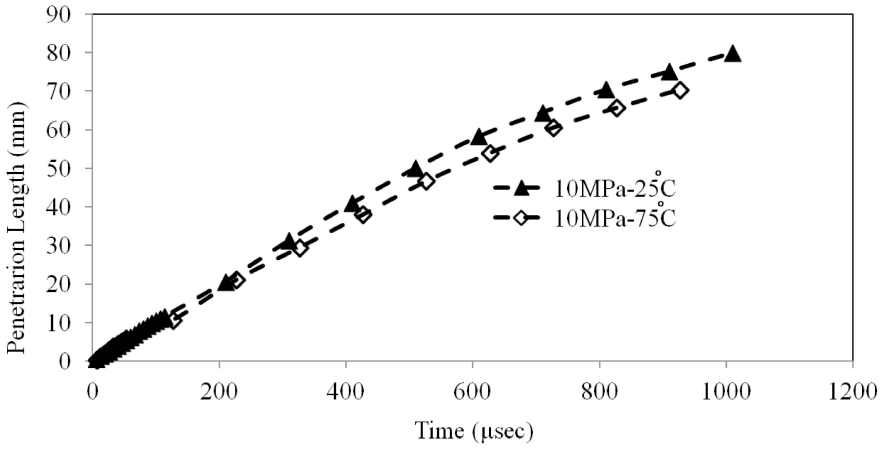

Figure 5.14 Effect of fuel temperature on spray tip penetration

in the spray are described by a log-normal distribution, as shown in Fig. 5.15. In this figure, the logarithmic abscissas represent both the volume frequency and cumulative volume percentages for droplets which have the same range of diameters. These distributions are the time averages of 50 experimental distributions measured under nominally identical experimental conditions.

In Table 5.1, stochastic parameters of the data presented in Fig. 5.15 are shown, with Dv50 and Dv90 as the droplet diameters at which 50 and 90 percent of the volume of spray droplets is smaller and the rest is larger. Dv50 value is also known as the Mass Median Diameter (MMD), and indicates the mid range of the distribution. The term 'Trans' is a measure of the amount of (transmitted) laser light reaching the beam power detector. Some light is blocked when droplets pass through the measurement area. When the transmitted light is more than about 80%, there are too few droplets in the area of measurement; when it is less than about 20%, the spray in the region of interrogation is too dense. In either of these cases, diffraction measurements may not be trustworthy.

The Malvern instrument has the ability to measure the droplet size distribution in time intervals as short as 0.4 ms. Fig. 5.16 shows the variation of different droplet size mean values during a single injection. In this figure, the solid black line represents the variation of received laser

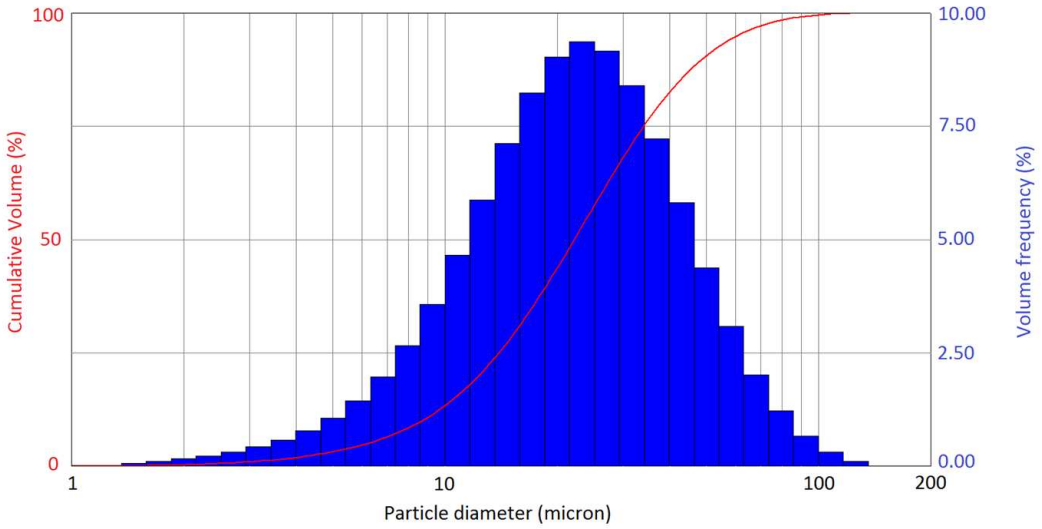

Figure 5.15 A typical size distribution of droplets in the far field of an n-heptane spray at an injection pressure of 5 MPa and a fuel and environment temperature of 25°C

Table 5.1 Stochastic values of Fig. 5.15 distribution

property	average	standard deviation	min	max
Trans(%)	63.3	9.3	54	87
Dv50 (μm)	22.17	1.463	21.06	26.42
Dv90 (μm)	49.1	2.06	48.16	55.46
SMD (μm)	16.15	1.019	15.45	19.24

intensity. It is clear that as the spray develops the transmission percentage reduces, showing that the middle of a single spray is denser. After the dense region of the spray and near the tail of the spray the transmission percentage increases. From different averaged droplet diameters, it is clear that the front leading edge of the spray consists of larger droplets compared to the middle and tail of the spray. Based on Fig. 5.16, during a single injection, the spray front leading edge Sauter Mean Diameter (SMD) is $26\ \%$ more than the minimum SMD; happening near the spray tail. This relative percentage is 35 and 45 for Dv50 and d_{43}, respectively. In this study in order to investigate the spray characteristics, a time averaged data of several measurements were used.

Fig. 5.18 and 5.17 show the effect of the injection pressure on droplets size distribution at a distance of 19 mm from the injector tip—the closest location at which reliable measurement

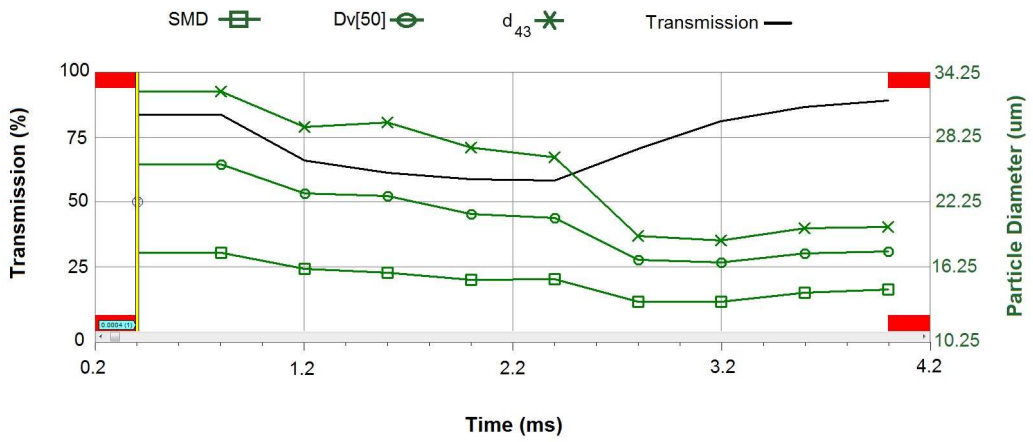

Figure 5.16 Variation of droplet size mean values during a single injection

could be made. Each graph is the time average of 50 experimental measurements at the ambient temperature of 25°C and is measured at 19 mm and 25 mm below the injector tip respectively. From these figures, it appears that increasing the injection pressure moves the distribution to the left in Fig. 5.15, implying there are more smaller droplets. From Fig. 5.18, at an injection pressure of 5 MPa, approximately 99% of droplets have diameters less than 160 μm, while at 10 MPa, this measure of diameter drops to 100 μm. Thus the droplet size distribution is very sensitive to the injection pressure. Table 5.2 shows the SMD and Dv50 values and their standard deviations for these experiments.

Table 5.2 Mean droplet sizes of Fig. 5.17

Injection Pressure	Mean Size	Average	Standard Deviation
5.0 MPa	Dv50 (μm)	23.16	2.173
	SMD (μm)	16.87	1.465
5.0 MPa	Dv50 (μm)	23.16	2.173
	SMD (μm)	16.87	1.465
5.0 MPa	Dv50 (μm)	23.16	2.173
	SMD (μm)	16.87	1.465

Fig. 5.19 shows the size distribution of droplets at different axial locations when the ambient and fuel temperature are 25°C. These measurements were made downstream of the location at which the primary and secondary break-up take place. From this figure, it can be seen that the size

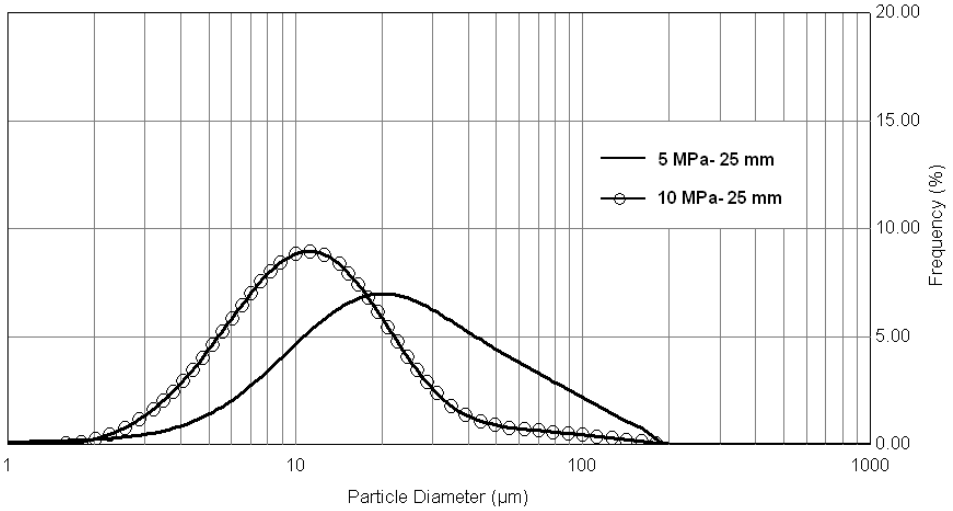

Figure 5.17 Effect of injection pressure on spray droplets size distribution

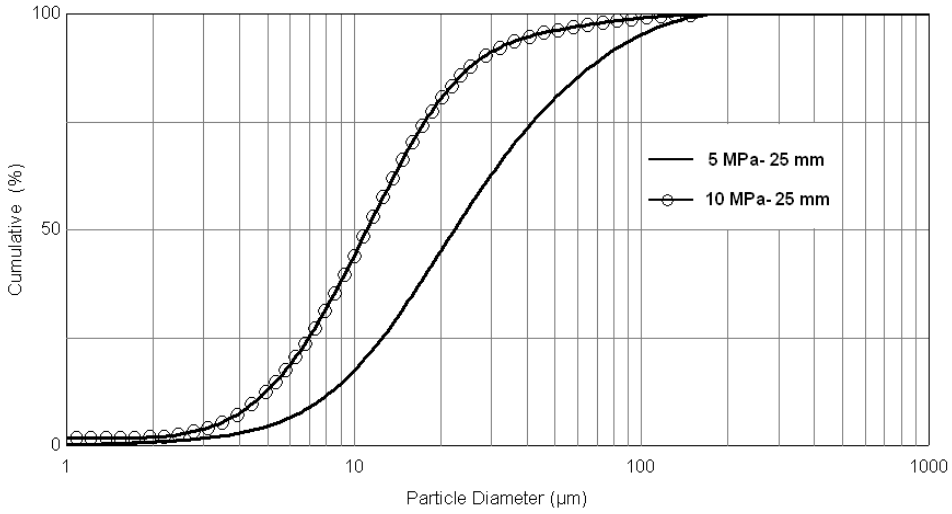

Figure 5.18 Effect of injection pressure on cumulative spray droplet size curve

distribution is shifted towards a larger ensemble of droplet diameters with increasing downstream distance. This observation is important because it suggests that there is a greater proportion of larger droplets in the spray as axial distance increases. This shift to larger droplets in the distribution could be caused either by the removal of small droplets through evaporation, or by droplet collision yielding more larger droplets.

Fig. 5.20 shows the variation of SMD with axial distance from the injector tip. This figure

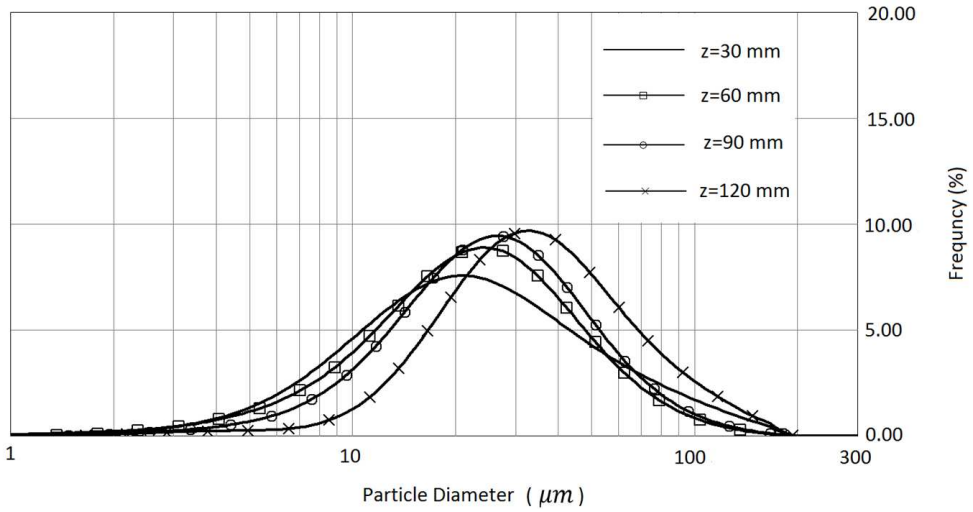

Figure 5.19 Droplet size distribution at different axial locations, at an injector pressure of 5 MPa and fuel temperature of 25°C (here z is the axial distance from the injector tip)

shows unambiguously that the average droplet diameter grows with axial distance and that the shift in the droplet distribution to larger diameters is not an artifact of the removal of small droplets from the distribution. Therefore droplet collision, which can yield larger diameter droplets, appears to be an important mechanism during spray development. It is also possible that droplet coalescence takes place as a result of collisions, leading to an increase in the SMD of droplets with axial distance.

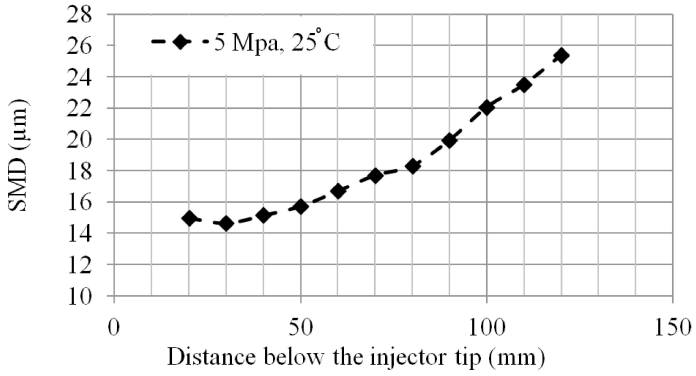

Figure 5.20 Axial SMD variation for the injection conditions of Fig. 5.19

Fig. 5.21 shows the SMD of droplets at different -on and off -axial locations, at ambient and fuel temperatures of 25°C. From this figure, it appears that droplets are finer at the edges of sprays,

where evaporation is more prevalent and there are fewer opportunities for collisions.

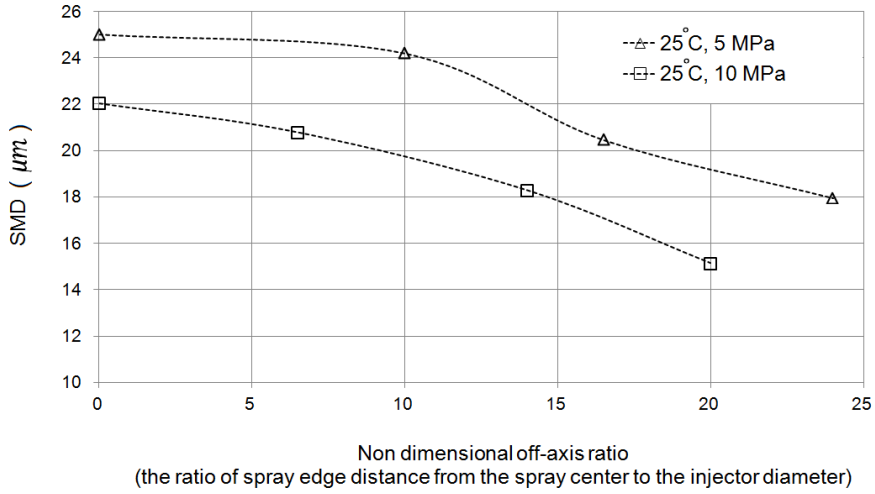

Figure 5.21 The variation of droplets SMD for different off-axial locations at ambient fuel temperature at 25°C

5.6 The Effect of Fuel Temperature on the Microscopic Characteristics of an n-Heptane Spray

Figs. 5.22 and 5.23 show the effect of the fuel temperature on the droplet size distribution in an impulsively started n-heptane spray. Each graph shows the time averaged of 50 experimental measurements at an injection pressure of 5 MPa and an axial location of 100 mm from the injector tip. From these figures, it is clear that increasing the fuel temperature from 25 to 75°C shifts the size distribution function to the right, which corresponds to fewer smaller droplets and a greater proportion of larger droplets. This effect is thought to be due to evaporation, which is more pronounced at higher fuel temperatures and depletes the spray of its smallest droplets. Table 5.3 shows the SMD, Dv50 and standard deviations for the data in these graphs.

Fig. 5.24 shows droplet size distributions at different axial locations in a n-heptane spray at

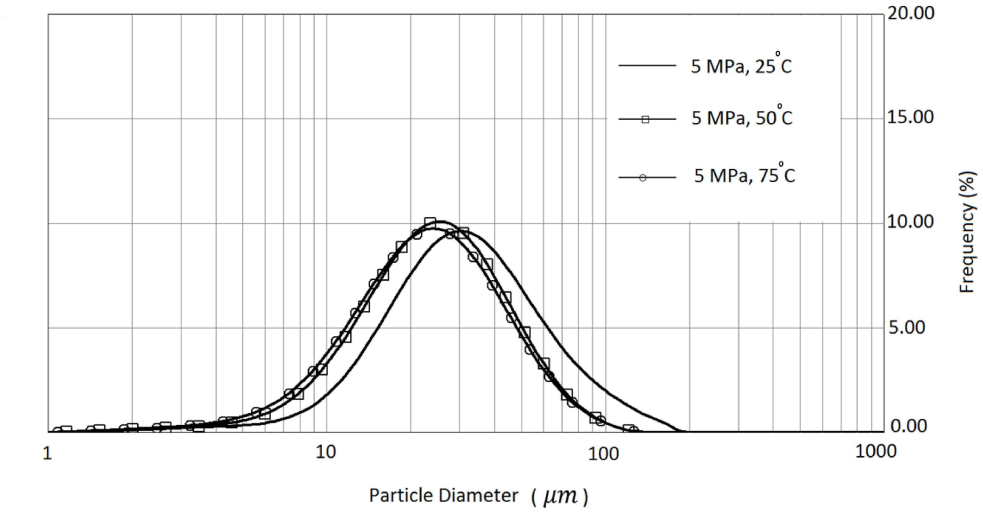

Figure 5.22 Effect of fuel temperature on the spray droplet size distribution

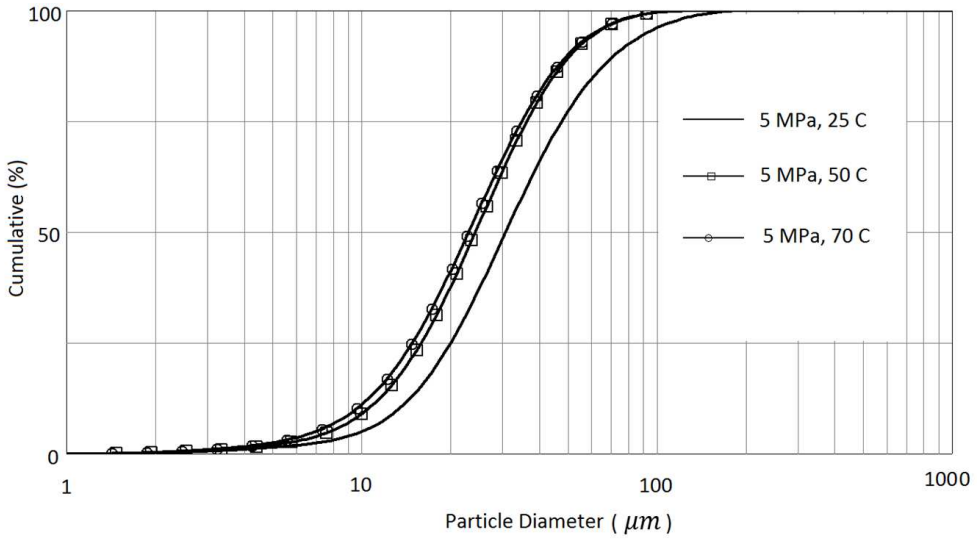

Figure 5.23 Effect of fuel temperature on the spray droplet size cumulative distribution curve

Table 5.3 Spray mean droplet sizes of Fig. 5.22

Fuel Temperature	Mean Diameter	Average	Standard Deviation
25°	Dv50 (μm)	30.65	3.633
	SMD (μm)	23.04	2.982
50°	Dv50 (μm)	24.22	3.25
	SMD (μm)	18.17	2.373
70°	Dv50 (μm)	22.97	0.963
	SMD (μm)	16.9	0.556

a fuel-line temperature of 75°C- a temperature at which droplet evaporation was shown to be significant in Fig. 5.22. However, from this graph, it can be seen that, even when evaporation is significant, the effect of increasing axial position is still to shift the droplet size distribution curve to the right, indicating a greater proportion of larger droplets with increasing downstream distance. The most likely explanation for this effect is that droplet coalescence through collision plays a dominant role in the downstream evolution of a spray. This effect will be examined through simulations in the following chapter.

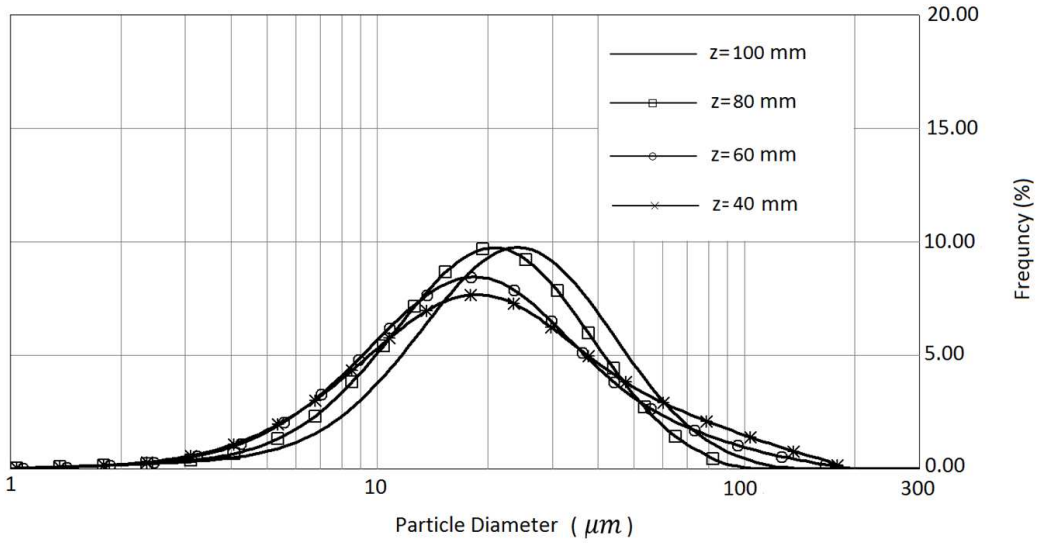

Figure 5.24 Droplet size distribution at different axial locations, at an injection pressure of 5 MPa and a fuel temperature of 75°C, where z is the axial distance from the injector tip.

Fig. 5.25 represents the SMD of droplets for different -on and off -axial locations for fuel temperature at 25, 75°C. For elevated fuel temperatures, the droplets are still finer at the edges of the spray.

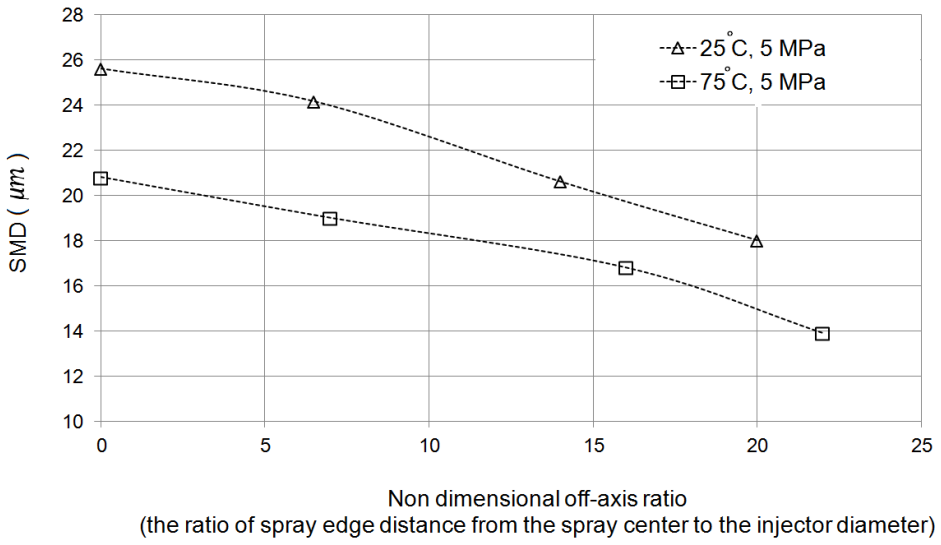

Figure 5.25 The variation of droplets SMD for different off-axial locations at different fuel temperatures at 5 MPa injection pressure

Chapter 6

Fuel Spray Modeling

In this chapter a simplified numerical approach to modeling the far field of low-speed sprays is presented.

6.1 Introduction

Although several break-up models have been proposed recently to estimate initial droplet size distribution in spray modeling, none of them can predict the generated fuel droplet size distribution with a high level of accuracy. The ability to measure droplets size with a Malvern Spraytec laser diffraction device provides a unique opportunity to use experimental measurements as initial conditions in simulations.

Simulation of the detailed evolution of low/medium pressure fuel sprays requires numerical solution of the velocity, temperature and concentration fields in the gas phase surrounding the droplets, and coupled solutions of the motion of individual droplets, possibly including their internal liquid motion and surface phase change ([74], [75]) and is computationally very expensive. Simulation of the break-up of liquid streams into droplets can have even greater computational expense. It is therefore important and useful to explore simplified and computationally cheaper approaches to modeling the evolution of sprays. Since trustworthy measurements of the size distribution of droplets at different downstream locations in a fuel spray can be made, the adequacy of

simplified modeling approaches for the far field of a fuel spray can be explored by using measured droplet size distributions near the injector nozzle as initial conditions and measured far field size distributions as target data for evaluation of spray model performance. In this thesis, the simplified modeling approach explored is one in which a large number of spherical droplets, of a chosen size distribution and initial velocity field, each move in a Lagrangian frame, governed by Newton's second law of motion. A simple evaporation model is used to describe phase change, and several models for droplet collisions- which are believed to be the main cause of changes in size distribution in the experiments of this study- are explored. A simple spherical droplet drag force model is used, and in this way the behavior of droplets in sprays is modeled without the considerable expense of having to solve for the companion gas phase, the internal velocity within each droplet, or the non-sphericity of droplets. The adequacy of this simplified modeling approach for low-pressure fuel sprays is the assessed by comparing predicted with measured droplet size distributions. The numerical simulation used in this study was programmed using MATLAB. Ensembles of droplets with random diameters which have the same size distribution as the ones measured from the Malvern Spraytec instrument can be generated relatively easily by computer. Using these generated droplets to match the initial size distribution in the fuel spray and implementing evaporation and collision models to simulate the Lagrangian development of droplets result is the essence of this fuel spray model. Since the Malvern Spraytec device has the ability to measure the droplet size distribution at different locations (Fig. 6.1), the fidelity of simulation results can be tested by comparing them with measured data at downstream locations.

There are important assumptions that are used in the simulation:

i) The droplets are assumed spherical and the environmental air drag force is the only force participated in the equations.

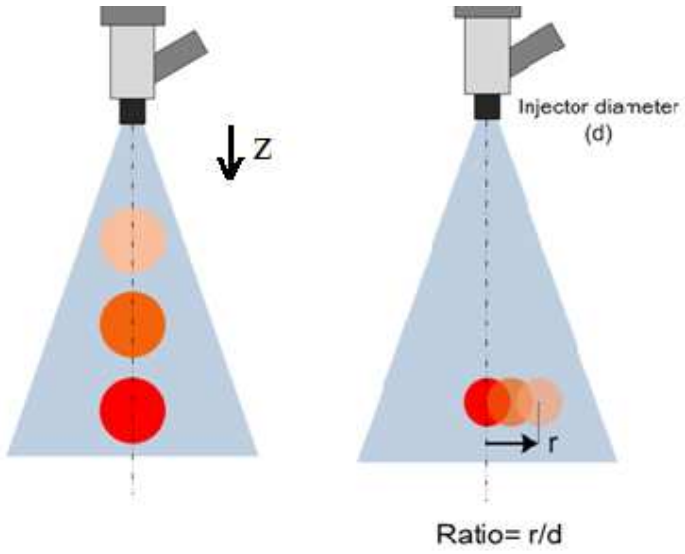

Figure 6.1 Schematic of the ability of the Spraytec instrument to measure size distributions at different locations

ii) The environmental gas phase is stagnant during the spraying event and the gas phase entrainment is assumed to be negligible.

iii) No turbulent equation is solved during the spraying event.

6.2 Test Calculations and Results

6.2.1 Simulation Procedure

In order to test the Lagrangian spray model and its dependence on the choice of collision model, the following steps are taken:

1. Droplet size distribution is measured experimentally at a desired location far enough (more than 30 mm) from the injector tip that the Malvern device is supposed to measure trustworthy data. The size distribution at this location is the initial condition in spray modeling. Additional measurements are also performed of fuel droplet size distribution at locations

beyond the first one.

2. Spherical droplets are generated by computer with random diameters which have the same size distribution as measured in experiments. These droplets and their diameters are considered as the initial conditions in the numerical simulation.

3. Velocities of droplets are determined from the experimental conditions.

4. Linear momentum equations are solved for the initial ensembles of droplets in a control volume around the spray to obtain the velocity field of all droplets at the next time step. When two droplets occupy parts of the same volume, they are considered to have collided. The appropriate collision model is then implemented to determine the outcome, and this procedure is continued at subsequent time steps.

6.2.2 Effect of Number of Droplets on the Convergence of Size-Distribution Statistics

As shown in the experimental results chapter, droplet size distribution in a pulsed fuel spray has a log-normal shape. In order to having a realistic numerical simulation, it is essential to generate initial droplets with random diameters which have a log-normal size distribution. The proper way of generating random droplets should not only be independent of the number of droplets, but also has the same range of fuel concentration in the air-fuel mixture as in the experiments. Fig. 6.2 shows the influence of the number of generated droplets on size distribution for specific mean and standard deviation values.

According to following definitions, the fuel spray Reynolds and Weber number in this case are

$52,000$ and $102,000$, respectively.

$$Re = \frac{\rho v d}{\mu}, We = \frac{\rho v^2 d}{\sigma} \tag{6.1}$$

where ρ is fuel density, d is injector orifice diameter, σ is fuel surface tension and v is fuel spray average velocity. Bosch injector model PA66 with a single hole diameter of 0.3 μm and spray wide angle of 12 degrees was used to generate droplets with the mean diameter value of 35 μm.

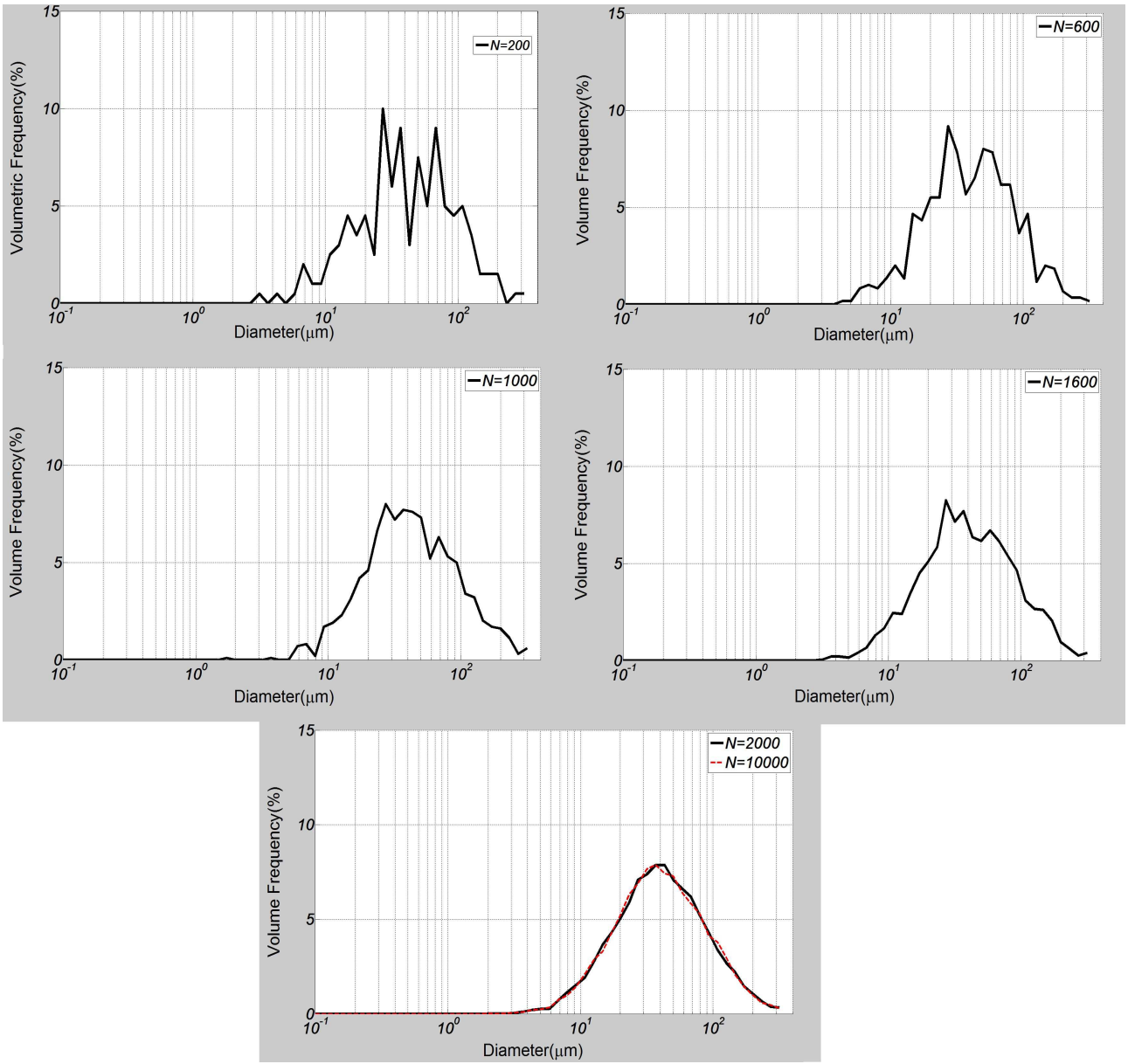

Figure 6.2 Generated random droplet size distribution for different number of droplets

According to Fig. 6.2 increasing the number of generated droplets from 2000 to 10,000 has negligible influence on the size distribution however it increases the calculation cost significantly. Taking into account that in the experiments n-heptane concentrations were measured in the range of 10 ppm to 30 ppm, choosing 2000 initial droplets results in a fuel concentration compatible to the experimental measurements as described below. In this study simulations, since the Malvern Spraytec laser beam diameter is 16 mm, the control volume dimensions are chosen to be 10 mm x 10 mm x 16 mm. Assuming the average diameter of droplets to be 30 μm, fuel droplets concentration is calculated as follows:

$$V_{control\ volume} = 10 \times 10 \times 16\, mm^3 = 16 \times 10^{-7} m^3 \tag{6.2}$$

$$d_{mean} = 30\ \mu m \tag{6.3}$$

$$V_{droplets} = 2000 \times \frac{\pi}{6} \times (30 \times 10^{-6})^3 = 28.27 \times 10^{-15} m^3 \tag{6.4}$$

$$\frac{V_{control\ volume}}{V_{droplets}} = 56.6 \times 10^6 = 56.6\ Million \tag{6.5}$$

$$PPM = \frac{2000}{56.6} = 35.3 \tag{6.6}$$

It is deduced that using 2000 droplets as the initial number of droplets in this study simulations not only results in having an independent smooth distribution, but also makes the air-fuel mixture concentration in the right range.

6.2.3 Effect of Mean Value of Initial Velocities on Downstream Statistics

The average value of initial velocity of droplets at injector tip is 100 m/s. It is assumed that the spray is symmetric and that each droplet has an initial velocity vector in the direction from the center of the injector tip to the center of the droplet, shown in Fig. 6.3. To investigate the effect of the initial mean velocity of droplets on downstream statistics, the downstream size distribution is calculated for different initial mean velocities for a representative initial log-normal size distribution. All droplet velocities are assumed to have an initial velocity equal to the mean velocity, and the O'Rourke model is used for predicting the collision outcomes. This simulation is carried out at ambient temperature for n-Heptane droplets, for which evaporation is assumed to be negligible at room temperature. Based on the definition given in Eq. 6.1 and the size distribution chosen, the Weber number range was between 0.5 and 86.7. The Reynolds number is in the range of 600 to 6,400.

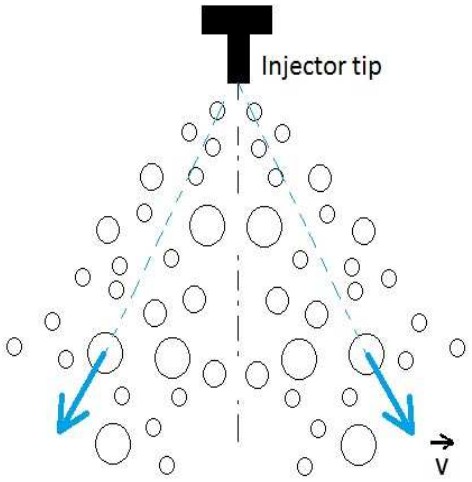

Figure 6.3 Droplets initial velocity

Fig. 6.4 shows that higher initial velocities result in slightly larger droplets downstream, which can be explained by the fact that increasing the initial droplet velocity increases the Weber number which results in more coalescence through head-on collisions, making the size distribution move slightly to the right. However this effect becomes much less significant when the initial mean velocity is reduced to 80 m/s or 40 m/s.

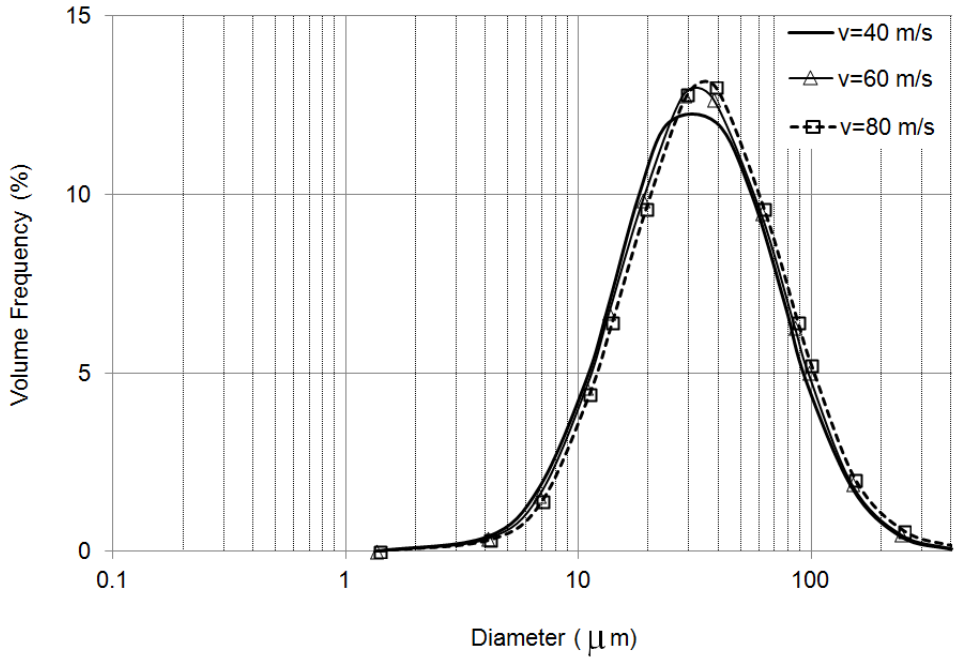

Figure 6.4 Simulated droplet size distribution at 50 mm downstream for different initial mean velocities

6.2.4 Effect of Synthetic Turbulence in Initial Velocity on Downstream Statistics

In this section, the effect of adding fluctuations to initial velocities of a few percent on downstream droplet size distribution is investigated. A random number between -1, 1 (RAN) is created for each droplet, so the instantaneous initial droplet velocity can be modeled as:

$$\frac{v}{V} = 1 + \alpha * (RAN), \tag{6.7}$$

The direction of each droplet velocity is assumed to be the same as described in the previous section. Fig. 6.5 shows the effect of upstream velocity fluctuations on downstream droplet size distribution for two different α values of 0.05 and 0.1. It is clear that this effect is very small in this study. The following statistical equations are used to calculate fluctuation intensity for different initial velocities.

$$u_{p,i} = \bar{u}_{p,i} + u'_{p,i} \ , \ \ p \in \{x, y, z\} \tag{6.8}$$

$$\bar{U}p = \frac{1}{N} \sum_{i=1}^{N} \bar{u}_{p,\,i} \ , \quad p \in \{x, y, z\} \tag{6.9}$$

$$U'p = \frac{1}{N} \sum_{i=1}^{N} u'_{p,\,i} \ , \quad p \in \{x, y, z\} \tag{6.10}$$

$$\bar{U} = \sqrt{\bar{U}_x^2 + \bar{U}_y^2 + \bar{U}_z^2} \tag{6.11}$$

$$U' = \sqrt{\frac{1}{3}\left(U'^2_x + U'^2_y + U'^2_z\right)} \tag{6.12}$$

$$I = \frac{U'}{\bar{U}} \tag{6.13}$$

Based on the above equations, the fluctuation intensity (I) is 2.3 and 5.6 percent for α values of 0.05 and 0.1, respectively.

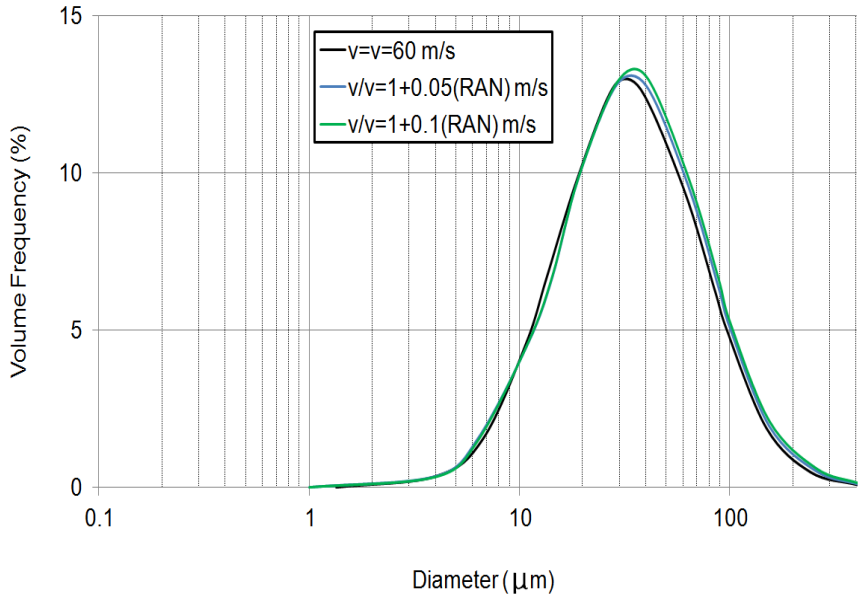

Figure 6.5 Simulated droplet size distribution at 50 mm downstream for synthetic turbulences in initial velocities

6.2.5 Droplet Collision

In this study four collision outcomes are considered as possible results of a binary collision as it was shown in Chapter 3. In this study in case of collision between two droplets, the value of the impact parameter is obtained analytically based on what it was proposed by Taskiran [76], which makes the collision model described in the previous chapter more accurate. In other previous simulation works, the impact parameter is chosen as a positive random number less than one, however this assumption can influence the result of collision simulation significantly, especially where there are many head-on collisions.

6.2.5.1 Binary Collision Impact Parameter

Consider two spherical droplets (Fig. 6.6) which have diameters of d_1, d_2 (d_1<d_2), and their position vectors at time t are $P_1(t)$ and $P_2(t)$, respectively. If $X_1(t)$, $X_2(t)$ demonstrate the position of droplets before collision, and $X_1(t_c)$, $X_2(t_c)$ represent the positions at the instant of collision (t_c), it is obvious that

$$|X_1(t_c) - X_2(t_c)| = \frac{1}{2}(d_1 + d_2) \tag{6.14}$$

$$X_1(t_c) = P_1(t) + U_1(t_c - t) \tag{6.15}$$

$$X_2(t_c) = P_2(t) + U_2(t_c - t) \tag{6.16}$$

$$|P_1(t) + U_1(t_c - t) - P_2(t) - U_2(t_c - t)| = \frac{1}{2}(d_1 + d_2) \tag{6.17}$$

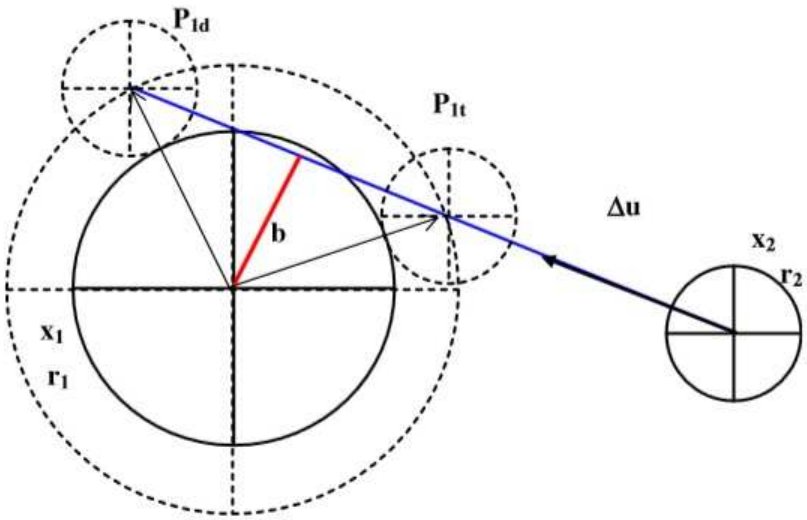

Figure 6.6 Representation of a binary impact parameter

$$\left| \left(P_1 \left(t \right) - P_2 \left(t \right) \right) + \left(t_c - t \right) \left(U_1 - U_2 \right) \right| = \frac{1}{2} (d_1 + d_2) \tag{6.18}$$

by introducing the following parameters

$$\Delta P = P_2 \left(t \right) - P_1 \left(t \right) \tag{6.19}$$

$$\Delta U = U_2 - U_1 \tag{6.20}$$

$$\Delta t = t_c - t \tag{6.21}$$

and substituting in Eq. 6.18, one can say

$$\left| \Delta P \right|^2 + 2 \left| \Delta P \right| \left(\Delta t \right) \left| \Delta U \right| + \left| \Delta P \right|^2 (\Delta t)^2 = \frac{1}{4} \sigma^2 \tag{6.22}$$

The smaller positive root of Eq. 6.22 gives the collision time t_c and the other positive root represents the imaginary departure time t_d. According to Fig.6.6 the imaginary distance traveled by the smaller droplets between t_c and t_d can be shown as $\Delta U(t_d - t_c)$. From the definition, impact parameter can be obtained by

$$b = \frac{2B}{d_1 + d_2} = \frac{2B}{\sigma} = \frac{2\sqrt{\sigma^2 - \frac{\left[|\Delta U|(t_d - t_c)\right]^2}{4}}}{\sigma} \tag{6.23}$$

Eq. 6.23 gives the impact parameter in a binary collision which depends on physical properties of both droplets. This impact parameter is incorporated into the Ko model, and called the extended Ko model.

6.2.6 Collision Models Comparison

In this section, results of implementing different collision models in the Lagrangian tracking of droplets are introduced. This gives the opportunity to compare the collision model results to better understanding the phenomenon of each one. In order to minimize the effect of evaporation of droplets in a fuel spray, simulations were done at 25 $^{\circ}C$ room temperature. Also, since the velocity of fuel spray at the injector exit is in the order of $100\ m/s$, entrainment of the surrounding air is expected to be negligible. The same droplet size distribution as what was measured by Spraytech at $30\ mm$ downstream was assumed as the initial condition in implementing different collision models. In that case the simulation is almost a pure collision problem in a pulsed fuel spray. Three following collision models are implemented into droplets development:

1. O'Rourke

2. Ko

3. Ko extended using the analytical Taskiran impact parameter model

Fig. 6.7 shows the droplet size distribution from lab data at 4 different axial locations downstream the fuel spray. The lab data at $30\ mm$ below the injector tip was used as the initial distribution in the simulations. The droplets get larger due to collision as they develop in these series of experiments.

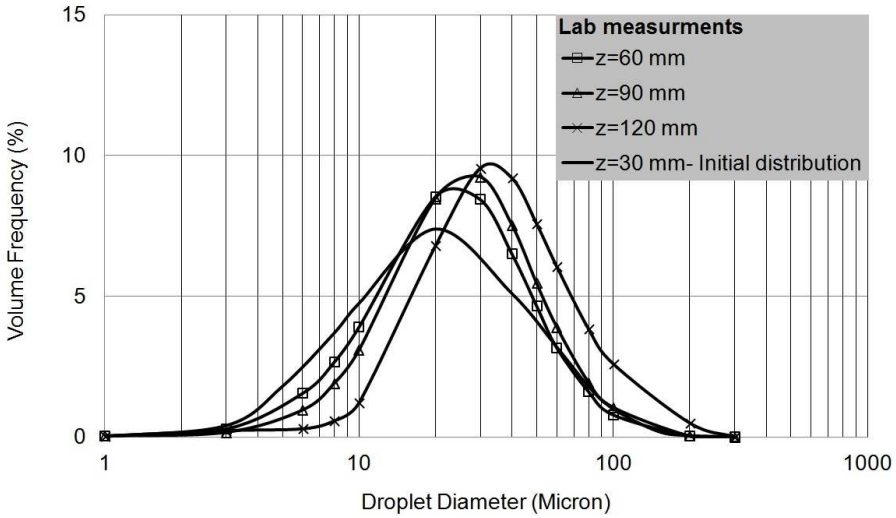

Figure 6.7 Droplet size distribution for n-heptane spray collected by Malvern Spraytec at $25°C$ room temperature and $5\ MPa$ injection pressure

For each simulation, 2000 droplets were tracked. They each had an initial velocity of $60\ m/s$, a vector direction outward from the nozzle center, the density, surface tension and viscosity of n-heptane, and a size distribution chosen to match the experiment.

6.2.6.1 Simulation Results using the O'Rourke Model

Fig. 6.8 shows the droplet size distribution that resulted from the simulation using the O'Rourke model for describing the collision outcomes. Following the spray development downstream, it is seen that droplets become larger on account of collisions. The O'Rourke model predicts that the average diameter of droplets gets 4 times larger in a development distance of 90 mm. Compared

to the experimental data of Fig. 6.7, this average size increase is unrealistically larger and implies that the assumptions of the O'Rourke module are not well-suited to the real spray.

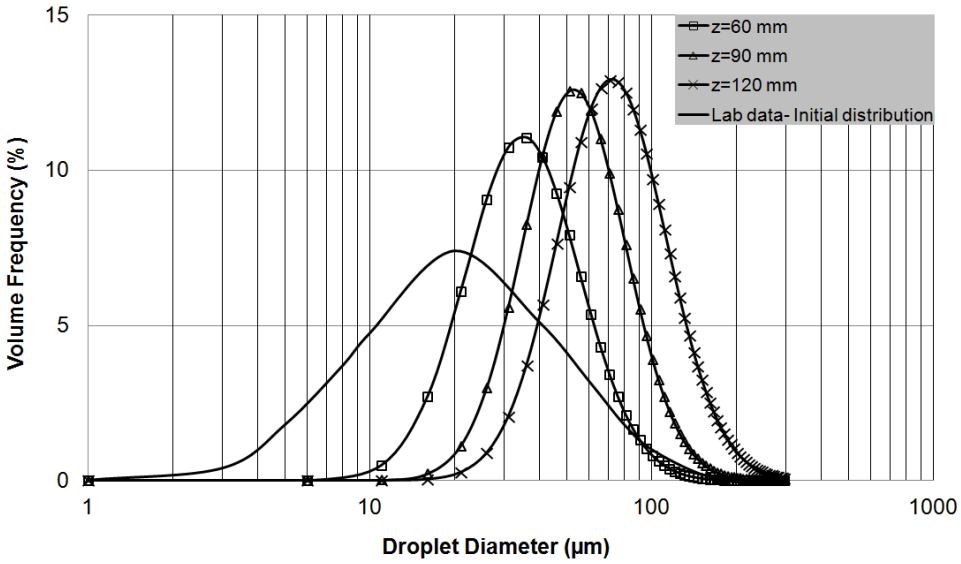

Figure 6.8 Droplet size distribution from simulations at different axial locations using the O'Rourke collision model

6.2.6.2 Simulation Results using the Ko Collision Model

Fig. 6.9 shows the droplet size distribution that resulted from the simulation using the Ko model for describing the collision outcomes [77]. Following the spray development downstream, it is seen that droplets become larger on account of collisions taking place. Since the Ko model has the capability to generate small satellite droplets in certain collisions, the average diameter of droplets is found to be smaller than that calculated by the O'Rourke model. This more realistic description of downstream droplet size distribution implies that some of the collisions within the spray do indeed generate small satellite droplets to offset the effect of other collisions generating larger droplets.

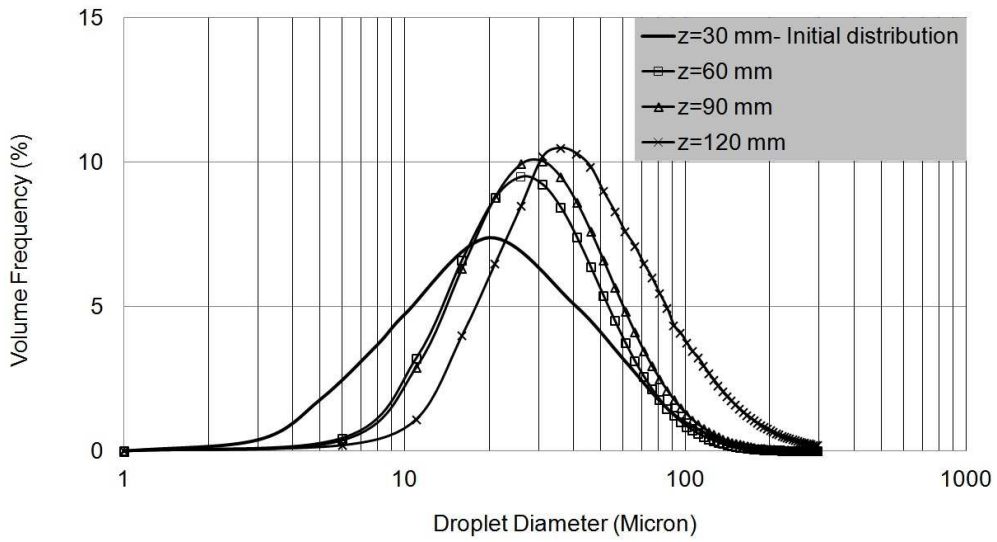

Figure 6.9 Droplet size distribution from simulation at different axial locations using the Ko collision model

6.2.6.3 Simulation Results using the Ko Model with the Taskiran Impact Parameter Model (Extended Ko Model)

Fig. 6.10 shows the droplet size distribution that resulted from the simulation using the Ko model for describing the collision outcomes, but with the analytical model of Taskiran [76] for calculating the binary impact parameter of each collision. This model also predicts that droplets become larger as they move downstream within the spray, but their size increase with distance is much slower and a much closer match to experimental data.

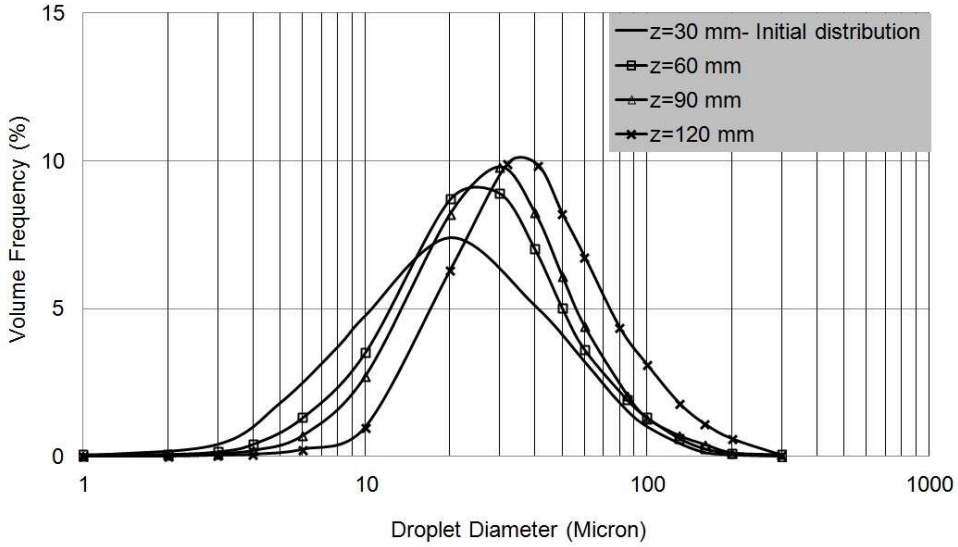

Figure 6.10 Obtained droplet size distribution at different axial location using Ko collision model and analytical impact parameter (extended Ko model)

6.2.6.4 Comparing Collision Models

Fig. 6.12 shows the size distribution of droplets initially measured at 30 mm below the injector tip, at three different downstream locations. As already mentioned, the Weber number range is between 0.5 and 86.7, and the Reynolds number is in the range of 600 and 6,400 based on the following definitions.

$$We = \frac{\rho d_{small} U_{rel}^2}{\sigma}, \tag{6.24}$$

$$Re = \frac{\rho d_{small} U_{rel}}{\mu}, \tag{6.25}$$

where d_{small} is the smaller droplet diameter in a binary collision, U_{rel} is the relative velocity of two droplets, σ is the droplet surface tension and μ is the droplet viscosity. All three models predict the movement of the size distribution toward larger droplets, however there are significant differences in how much larger droplets become during spray development. The O'Rourke model does not take into account the generation of small satellite droplets in certain collisions and it tends to overpredict the size of droplets relative to other models. Because of the predominantly unidirectional flow in this study, there are many almost head-on-collisions taking place, in which case the impact parameter is close to zero. In the Ko collision model the impact parameter is estimated as a random positive number less than 1. Hence according to Fig. 6.11, coalescence can take place randomly in binary collisions without any sensitivity to the collision angle. However in the extended Ko model, since the impact parameter is calculated analytically for each collision, the number of coalescences through head-on-collisions is lower than predicted by the Ko model. It is for this reason that the extended Ko model predicts droplet sizes to be smaller than the Ko model. Table 6.1 shows the number of collisions that take place over a distance of 30 mm for each model.

Table 6.1 Collision models test cases

Collision model	O'Rourke	Ko	Extended-Ko
Total initial droplets	2000	2000	2000
Total collisions	6,157	41,574	38,973
Total coalescences	4,781	5,364	4,056
Total satellite droplets	0	26,154	20,426

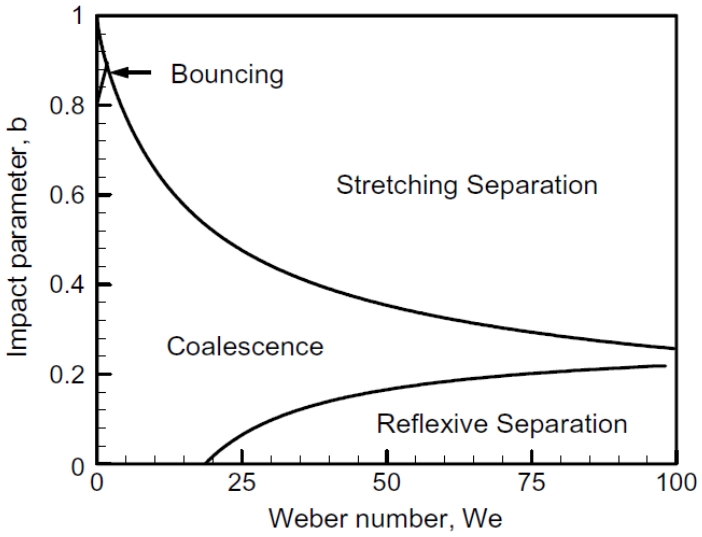

Figure 6.11 Binary collision regimes criteria for the same size droplets

From Fig. 6.12 it seems that considering the formation of stellate droplets along with using the analytical approach to predict the impact parameter makes the predicted size distribution closer to the experimental results. Since in the O'Rourke model satellite droplets do not generate, this model overpredicts the droplet size distribution. In the models that consider formation of satellite droplets, this overprediction is less than what it is seen in the O'Rourke. However since in this study there are lots of heads-on collision and since the Extended Ko modeling uses an analytical calculated based impact parameter in the case of collision, this model gives trustworthy results, however there is still discrepancies between model and lab data which might be either come from the fact that the real droplets are not completely spherical or the experimental errors.

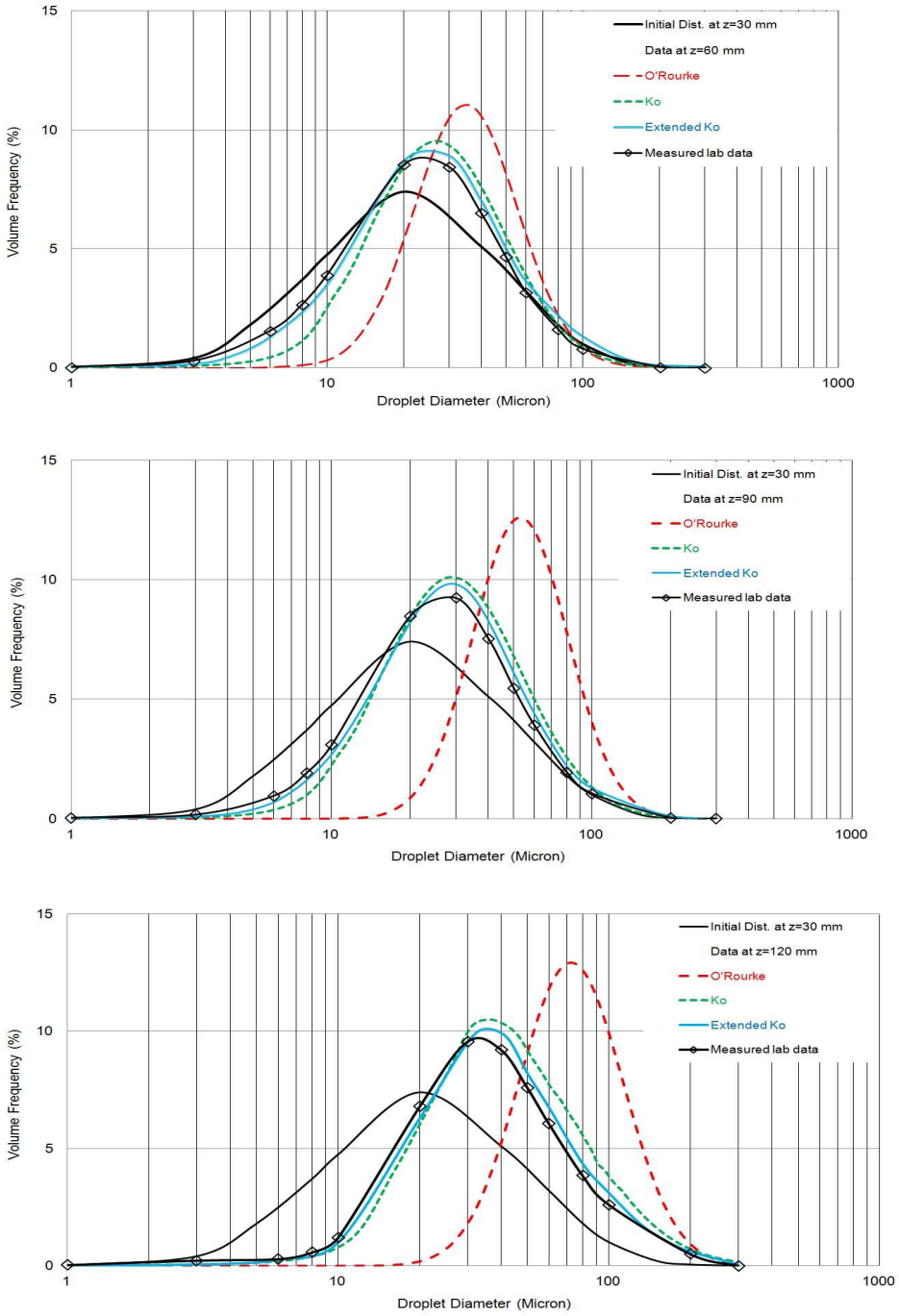

Figure 6.12 Comparison of different collision models results

6.2.7 Effects of Instrumentation Uncertainty

Fig. 6.13 shows the droplet size distribution for an n-heptane spray at $10\ MPa$ injection pressure measured $30\ mm$ downstream of the injector tip. As discussed in the previous chapter, the effect

of uncertainty in measurements of size distribution with the Malvern Spraytec has no more than 5 percent in droplet size. This effect is represented in Fig. 6.13, by plotting an envelope around the measured size distribution, corresponding to this measurement uncertainty, showing by the blue dashed line. The size distribution results for this envelope of initial conditions, predicted $120\ mm$ downstream of the injector tip using the extended Ko model are shown. The envelope of predictions of the extended Ko model at this level of uncertainty are compared with the measured data at $z = 120\ mm$ in Fig. 6.13. The envelope clearly bounds the experimental data, indicating that the prediction accuracy is comparable to that of the experimental uncertainty.

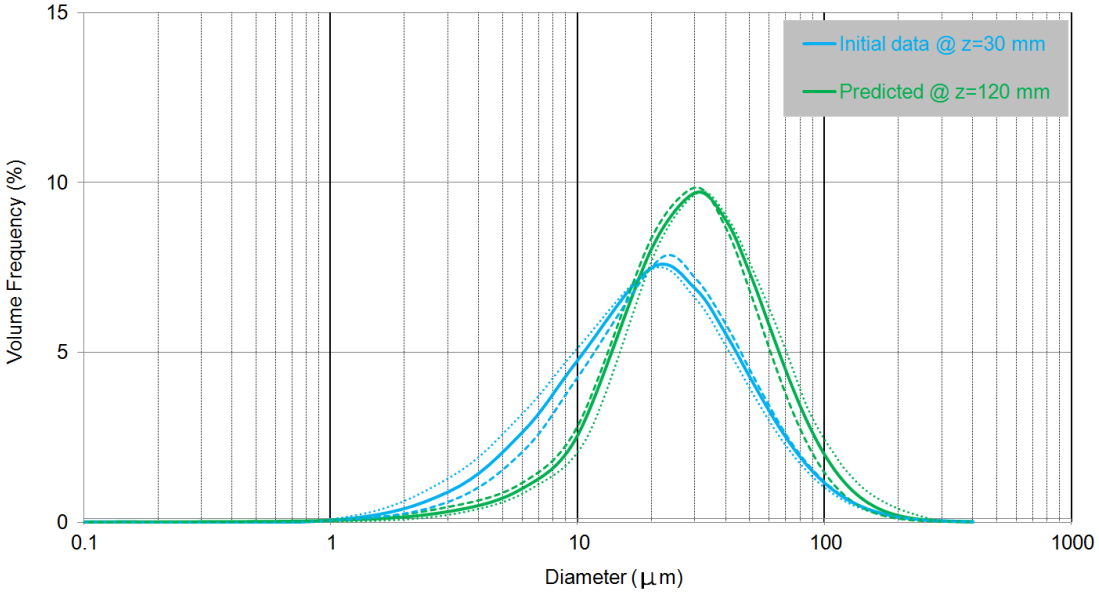

Figure 6.13 Effects of instrumentation uncertainty on predicted droplet size distribution using extended Ko collision model

6.2.8 Simulation Results At Elevated Temperature

In order to examine the accuracy of the extended Ko collision model at temperatures higher than ambient, a simulation was performed to study the simultaneous effects of evaporation and collision on size distribution in the spray. In this simulation, droplet temperatures were assumed to be at

initially $70^{\circ}C$ to experimental measurements of droplet size distribution at this fuel temperature. The d^2 evaporation model was implemented with the extended Ko collision model, so that droplet sizes decreased on account of evaporation between collisions. For the purposes of this study, the complexity of droplet evaporation can be simplified significantly by making the following assumptions:

i) The evaporation process is quasi steady. This means that at any instant in time the process of evaporation can be described as if it were in steady state. This assumption eliminates the need to solve partial differential equations.

ii) The droplet temperature is uniform and assumed to be a fixed value below the boiling point of the liquid. This assumption eliminates the need to apply conservation of energy to the gas phase surrounding the liquid droplet and to the droplet itself.

iii) The mass fraction of vapor at the droplet surface is determined by liquid-vapor equilibrium at the droplet temperature.

iv) Both liquid and gas thermodynamic properties including thermal conductivity, density and heat capacity are constant.

v) The ambient air is assumed to be traveling at the same velocity as the droplet, so the heat transfer problem is assumed to be a stationary rather than convective one.

Fig. 6.14 defines the spherically symmetric coordinate system for an evaporating droplet. Very far from the droplet surface, the mass fraction of droplet vapor is assumed to be zero.

With the above assumptions, the mass evaporation rate, $\dot{m}$, and droplet diameter, $d(t)$, can be related by writing a droplet vapor species conservation equation, and a droplet liquid mass conservation equation. The species originally in the liquid phase is the species transported, and

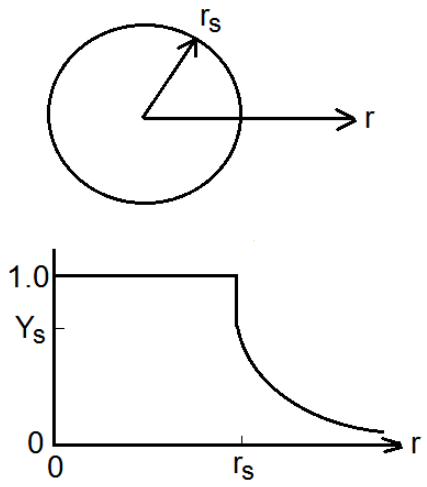

Figure 6.14 Evaporation of a liquid droplet in a quiescent environment

there is no slip velocity between the droplet and the ambient air. So one can say

$$\dot{m}(r) = constant = 4\pi r^2 \dot{m}'' \tag{6.26}$$

Species conservation for droplet vapor becomes

$$\dot{m}'' = Y_S \dot{m}'' - \rho D \frac{dY_S}{dr} \tag{6.27}$$

where Y_S is the vapor mass fraction at the interface, ρ is the mixture density at the interface, and D is the diffusivity coefficient. Substituting Eq. 6.27 into 6.26 and rearranging to solve for the evaporation rate, yields

$$\dot{m} = 4\pi r_S \rho D \; Ln\left[\frac{1 - Y_\infty}{1 - Y_S}\right] \tag{6.28}$$

where Y_∞ is the vapor mass fraction far from the droplet, which can be set to zero. Since the rate at which the mass of the droplet decreases is equal to the rate at which the liquid is vaporized, it

follows that

$$\frac{dm}{dt} = \frac{d(\rho_l \pi \frac{d^3}{6})}{dt} = -\dot{m} \tag{6.29}$$

Substituting Eq. 6.29 into 6.28 and differentiating yields:

$$\frac{d(d^2)}{dt} = -\frac{8\rho D}{\rho_l} Ln\left[\frac{1-Y_\infty}{1-Y_s}\right] = -K \tag{6.30}$$

The slope is defined as the evaporation constant K [78]:

$$K = \frac{8\rho D}{\rho_l} Ln\left[\frac{1-Y_\infty}{1-Y_s}\right] \tag{6.31}$$

Table 6.2 n-heptane thermodynamics properties

**********	Value	Unit
Fluid type	n-heptane	C_7H_{16}
Boiling temperature (at $1atm$)	371.4	K
Molecular weight	100.2	$\frac{gr}{mole}$
Liquid density (at $70^\circ C$)	640	$\frac{kg}{m^3}$
Diffusivity (at air)	0.065	$\frac{cm^2}{m}$
Gas constant	0.083	$\frac{kJ}{kgK}$
Heat of evaporation	336.5	$\frac{kJ}{kg}$

To calculate the evaporation constant for n-heptane, from its thermodynamic properties (Table 6.2), the Clausius-Clapeyron equation to estimate saturation pressure variation with temperature can be written as:

$$\frac{dP_{sat}}{P_{sat}} = \frac{h_{fg}}{R} \frac{dT_{sat}}{T_{sat}^2} \tag{6.32}$$

where sat denotes the saturation condition, h_{fg} is the heat of evaporation, and R is the gas constant.

$$[ln\ P]_{1atm}^{P_{sat}} = \frac{-336.5\left(\frac{kJ}{kg}\right)}{0.083\left(\frac{kJ}{kgK}\right)}\left[\frac{1}{T}\right]_{371\ K}^{368\ K} \rightarrow P_{sat} = 0.9\ atm \tag{6.33}$$

The interface mole fraction (X) and mixture molecular weight (M_{mix}) then can be calculated as

$$X = \frac{P_{sat}}{P_{atm}} = 0.9 \tag{6.34}$$

$$M_{mix} = X \times 100.2 + (1 - X)\,29 = 93.08\ \frac{mole}{gr} \tag{6.35}$$

The interface mass fraction (Y_s) then can be calculated from

$$Y_s = X\frac{100.2}{M_{mix}} = 0.968 \tag{6.36}$$

Substituting these quantities into Eq. 6.31 completes the d^2 model for n-heptane as:

$$d^2\,(t) = d_0^2\,(t) - Kt = d_0^2\,(t) - 34 \times 10^{-8}\ t \tag{6.37}$$

The droplet size distributions at two different locations were then compared with simulations of a heptane spray at $70^{\circ}C$, using the simulation approach described earlier. Fig. 6.15 shows the droplet size distribution of the extended Ko collision model,together with the d^2 evaporation model at 60 and $120\ mm$ downstream of the injector tip. It seems that even at elevated temperatures around $70^{\circ}C$, the collision model can play the dominant part of the simulation. Experimental lab data shows that even though droplets evaporate at higher temperatures more rapidly, many collisions take place during the spray development which make the droplets become larger. There are some discrepancies between the simulation and lab results which can be due to the accuracy of

the droplet evaporation model and the fact that in reality droplets are not completely spherical.

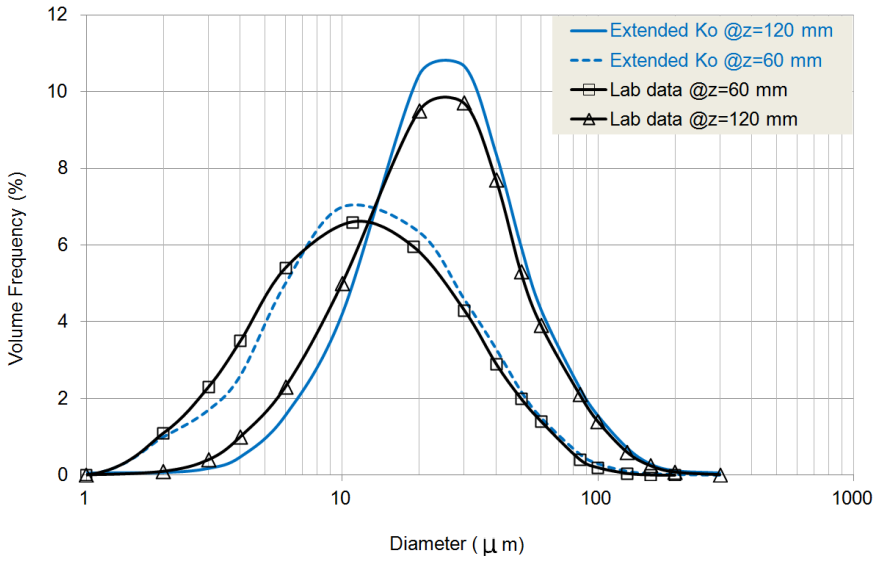

Figure 6.15 Simulation and lab data comparison at n-heptane temperature of $70^{\circ}C$

Fig. 6.16 shows the effect of using the d^2 evaporation model in the extended Ko collision model. Without using the evaporation model, the extended Ko collision model overpredicts the average droplet size by almost $10\ \mu\ m$.

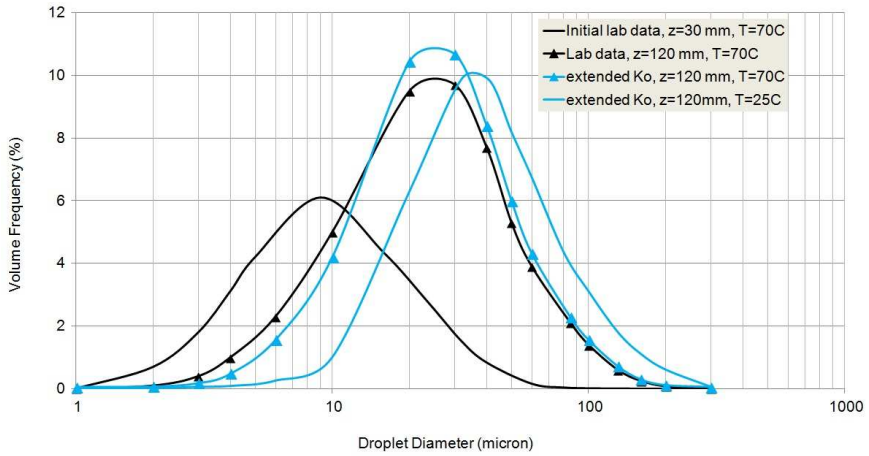

Figure 6.16 Lab data and simulation for extended Ko collision model at an elevated temperature

Chapter 7

Summary, Conclusions and Recommendations for Future Work

7.1 Summary and Conclusions

In this dissertation the character of n-heptane pulsed sprays has been investigated for downstream of the injector. Specifically, macroscopic and microscopic characteristics of fuel sprays are measured experimentally over a range of different injection parameters. These characteristics included spray tip penetration, spreading angle, and droplet size distribution. Interpretations of the behavior of the spray development based on droplet evaporation and collision models are also presented. For liquid sprays, the two parameters of spray tip penetration and spray angle describe the overall shape of the fuel spray, and can be modeled by empirical equations. The droplet size distribution in pulsed fuel sprays is log-normal just as in steady continuous sprays.

In consideration of droplet evaporation within sprays, mass transfer analysis are carried out using empirical equations for Sherwood number. Collision models for two impinging droplets are introduced and the possible outcomes of their collision are explained. It is shown that for two individual droplets the outcome of each collision is based predominantly on the Weber number, surface tension, and geometric parameters. It was proposed that liquid spray development could be modeled as a stochastic in process and this behavior was consistent with experimental measurements.

This stochastic nature is also explored through collision models.

Another part of this study describes appropriate ways of visualizing liquid sprays and calculating geometrical parameters. In this study, a high speed camera is used to record the development of n-heptane sprays illuminated by a diffused white background light source. The raw images are processed by subtracting the background and filtering the noise, after which Edge detection techniques are carried out to locate the borders of the spray in order to find the spray geometrical parameters. The effects of fuel injection pressure and temperature on the spray penetration length and spreading angle were then measured experimentally.

A Spraytec laser diffraction system is used to determine the size distribution of droplets at different axial locations. This system is able to calculate the size distribution based on the light scattering intensity which is detected by an angular array of detectors.

It was also determined experimentally how the variation of injection pressure and temperature influences the droplet size distribution. In the present fuel spray study, it was found that droplet size changes primarily through collision and that effects of evaporation are negligible at temperatures close to ambient for n-heptane.

Since trustworthy measurements of droplet size distribution at different downstream locations in the fuel spray were made, the adequacy of simplified modeling approaches for the far field of a fuel spray could be explored. By using measured droplet size distributions near the injector nozzle as the initial condition and the measured far field size distribution as the target data different spray models performance are compared. In this study, the simplified model approach is the one in which a large number of spherical droplets, of a chosen size distribution and initial velocity field, move in a Lagrangian frame, governed by Newton's second law of motion. Several well-known binary droplet collision models are implemented during spray development. One of these models is the O'Rourke model [67] which takes into account bouncing, coalescence and separation as

three possible outcomes of binary collisions.

The other model explored is the Ko model [77] in which generation of satellite droplets is included. Another collision model is developed in this study based on an extension of Ko model using analytically calculated impact parameter proposed by Taskiran [76]. Comparison of the above models shows that the O'Rourke model overpredicts the droplet size distribution because of its neglect of satellite droplets. Because of the unidirectional spray development in this study, there are many of close-to-head-on-collisions taking place, so that impact parameters are often close to zero. In the Ko collision modeling, the impact parameter is estimated as a random positive number less than 1. This is why coalescence can still be taken place in binary collisions. However in the Taskiran-extended Ko modeling, since the impact parameter is calculated analytically, the number of coalescence in close-to-heads-on-collisions is considered less than that of the Ko model. This is the reason that the extended Ko model predicts droplet sizes smaller than the Ko model. Of the three collision models considered in this study, the extended Ko model predicts results in a best agreement with lab data. It is concluded that this approach of Lagrangian modeling is very effective for simulating the behavior of single jet sprays with Weber numbers of around $100,000$. In this study droplets were considered to be spherical, and it is not safe to assume that this model applies for non-spherical droplets.

There are limitations applied in using the extended Ko collision model. Boundaries for coalescence and separation outcomes are valid for droplets with dynamic viscosity to surface tension ratio ($\frac{\mu}{\sigma}$) of greater than 0.02 s/m [79]. Since in this study droplet binary collision Weber number ($\frac{\rho U^2 d}{\sigma}$) is less than 100, more cautious should be used for using the extended Ko collision model in sprays which their Weber number exceeds 100. It was also concluded that for sprays similar to those of this study, if the droplet size distribution is known at some plane downstream of the break-ups region, the development of spray can be simulated by using a simple Lagrangian model.

Therefore, collision impact parameter can be calculated analytically.

7.2 Recommendations for Future Work

In future research into this topic, it is recommended that the following be examined:

i) Non-sphericity of droplets: In this study the range of non-dimensional Weber and Reynolds numbers of spray droplets are in the range that they can be assumed spherical. For cases in which fuel spray droplets have non-spherical shapes, the extended Ko collision model could be assessed for non-spherical droplets in the fuel spray development modeling by comparison with experiments;

ii) Implementing the extended Ko model in multi-hole sprays: More investigation is needed to examining the suitability of collision models in situations in which there are significant velocity shear forces so droplets can not be assumed spherical, or more than one spray is developing;

iii) Implementing a more comprehensive evaporation model for high environment temperature: The proposed model might not work well in cases where there are large temperature differences between the spray jet and ambient, so d^2 model might not describe evaporation accurately. This could be explored by using the proposed collision model along with more sophisticated evaporation models;

iiii) Break-up models: Examining more sophisticated approaches to predicting the fuel spray break-up from upstream initial conditions, provided by downstream experimentally measured droplet size distributions.

BIBLIOGRAPHY

BIBLIOGRAPHY

[1] S. Martínez-Martínez, F. A. Sánchez-Cruz, V. R. Bermúdez, and J. M. Riesco-Ávila, "Liquid sprays characteristics in diesel engines," *SAE Technical Paper*, no. 13056, 2002.

[2] A. K. Sumer Dirbude, Vinayak Eswaran, "Droplet evaporation modeling of some conventional and alternative fuels at low pressure," *38th international and 4thnational conference on Fluid Mechanics and Fluid Power*, 2010.

[3] S. Morsi and A. Alexander, "An investigation of particle trajectories in two-phase flow systems," *J. Fluid Mech*, vol. 55, no. 2, pp. 193–208, 1972.

[4] P. Strakey, "Assessment of multiple scattering errors of laser diffraction instruments," *International Conference on Liquid Atomization and Spray Systems*, 2003.

[5] A. C. F. Savart, "Brief history of droplet formation," *Phys.*, vol. 53, p. 337, 1833.

[6] L. Rayleigh, "Falling jet instability," *Proc. R. Soc.*, vol. 29, p. 71, 1879.

[7] W. G. R. J. Donnelly, "Experiments on the capillary instability of a liquid jet," *Proc. R. Soc.*, vol. 33, p. 547, 1966.

[8] P. Lafrance, "Nonlinear breakup of a laminar liquid jet," *AIP*, vol. 25, no. 8, 1974.

[9] R. Reitz and F. Bracco, "Mechanism of atomization of a liquid jet," *Physics of Fluids*, vol. 25, p. 1730, 1982.

[10] E. Lubarsky, D. Shcherbik, O. Bibik, Y. Gopala, J. Bennewitz, and B. Zinn, "Fuel jet in cross flow. experimental study of spray characteristics," in *ILASS Americas, 23rd Annual Conference on Liquid Atomization and Spray Systems, Ventura, CA, May 2011*, 2011.

[11] H. E. Miller and E. G. Beardsley, *Spray penetration with a simple fuel injection nozzle*. National Advisory Committee for Aeronautics, 1926.

[12] J. Dent, "A basis for the comparison of various experimental methods for studying spray penetration," *Diesel Engine*, vol. 2012, pp. 12–04, 1971.

[13] C. D., "Estudio teorico experimental del chorro libre diesel isotermo," *Tesis Doctoral, E. T. S. Ingenieros Industriales, Universidad Politecnica de Valencia, Spain*, 1998.

[14] B. Jawad, E. Gulari, and N. Henein, "Characteristics of intermittent fuel sprays," *Combustion and flame*, vol. 88, no. 3, pp. 384–396, 1992.

[15] J. Jimenez, F. Castro, F. Tinaut, and B. Gimenez, "The tip evolution of an evaporative intermittent fuel spray," in *Thermo-and Fluid-dynamic Processes in Diesel Engines: Selected Papers from the THIESEL 2000 Conference Held in Valencia, Spain, September 13-15, 2000*, p. 175, Springer Verlag, 2002.

[16] B. F. Reitz R.D., "On the dependence of spray angle and other spray parameters on nozzle design and operating conditions," *SAE Technical Paper*, no. 79094, 1979.

[17] A. M. Hiroyasu H., Kodata T., "Fuel spray characterization in diesel engines. combustion modeling in reciprocant engines," *Plenum Press*, 1980.

[18] F. Williams, "Spray combustion and atomization," *Physics of fluids*, vol. 1, p. 541, 1958.

[19] W. Ning, *Development of a next-generation spray and atomization model using an Eulerian-Lagrangian methodology*. ProQuest, 2007.

[20] G. Luret, G. Blokkeel, R. Lebas, T. Ménard, A. Berlemont, and F. Demoulin, "Spray interactions: modeling of collision/coalescence phenomena," in *22nd European Conference on Liquid Atomization and Spray Systems. Como Lake, Italy*, 2008.

[21] A. Vallet, A. Burluka, and R. Borghi, "Development of a eulerian model for the ?atomization? of a liquid jet," *Atomization and Sprays*, vol. 11, no. 6, 2001.

[22] C. Arcoumanis, M. Gavaises, and B. French, "Effect of fuel injection processes on the structure of diesel sprays," *SAE transactions*, vol. 106, no. 3, pp. 1025–1064, 1997.

[23] K. Huh and A. Gosman, "A phenomenological model of diesel spray atomization," in *Proceedings of the international conference on multiphase flows*, pp. 24–27, 1991.

[24] C. Baumgarten, J. Stegemann, and G. Merker, "A new model for cavitation induced primary break-up of diesel sprays," *Zaragoza*, vol. 9, p. 11, 2002.

[25] Y. Wan and N. Peters, "Scaling of spray penetration with evaporation," *Atomization and sprays*, vol. 9, no. 2, 1999.

[26] S. Sazhin, G. Feng, and M. Heikal, "A model for fuel spray penetration," *Fuel*, vol. 80, no. 15, pp. 2171–2180, 2001.

[27] J. D. Naber and D. L. Siebers, "Effects of gas density and vaporization on penetration and dispersion of diesel sprays," *SAE transactions*, vol. 105, pp. 82–111, 1996.

[28] I. Roisman, L. Araneo, and C. Tropea, "Effect of ambient pressure on penetration of a diesel spray," *International journal of multiphase flow*, vol. 33, no. 8, pp. 904–920, 2007.

[29] M. V. Panchagnula and P. E. Sojka, "Spatial droplet velocity and size profiles in effervescent atomizer-produced sprays," *Fuel*, vol. 78, no. 6, pp. 729–741, 1999.

[30] S. Ghaemi, D. Nobes, and P. Rahimi, "Investigation of the spatial distribution of droplet smd in the spray field of an effervescent atomizer," in *21st Annual ILASS-Americas Conference, Orlando, FL, USA*, 2008.

[31] A. L. Kastengren, C. F. Powell, Y. Wang, K.-S. Im, and J. Wang, "X-ray radiography measurements of diesel spray structure at engine-like ambient density," *Atomization and Sprays*, vol. 19, no. 11, 2009.

[32] R. Klein-Douwel, P. Frijters, L. Somers, W. De Boer, and R. Baert, "Macroscopic diesel fuel spray shadowgraphy using high speed digital imaging in a high pressure cell," *Fuel*, vol. 86, no. 12, pp. 1994–2007, 2007.

[33] M. E. Ozgur O. Taskiran, "Experimental study on diesel spray characteristics and auto ignition process," *Journal of Combustion*, no. 528126, 2011.

[34] S. S. Sazhin, "Advanced models of fuel droplet heating and evaporation," *Progress in energy and combustion science*, vol. 32, no. 2, pp. 162–214, 2006.

[35] I. Goldfarb, V. Goldshtein, G. Kuzmenko, and J. B. Greenberg, "On thermal explosion of a cool spray in a hot gas," in *Symposium (International) on Combustion*, vol. 27, pp. 2367–2374, Elsevier, 1998.

[36] A. McIntosh, V. Gol'dshtein, I. Goldfarb, and A. Zinoviev, "Thermal explosion in a combustible gas containing fuel droplets," *Combustion Theory and Modelling*, vol. 2, no. 2, pp. 153–165, 1998.

[37] I. Goldfarb, V. Gol'dshtein, G. Kuzmenko, and S. Sazhin, "Thermal radiation effect on thermal explosion in gas containing fuel droplets," *Combustion Theory and Modelling*, vol. 3, no. 4, pp. 769–787, 1999.

[38] S. Sazhin, G. Feng, M. Heikal, I. Goldfarb, V. Gol?dshtein, and G. Kuzmenko, "Thermal ignition analysis of a monodisperse spray with radiation," *Combustion and Flame*, vol. 124, no. 4, pp. 684–701, 2001.

[39] V. Bykov, I. Goldfarb, V. Gol'dshtein, and J. B. Greenberg, "Thermal explosion in a hot gas mixture with fuel droplets: a two reactant model," *Combustion Theory and Modelling*, vol. 6, no. 2, pp. 339–359, 2002.

[40] N. A. Fuchs *et al.*, "Evaporation and droplet growth in gaseous media.," *The Pergamon Press, Oxford.*, vol. 2, no. 2, 1959.

[41] A. Polyanin, A. Kutepov, A. Vyazmin, and D. Kazenin, *Hydrodynamics, mass and heat transfer in chemical engineering, Topics in Chemical Engineering, vol. 14*. Taylor & Francis, London, 2002.

[42] C. Chiang, M. Raju, and W. Sirignano, "Numerical analysis of convecting, vaporizing fuel droplet with variable properties," *International journal of heat and mass transfer*, vol. 35, no. 5, pp. 1307–1324, 1992.

[43] R. Haywood, R. Nafziger, and M. Renksizbulut, "A detailed examination of gas and liquid phase transient processes in convective droplet evaporation," *Journal of Heat Transfer (Transactions of the ASME (American Society of Mechanical Engineers), Series C);(United States)*, vol. 111, no. 2, 1989.

[44] M. Renksizbulut and M. Yuen, "Experimental study of droplet evaporation in a high-temperature air stream," *Journal of Heat Transfer*, vol. 105, p. 384, 1983.

[45] S. Sazhin, W. Abdelghaffar, P. Krutitskii, E. Sazhina, and M. Heikal, "New approaches to numerical modelling of droplet transient heating and evaporation," *International journal of heat and mass transfer*, vol. 48, no. 19, pp. 4215–4228, 2005.

[46] L. C. X. D. C. Mang Wai Woo, Nan Fu, "Evaporation of pure droplets in the convective regime under high mass flux," *Drying Technology*, vol. 48, no. 19, 2011.

[47] G. J. Brereton, "A discrete multicomponenet temperature-dependent model for the evaporation of spherical droplets," *HEat and Mass Trnasfer*, Submitted 2012.

[48] D. Torres and P. O'Rourke, "Multicomponent fuel vaporization at high pressures.," tech. rep., Los Alamos National Laboratory, 2002.

[49] P. O?Rourke and F. Bracco, "Modelling of drop interactions in thick sprays and a comparison with experiments," *Proc. Inst. Mech. Eng*, vol. 9, pp. 101–116, 1980.

[50] N. Ashgriz and J. Poo, "Coalescence and separation in binary collisions of liquid drops," *Journal of Fluid Mechanics*, vol. 221, no. 1, pp. 183–204, 1990.

[51] J. Qian and C. Law, "Regimes of coalescence and separation in droplet collision," *Journal of Fluid Mechanics*, vol. 331, no. 1, pp. 59–80, 1997.

[52] G. Brenn, D. Valkovska, and K. Danov, "The formation of satellite droplets by unstable binary drop collisions," *Physics of Fluids*, vol. 13, p. 2463, 2001.

[53] J.-P. Estrade, H. Carentz, G. Lavergne, and Y. Biscos, "Experimental investigation of dynamic binary collision of ethanol droplets–a model for droplet coalescence and bouncing," *International journal of heat and fluid flow*, vol. 20, no. 5, pp. 486–491, 1999.

[54] A. Wadewitz and E. Specht, "Limit value of the nusselt number for particles of different shape," *International journal of heat and mass transfer*, vol. 44, no. 5, pp. 967–975, 2001.

[55] B. Abramzon and W. Sirignano, "Droplet vaporization model for spray combustion calculations," *International journal of heat and mass transfer*, vol. 32, no. 9, pp. 1605–1618, 1989.

[56] G. A. E. Godsave, "studies of the combustion of drops in fuel spray the burning of single drops of fuel," *Fourth Symposium of Combustion*, pp. 818–830, 1953.

[57] F. P. Incropera, A. S. Lavine, and D. P. DeWitt, *Fundamentals of heat and mass transfer*. John Wiley & Sons Incorporated, 2011.

[58] M. Renksizbulut, R. Nafziger, and X. Li, "A mass transfer correlation for droplet evaporation in high-temperature flows," *Chemical engineering science*, vol. 46, no. 9, pp. 2351–2358, 1991.

[59] G. Aguilar, B. Majaron, W. Verkruysse, Y. Zhou, J. S. Nelson, and E. Lavernia, "Theoretical and experimental analysis of droplet diameter, temperature, and evaporation rate evolution in cryogenic sprays," *International Journal of Heat and Mass Transfer*, vol. 44, no. 17, pp. 3201–3211, 2001.

[60] L. Dombrovsky and S. Sazhin, "A simplified non-isothermal model for droplet heating and evaporation," *International communications in heat and mass transfer*, vol. 30, no. 6, pp. 787–796, 2003.

[61] S. Lin and R. Reitz, "Drop and spray formation from a liquid jet," *Annual Review of Fluid Mechanics*, vol. 30, no. 1, pp. 85–105, 1998.

[62] A. Kolmogorov, "On the log-normal distribution of particles sizes during break-up process," in *Dokl. Akad. Nauk SSSR*, vol. 31, p. 99, Elsevier, 1941.

[63] M. Gorokhovski and V. Saveliev, "Analyses of kolmogorov?s model of breakup and its application into lagrangian computation of liquid sprays under air-blast atomization," *Physics of Fluids*, vol. 15, p. 184, 2003.

[64] L. Rayleigh, "The theory of sound, 1894," *Republished by Dover Publications, New York*, vol. 326, no. 1566, pp. 393–408.

[65] G. H. Ko and H. S. Ryou, "Modeling of droplet collision-induced breakup process," *International journal of multiphase flow*, vol. 31, no. 6, pp. 723–738, 2005.

[66] P. Brazier-Smith, S. Jennings, and J. Latham, "The interaction of falling water drops: coalescence," *Proceedings of the Royal Society of London. A. Mathematical and Physical Sciences*, vol. 326, no. 1566, pp. 393–408, 1972.

[67] S. Kim, D. J. Lee, and C. S. Lee, "Modeling of binary droplet collisions for application to inter-impingement sprays," *International Journal of Multiphase Flow*, vol. 35, no. 6, pp. 533–549, 2009.

[68] P. Brazier-Smith, S. Jennings, and J. Latham, "The interaction of falling water drops: coalescence," *Proceedings of the Royal Society of London. A. Mathematical and Physical Sciences*, vol. 326, no. 1566, pp. 393–408, 1972.

[69] A. Munnannur and R. D. Reitz, "A new predictive model for fragmenting and non-fragmenting binary droplet collisions," *International journal of multiphase flow*, vol. 33, no. 8, pp. 873–896, 2007.

[70] T. L. Georjon and R. D. Reitz, "A drop-shattering collision model for multidimensional spray computations," *Atomization and Sprays*, vol. 9, no. 3, 1999.

[71] S. BEGG, "In-cylinder airflow and fuel spray characterisation for a top entry direct injection gasoline engines," *Thesis (PhD), University of Brighton, United Kingdom*, 2003.

[72] J. Liu, H. Vu, S. S. Yoon, R. A. Jepsen, and G. Aguilar, "Splashing phenomena during liquid droplet impact," *Atomization and Sprays*, vol. 20, no. 4, 2010.

[73] S. Sazhin, S. Martynov, T. Kristyadi, and C. Crua, "Diesel fuel spray penetration, heating, evaporation and ignition: modelling vs. experimentation," *International Journal of Engineering Systems Modelling and Simulation*, vol. 1, no. 1, pp. 1–19, 2008.

[74] S. S. Sazhin, "Advanced models of fuel droplet heating and evaporation," *Progress in energy and combustion science*, vol. 32, no. 2, pp. 162–214, 2006.

[75] E. K. Shashank and H. Pitsch, “Spray evaporation model sensitivities,”

[76] O. O. Taskiran and M. Ergeneman, “Trajectory based droplet collision model for spray modeling,” *Fuel*, vol. 115, pp. 896–900, 2014.

[77] G. H. Ko and H. S. Ryou, “Modeling of droplet collision-induced breakup process,” *International journal of multiphase flow*, vol. 31, no. 6, pp. 723–738, 2005.

[78] S. R. Turns *et al.*, *An introduction to combustion*, vol. 287. McGraw-hill New York, 1996.

[79] Y. Jiang, A. Umemura, and C. Law, “An experimental investigation on the collision behaviour of hydrocarbon droplets,” *Journal of Fluid Mechanics*, vol. 234, pp. 171–190, 1992.